FABRICATION OF COLLAGEN SCAFFOLDS WITH COMPUTER-DESIGNED INTERNAL MICROARCHITECTURE FOR BLOOD VESSEL ENGINEERING USING INVERSE 3D PRINTING

By

Joab Ogato

A THESIS SUBMITTED TO THE FACULTY OF GRADUATE STUDIES

IN PARTIAL FULFILLMENT OF THE REQUIREMENTS FOR THE DEGREE OF

MASTER OF APPLIED SCIENCE

GRADUATE PROGRAM IN MECHANICAL ENGINEERING

YORK UNIVERSITY, TORONTO, ONTARIO

AUGUST 2022

Abstract

In the field of tissue engineering, three-dimensional printing has been employed in the production of functional tissues with biomimetic structures and required mechanical properties. These engineered tissues can be used as transplant alternatives or disease models for further biomedical research. While there have been successful observations in thin (< 1mm) tissues, viable thick tissues are still challenging to engineer. To obtain viable thick engineered tissue, vasculature is needed to provide nutrients and oxygen and remove waste products from the tissue. Unfortunately, including functional vasculature in engineered constructs has been a technical challenge preventing the fabrication of thick (>1mm) viable tissue.

A method using a commercial three-dimensional printer to produce perfusable vasculature in 3D collagen scaffolds using biocompatible sacrificial moulds is developed in this thesis, with further study in observing the biocompatibility of the obtained scaffolds. The first objective of this thesis was to select and characterize biocompatible wax materials that could be used as printing materials for our selected wax-based 3D printer. This was done by eliminating different biocompatible wax materials from a prescribed list using their manufacturers' literature and performing rheological tests on the selected materials, stearic acid, and polyethylene glycol, to ensure that they could be used as substitute materials in the commercial 3D printer. The result was a commercial 3D printer repurposed for bioprinting.

The second objective of the thesis was to cast and characterize collagen scaffolds for tissue engineering. To achieve the second objective, scaffolds with internal microchannels were produced by inverse 3D printing. Non-destructive observation of the microchannels was done using optical coherence tomography. The scaffold collagen material's chemical and mechanical properties were characterized using scanning electron micrography, Fourier-transform infrared analysis, and a dynamic mechanical analyzer.

After seeding human umbilical vascular endothelial cells into the branched microchannels, scanning electron micrography was used to show the attachment of the cells to the lining of the microchannels, and metabolic activity was observed using Alamar Blue dye after 72 hrs of incubation. This thesis's third objective was to probe the biocompatibility of the produced scaffolds. The obtained results demonstrate the ability to use the inverse 3D printing method to produce microchannel-containing scaffolds for thick tissue engineering using a commercially avaliable 3D printer.

Graphical Abstract

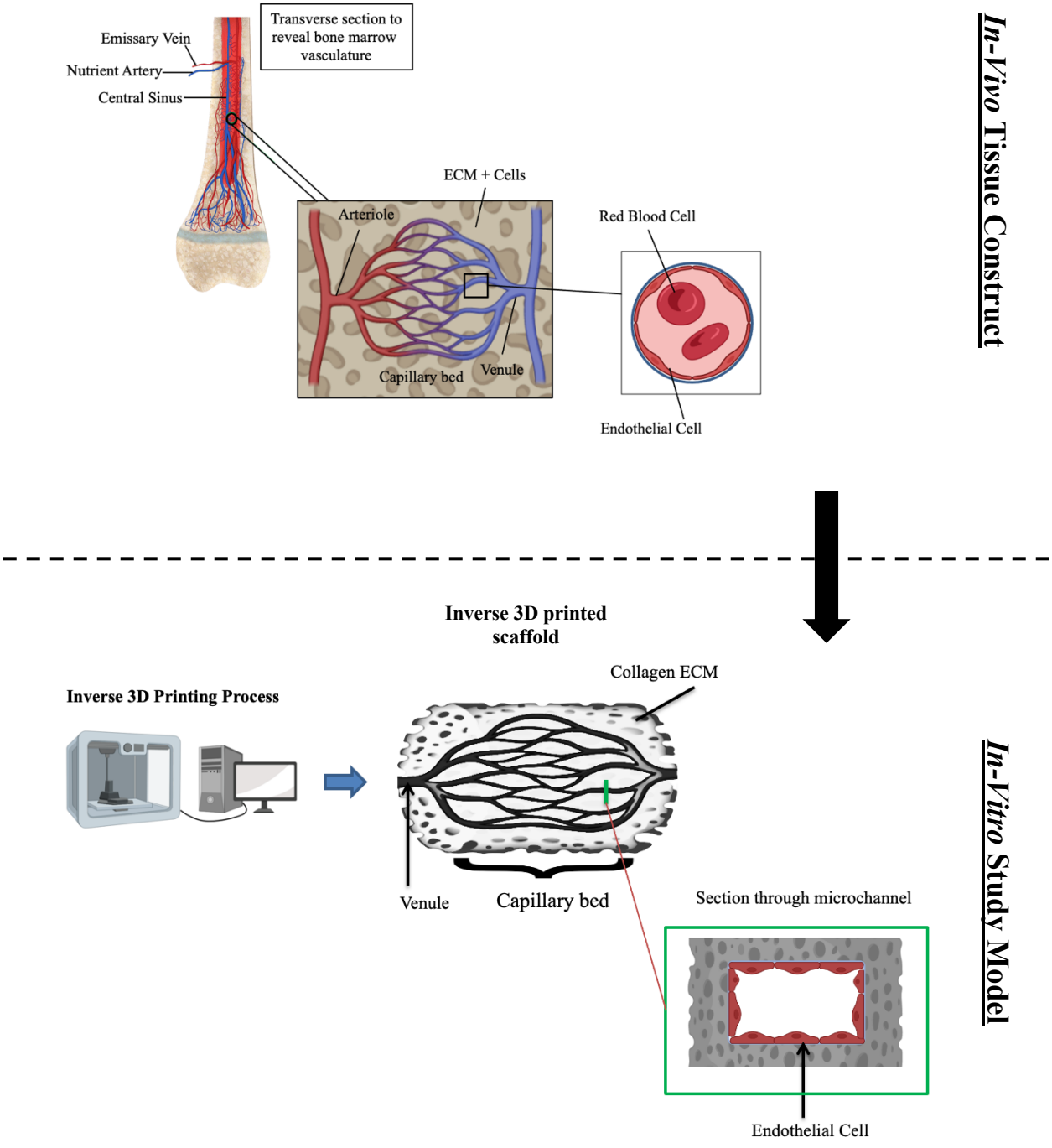

Acknowledgements

Great thanks to the creator, for the gift of science, and to those who preceded me in in the quest for scientific breakthroughs, on whose findings I piggyback my thirst for knowledge and discovery.

My appreciation goes to Prof. Terry Sachlos for his support and guidance during my research as well as Naomi Ogato, my mother, Johnson Ogato, my grandfather and Zillah Ontiriah, my partner who have provided emotional support to me in this quest.

Table of Contents

List Of Figures

List of Tables

Chapter 1: Introduction

1.1 Introduction and Research Motivation

Yearly, the aging population has increased the number of people suffering from organ dysfunction or organ failure due to damaged or diseased tissue. As these traumas, diseases, and injuries cause tissue damage and organ degeneration in the human body, treatment is required, to aid in the tissues' replacement, repair, or regeneration[1-2].

Organ transplants: autografts and allografts have been the conventional clinical therapy used to restore function due to failed tissues or organs[3]. Two challenges have necessitated finding alternative sources of organ transplants: rejection, as a result of the recipients' immune response to the donor tissue[4], and organ shortages[5], due to a lack of donors to cater to the increased demand as seen by the long organ recipient waitlists[4]. Tissue engineering, also known as regenerative medicine, focuses on producing tissue constructs with biomimetic characteristics that can be used to treat damaged tissues or organs[6]. These tissue engineering constructs have also been recently expanded to produce models for use in drug discovery[7] as well as understanding modes of disease progression[8].

In their native state within tissues, cells are normally embedded in an extra-cellular matrix (ECM)[3]. Apart from containing the necessary materials that keep cells alive, the ECM gives the tissue its shape[9] and mechanical properties[10]. The ECM also provides the cells with environmental cues and signals which regulate cellular behaviour[11].

One goal of tissue engineering is to produce substitutes that function like the natural ECM (Fig 1.1) to help guide the growth of functional tissue *in vivo* or *in vitro*. Tissue engineering relies on the use of porous three-dimensional (3D) scaffolds[12]. Tissue engineers have used several methods to fabricate scaffolds that are meant to mimic the natural ECM. The scaffolds, onto which cells are seeded, present an environment favourable for the regeneration of tissues and organs[13] by providing a temporary template for the formation of new tissue.

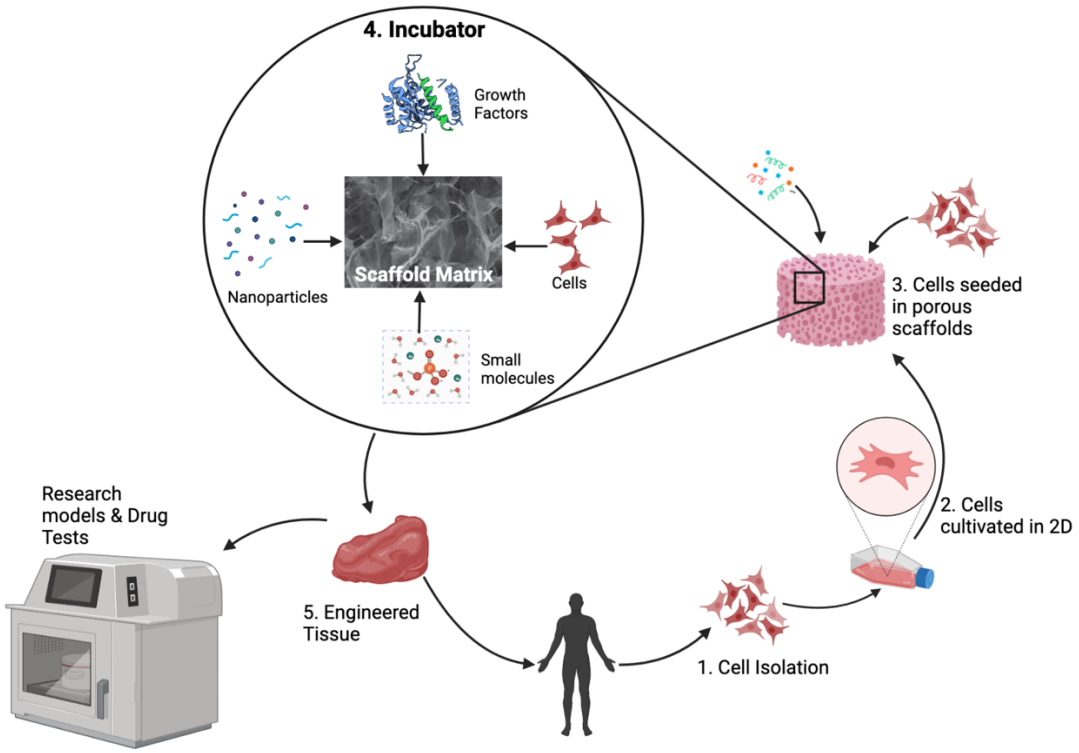

Figure 1.1: A Schematic showing the traditional method of tissue engineering. Cells are isolated from an individual and expanded in tissue culture media before they are seeded on a porous scaffold with the necessary bioactive signalling molecules. This scaffold is then incubated where the tissue reorganizes itself before the tissue is implanted back into the patient. The tissue can also be used as a research model for other conditions or a disease model for drug tests.

Scaffolds with seeded cells can then be implanted in a patient. They will end up ultimately biodegrading and being replaced with new tissue[14]. Acellular scaffolds can also be implanted into a site with an injury and, the injured body can populate the scaffold with its own cells[15].

This process facilitates healing but is dependent on host blood vessel ingrowth to support cell penetration into the scaffold[16-17]. Scaffolds can be loaded with growth factors, which provide signals that can facilitate repair[18].

Previously, scaffolds have also been exposed to a bioreactor that mimicked biophysical stimuli to promote the deposition of ECM before implantation[19]. Once sufficient cell integration has occurred; the cells should produce their own ECM which will replace the scaffold. To improve its qualities for tissue engineering, a scaffold should contain an adequately interconnected pore structure with a pore size distribution that will aid in regenerating tissue by supporting cell growth and differentiation. It should also provide the necessary mechanical strength to achieve the required function for the tissue. Finally, the scaffold should break down into biocompatible by-products and be replaced by the cells' native ECM[20] .

In mammals, collagen is the most abundant ECM molecule. It has been found in both soft and hard connective tissue, blood vessels and organs including the lung and liver[21]. This fact has made collagen a likely candidate in many tissue engineering studies[22-23]. Collagen scaffolds have found in particular clinical success, especially in cartilage[19,24], skin[25], cornea[26], heart tissue[27-28] and bone[29], and tissue engineering, with particular success in dermal regeneration of severe wounds from trauma and burns[21].

Due to its robust nature, a variety of ways can be used to fabricate collagen scaffolds without harming its basic structure. Fabrication techniques that have been used include additive manufacturing, critical point drying[30], electrospinning[31] and the most common, freeze-drying[12].

Additive manufacturing, also called 3D printing, is a layered manufacturing technology that can fabricate tissue engineering scaffolds, build custom-shaped implants and create models of hard tissues. The technology proceeds by creating a 3D model in computer software. Then a printer lays down printing material or binding agent layer-by-layer, to make the designed 3D structure. Currently several 3D printing techniques are used in tissue engineering, including fused deposition modeling[32], stereolithography[33], selective laser sintering[34] and phase-change jet printing[35]. These methods can be used to print scaffolds onto which cells can be seeded and grown in a bioreactor. Most 3D printing techniques use biodegradable synthetic polymers as raw materials[14]. However, these biodegradable synthetic polymers lack the surface chemistry to promote cell adhesion[36] and break down into acidic by-products that create acidic microenvironments[37] making the scaffold unhospitable to resident cells. Due to these limitations, natural polymer scaffolds are preferred for tissue engineering applications but, are subject to thermal and chemical constraints which limit their application in 3D printing techniques.

Consequently, cell and protein-friendly printing techniques have been adapted for tissue engineering and can be further classified into direct bioprinting and indirect printing.

Direct bioprinting involves printing tissues with cells suspended in a hydrogel and using an extrusion-based printer to lay the cell-laden hydrogel on a print bed layer-by-layer to form a 3D tissue without necessarily involving a scaffold[38]. Due to the high shear stresses that can be met during extrusion, some cells die during the printing process[39].

Indirect 3D printing on the other hand involves printing a sacrificial mould into which a high protein concentration material is cast to produce a biocompatible scaffold for tissue engineering purposes[30]. Cells can then be seeded onto the indirectly printed scaffold.

1.2 Research Opportunity and Thesis Objectives

For the cells in a tissue to meet their metabolic demands and remain viable, a perfusable vascular network is necessary to provide the requisite nutrients. The lack of 3D perfusable networks has slowed down industry progress in the development of complex tissues and organs[40]. To prevent development of necrotic tissue within engineered tissue constructs, cells must be close enough at 100 – 200 μm of vessels that can provide oxygen and nutrients[41].

Fabrication of thick scaffolds, as shown in **Figure 2.1**[42] which contain no internal microvasculature, will most likely lead to a necrotic core. Currently, most tissue fabrication methods have not allowed scaffolds to have a total three-dimensional capacity to support large volumes of engineered tissue constructs. Most of the suggested methods to create vascularized constructs have varied limitations.

Creating a layer containing a vascular channel and adding another layer on top of it by the method of lithography has been reported. These systems, however, lack the 3D structure needed to achieve a fully functional tissue in 3D[17]. However, the success of these methods has shown that a network of vessels improves the viability of engineered tissue. Furthermore, these methods have further reported actual behaviour experienced by native vascular systems, such as the sprouting of angiogenic vessels into the engineered construct[16].

This research puts forth a method that uses a phase-change jet printing system to print sacrificial moulds used to cast collagen scaffolds with internal microchannels made in a method we have defined as inverse 3D printing. Experiments are conducted to determine the printability of the printing materials and the optimum printing parameters. Once inverse moulds are obtained, a collagen slurry is cast in the moulds. The sacrificial mould is washed away leaving a porous collagen scaffold. Human umbilical vein endothelial cells (HUVECs) are seeded into the channels and SEM is used to observe the biocompatibility of these scaffolds. These thesis objectives are pursued to achieve the project's goals:

1. Surveying and characterizing printing properties of suitable biocompatible printing materials.
2. Repurposing a commercial 3d printer into a bioprinter and using it to indirectly bioprint collagen scaffolds.
3. Seeding human umbilical vein endothelial cells in the obtained scaffolds to observe cell adhesion and integration as well as biocompatibility of the scaffolds.

1.3 Thesis Organization

Generally, the first chapter highlights a general introduction and a motivation behind this research. This is followed by the research gaps as well as a definition of the objectives of this thesis.

The second chapter defines different materials that are used in the production of scaffolds for tissue engineering. There are also highlighted different methods employed in the fabrication of tissue engineering scaffolds using the materials mentioned above, and a deeper delve into different 3D printing mechanisms employed in tissue engineering. Methods for evaluating the mechanical strength of fabricated scaffolds are briefly discussed.

The third chapter focuses on the conceptual repurposing of a commercial 3D printer into a bioprinter. This includes finding suitable polymeric materials that can be used to replace the manufacturers printing materials. Protocols for the fabrication of collagen scaffolds are also highlighted here with a discussion of qualifying techniques that can be used to investigate the presence of internal microchannels in the fabricated channels.

The fourth chapter highlights data processing and a look at obtained results from experiments followed by relevant discussions which prove that our introduced method can create scaffolds with internal microchannels. A non-destructive method for channel observation OCT is also qualified as a possible method for obtaining internal images of the scaffolds without rendering any damage that would make them unusable post imaging.

The fifth chapter highlights cell culture experiments that were conducted on the scaffolds proving that the fabrication technique used and the resulting scaffolds are capable of supporting cells.

The sixth, and final chapter summarizes the findings presented in this research and recommends improvements that can be carried out in furtherance.

Chapter 2: Literature Review

2.1 Scaffolds and Scaffold Materials

Scaffolds can be in the form of a single layer (a thin film) or have a three-dimensional structure made up of many fused thin layers or one thick layer[22]. Scaffolds should be highly porous, have well-interconnected pore networks, and have consistent and adequate pore size for cell migration and infiltration. In addition, scaffolds must provide the necessary temporary mechanical support, not be toxic to the cells, and degrade once implanted to enable the cells to produce their own extracellular matrix, the 'natural scaffold' for the cells[43]. It is important to note that degradation of most synthetic polymers, both in vitro and in vivo, releases cytotoxic acidic by-products that may make the scaffold environment unideal for cell proliferation. The synthetic polymers also do not possess surface chemistry familiar to cells, which typically thrive on an extracellular matrix made mostly of collagen, elastin, glycoproteins, proteoglycans, laminin and fibronectin[44].

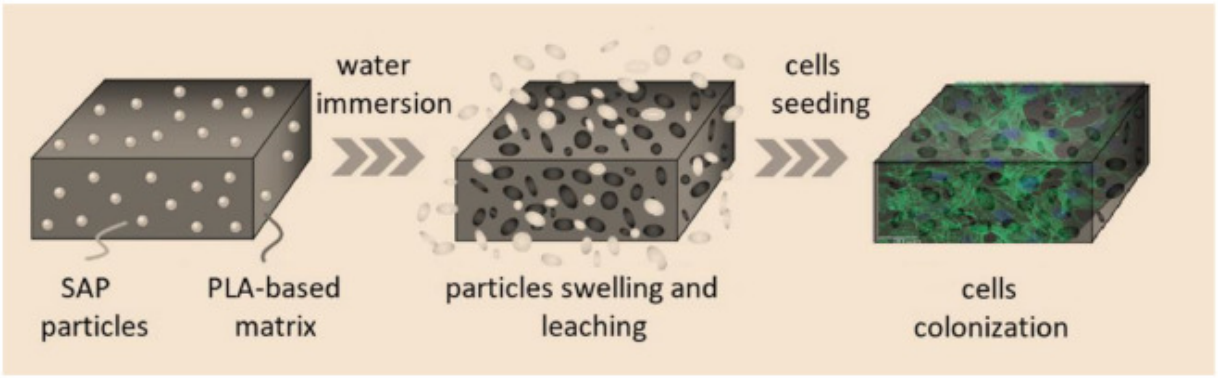

Figure 2.1: Scaffolds, like the one shown here by Sartore into which cells are seeded, that contain no internal microchannels will develop a necrotic core as oxygen and nutrients cannot reach deep into the scaffolds. Image adapted from ref[42] and reprinted by permission from Elsevier Ltd.

To produce scaffolds, we investigated two major classes of materials: ceramics and their composites and biodegradable polymers. These biodegradable polymers can be further broken into synthetic polymers, including thermoplastics like Polylactic acid (PLA), Polyglycolic acid (PGA), Polycaprolactatone (PCL), Polylactoglycolic acid (PLGA), among others as well as natural polymers like collagen, chitosan, alginate and fibrinogen[45]. Each class provides a unique set of advantages while being beset by a list of limitations.

2.1.1 Ceramics

In order to meet the need for combining bioactivity and bioresorbability properties that will aid in stimulating healing mechanisms in the body bioactive ceramics including tricalcium phosphate[46-47], hydroxyapatite[48], bioinert-alumina[49], zirconia[50], and bioactive glasses like 45S5 Bioglass (calcium sodium phosphosilicate)[51-52] have been used. The bioactive glasses form strong bonds with body tissue, including both hard and soft tissues[53-54]. While these bioactive ceramics are useful and provide the proper mechanical strength especially in hard tissue engineering, they are both brittle and stiff and present a difficulty when bioengineers try forming them into complex shapes[55]. This challenge can be solved by using relatively soft synthetic bioresorbable polymers. While these polymers can be fabricated relatively easily into shapes and structures that are complex[56-57], sometimes they will be weaker to meet the demand presented in vivo[58-59]. In order to harness the advantages of these bioactive ceramics as well as bioresorbable polymers, composites of the two classes of materials can be used[60], to meet the biological properties as well as the physical and mechanical requirements[61].

2.1.2 Natural Polymers

Natural polymers can be used as alternatives to synthetic polymers for the fabrication of scaffolds for tissue engineering.

2.1.2.1 Pectin

Pectin, an anionic polysaccharide, reduces serum cholesterol while inhibiting the release of histamine[62]. As a scaffold material, it has found application in skin tissue engineering to heal wounds[63]. Hyaluronic acid and glycosaminoglycan are biopolymers produced by the body on the cell membrane of fibroblasts and Golgi bodies respectively[64]. As scaffold materials, they have found use in wound dressing[65] as well as healing agents in glaucoma and retinal surgical procedures[64,66]. Hyaluronic acid promotes the migration and differentiation of cells as well as enhances the deposition of collagen. In osteoarthritic patients, these qualities of hyaluronic acid alleviate pain[67-68].

2.1.2.2 Chitosan

Chitosan is a derivative of chitin. Chitin occurs naturally and is abundant in the exoskeletons of insects and crustaceans[69]. Chitin is insoluble in a host of solvents[70]. Chitosan, however, is deacylated and presents a material suitable for scaffold production. As a scaffold, it has found application due to its cytocompatibility with many cell types including fibroblasts, hepatocytes, and myocardial cells. It has properties promoting the permeability of oxygen and cell migration as well as proliferation[71].

2.1.2.3 Alginate

Alginate, which can be naturally found in brown algae, has been used to produce scaffolds for tissue engineering[72]. In mammals, it cannot be degraded as mammals lack the enzyme necessary for the degradation of alginate[73]. As a scaffold material alginate is not easy to mould and thus cannot be used in fabricating scaffolds with complex shapes. It, however, has a property that minimizes bacterial infections[74].

2.1.2.4 Collagen

The predominance of collagen in human tissues[75] and different characteristic properties, for example, cell recognition signals, capacity to shape three-dimensional platforms of different actual adaptations, controllable mechanical properties, and biodegradability[76], make it an ideal raw material for tissue-engineered frameworks for different clinical applications, including cornea[77], skin, and bone tissue engineering[78-79]. The attractive quality of collagen as a biomaterial relies essentially upon the way that it is a normally abundant extracellular matrix (ECM) component and, accordingly, it is seen as an endogenous constituent of the body and not as foreign body. Collagen is a complex supramolecular structure and occurs in exceptionally different forms across various tissues. This makes collagen a suitable option in the production of scaffolds[24].

While the natural polymers offer natural cell binding properties and adequate biological properties, making them desirable as scaffold materials, there is variability in different batches and in biodegradation.

This results from differences in the animals from which they are obtained[80-81]. They are also difficult to manufacture compared to synthetic polymers[82] and pose a possible immune response in-vivo due to having peptide regions[83].

For the reasons mentioned above, collagen was settled upon as the material of choice in the fabrication of scaffolds in the research highlighted in this thesis.

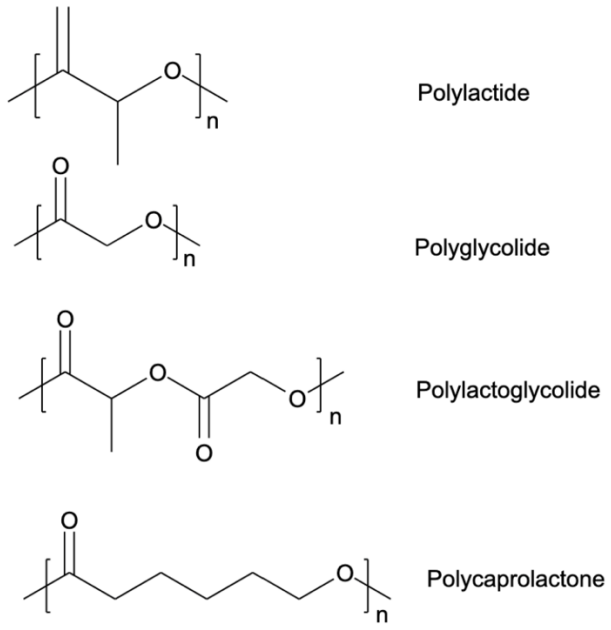

Figure 2.2: An illustration of the chemical backbone of PLA, PGA, PLGA and PCL. These synthetic polymers are used as scaffold fabrication materials and their rate of degradation, as well as rate of breakdown, can be adjusted by tuning their molecular weight as well as their structure.

2.1.3 Synthetic Polymers

While natural polymers provide the advantage of cell adhesion, their complex composition, possible immune response, and possible pathogen transmission make them undesirable[84].

Biodegradable synthetic polymers have a structure that can generally be controlled[85], their processing can be more flexible and they pose minimal immunological concerns[86]. While many types of biodegradable polymers have been used as scaffold materials for tissue engineering, aliphatic polyesters are the most widely used[87]. These polymers do not melt or dissolve in tissue culture conditions and normally degrade by the hydrolysis of their backbone ester groups[88]. Their degradation rate and breakdown by-products can be adjusted accordingly by tuning their molecular weight, composition as well as structure[89]. They include Polylactide (PLA) also known as Polylactic Acid[90], Polyglycolide(PGA) also known as polyglycolic acid[91], Polylactide-coglycolide (PLGA) also known as Polylactoglycolic acid[92], and polycaprolactone (PCL)[93].

2.2 Scaffold Fabrication Methods

Methods for producing scaffolds include Solvent-casting particulate leaching[94], solvent casting[95], gas foaming[96], melt moulding, solution casting, freeze drying[97], and electrospinning[98], among others. Unfortunately, these conventional scaffold fabrication techniques may have an irregular spatial distribution of pores and make it challenging construct internal channels within the scaffold[44].

2.2.1 Solvent Casting

In this fabrication technique, a mixture of the desired polymer, and ceramic is dissolved in an organic solvent, after which the resulting solution is cast into a designed mould. Exposing the mixture allows the solvent to evaporate leaving the desired scaffold[95,99]. This fabrication technique is relatively easy as it does not require expensive machines and/or equipment but is limited to simple shapes and cannot be used to fabricate scaffolds with complex shapes. Additionally, obtained scaffolds could be cytotoxic as a residual solvent may cause denaturation of proteins[100].

2.2.2 Solvent Casting Particulate Leaching

A mixture of porogen particles, polymer solution and inorganic granules are cast in a designed mould. The polymer solvent is evaporated, and the remaining mass is fractionated in a solvent that removes (leaches) the remaining particulates. This leaves behind a porous structure[94,101]. The porosity and pore size of the scaffold can be controlled by selecting desired porogen particles and the particles to polymer solvent ratio[102].

Like in the solvent casting method, this technique is inexpensive and relatively simple but also presents the inability to fabricate complex shapes. At the same time there may be an experience of cytotoxicity due to residual cytotoxic organic solvents after processing[100].

2.2.3 Freeze Drying

For this technique, a natural or synthetic polymer is dissolved in a suitable solvent. This polymer-solvent solution is then poured into a mould before it is frozen. Freezing can be done in liquid nitrogen or a freezer.

After lyophilization of the frozen solution, a porous scaffold is then obtained that can go on to additional processing[97]. The pore size can be adjusted by manipulating the ratios of the polymer to the solvent as well as adjusting the rate of freezing and the freezing temperature[103]. Scaffolds produced by this method have adequate interconnectivity, although the pores are quite irregular and small[104]. This method is suitable for natural polymers as it does not involve high temperatures which could otherwise denature natural polymers[105].

2.2.4 Gas Foaming

A desired liquified polymer is placed in a container; then, a high-pressure carbon dioxide gas is saturated in the container. A sudden pressure drop, by either increasing the container's volume or opening a valve creates pores in the polymer[96]. Pore sizes can be controlled by among other factors, the ambient temperature[106], the degree of pressure as well as the amount of time taken for depressurization[107]. Since this method used carbon dioxide which is non-toxic as it has no residual effects as in solvents, proteins cannot be denatured by the obtained scaffolds. The obtained scaffold, however, may lack pores in its membranes which may be a drawback[108].

2.2.5 Thermally Induced Phase Separation

In this method of scaffold preparation, a polymer/ceramic mixture in the desired proportions is dissolved in a volatile organic with a low melting point. This solution is then rapidly cooled so that phase separation can be induced. This forces the polymer/ceramic mixture into the interstitial spaces. The solvent is then removed via sublimation leading to the obtaining of a porous scaffold[109]. The scaffold architecture, including the pore size and shape, can be controlled by selecting the polymer and solvent types. If desired, this process can be followed with freeze-drying to improve the porosity of the scaffolds[110]. Since the pore size produced is limited, the scaffolds produced by this method have a very limited application[111].

2.2.6 Electrospinning

An electrical field is applied to a needle that contains a polymer solution. Since this polymer is now charged, it starts flowing out of the needle onto a collection plate. The collection plate has a potential difference, and this causes the solution to elongate as it spreads across the plate, creating a porous scaffold[98].

Functional scaffolds can be created by optimizing the fabrication technique by adjusting such parameters as the length and diameter of the needle, the type and concentration of the polymeric solution, the potential difference as well as the flow rate of the polymer through the needle to the collection plate[112].

The ability to control the potential difference gives these scaffolds obtained by this type an advantage, in that, they can have fibres that are up to nano to micro-scale and can be highly porous. However, the fact that an organic solvent is used here means a risk of scaffold toxicity to the cells unless this polymer is completely removed[113-114].

2.3 3D Printing as a Scaffold Fabrication Technique

3D printing is an additive manufacturing method where the material is laid in a layer-by-layer fashion on a 'print bed' to achieve a final 3D structure[115]. 3D printing for scaffold fabrication has been developed as advanced technology to overcome the limitations of conventional scaffold fabrication methods[116]. It may ultimately lead to the production of matrix scaffolds capable of more effectively promoting the regeneration of functional tissue by being a promising tool to fabricate scaffolds with high precision and accuracy[117], creating intricately detailed biomimetic 3D structures[118].

This is because 3D printing makes it possible to design complex shapes directly or indirectly using a 3D printer into scaffolds for use in tissue engineering[119]. These complex shapes would otherwise not be possible while using the conventional scaffold fabrication techniques[120].

Scaffold 3D printing techniques can be split into direct 3D printing, where a 3D printer prints the scaffold itself[121], and indirect 3D printing, where a sacrificial mould is first 3D printed by any of the different 3D printing methods and this is then used to create the scaffold that can then be used for tissue engineering[122-123].

The techniques currently being used to achieve 3D printing of scaffolds, which involve a layer-by-layer process, include, but are not limited to, direct 3D printing, fused deposition modeling (FDM) stereolithography (SLA), and selective laser sintering (SLS).

Moulds can also be printed into which scaffold material is poured as shown in wax-based indirect 3D printing as shown in **Figure 2.3**. These techniques can be used to produce scaffolds starting from millimeter- to nanometer-sized scaffolds[124]. It is also important to notice that the terms: solid freeform fabrication, additive manufacturing and 3D printing became synonymous over the past two decades and are now used interchangeably[1].

Materials used for 3D printing for scaffold fabrication include ceramics like hydroxyapatite and calcium silicate, tricalcium phosphate, synthetic polymers like PLA, PCL, PGA and PLGA [125] and some natural polymers like gelatin methacrylate (Gel-MA), and collagen-based hydrogels[126]. These materials have been discussed in the preceding sections of this thesis. Composites of these materials have also been used in fabricating scaffolds for tissue engineering[127].

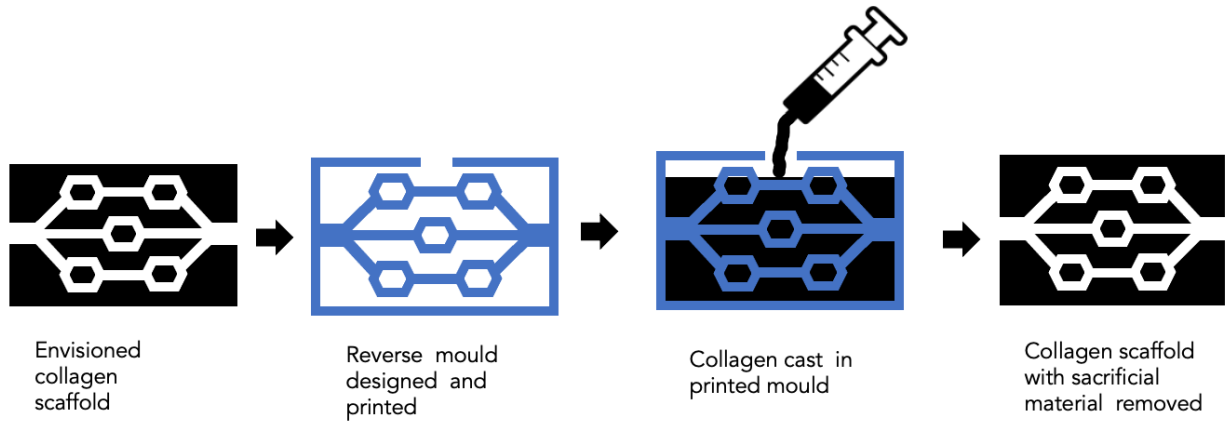

Figure 2.3: An illustration of the indirect 3D printing method for fabricating collagen scaffolds whereby an inverse mould is printed on a 3D printer before the collagen is cast in this mould and the sacrificial mould is removed by dissolution. Adapted from[29].

Printing materials for 3D printing of these scaffolds can be in the form of solid pellets, solid chunks or sticks, filaments wound into a spool, powders and liquids[128]. Materials suitable for different 3D printing methods are highlighted in **Table 2.1.**

Most 3D printing processes follow a similar methodology, where computer-aided design (CAD) software will be used to design the desired scaffold[129].

An alternative is to use two-dimension slices from medical images such as computed tomography (CT) scans as well as magnetic resonance imaging MRI scans to create 3D designs that can be further sliced using a slicer software into the 3D printers machine code language[118,130].

This code will then be fed into the 3D printer's computer and the 3D printer will start 'printing' the scaffold layer-by-layer manner on the print bed[131].

Below are discussed some 3D printing methods used in scaffold fabrication.

2.3.1 Fused Deposition Modelling (FDM)

In Fused deposition modelling, thermoplastic polymer filaments wound in a spool, are normally unwound heated above their glass transition temperatures as they are pushed through a nozzle onto a print bed. It hardens and sets when the heated thermoplastic polymer filament comes into contact with the cooler print bed.

This process continues for the entire layer of the scaffold. After a layer is done, either the print head will move a step up or the print bed will move a step down and the process will be repeated for a second layer. This process will repeat itself until the print process reveals the desired scaffold[132].

Overhangs need to be supported; therefore, the slicer software will create support structures to support overhangs as 'you cannot print on air'[133]. Additional processing may be done on the scaffold to remove the overhangs and any print defects due to excessive extrusion[134]. The fused deposition modelling method is illustrated in **Figure 2.4.**

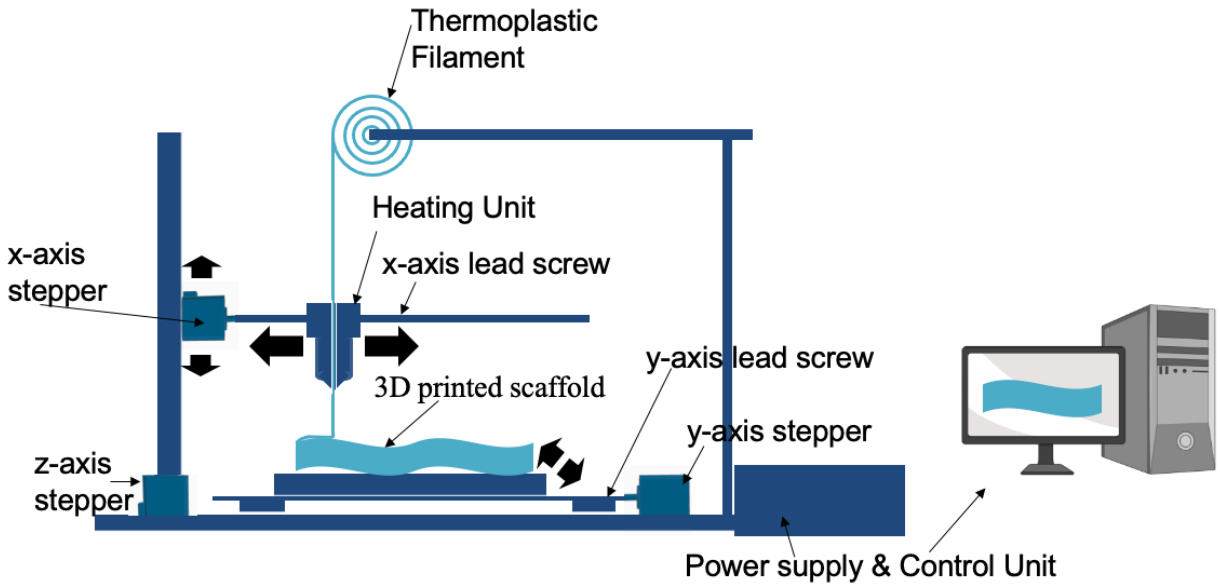

Figure 2.4: An illustration of the fused deposition modelling 3D printing method. The thermoplastic filament is melted and extruded through the heating unit and laid in a layer-by-layer manner on the print bed until the scaffold is printed.

2.3.2 Selective Laser Sintering (SLS)

In this scaffold fabrication technique, a layer of powder is spread on the print bed surface. A laser will then sinter the powdered particles together following the pattern of the scaffold design according to the CAD. This pattern continues until the entire layer is done.

The print bed will move down, and a fresh layer of powder will be applied to the initial layer. The laser sinters the new layer according to the desired pattern. This process will repeat itself until the scaffold design is completely printed[135]. Overhangs do not need a printed support structure as the powder will support any existing overhangs[136]. Cleaning of the scaffold may need to be performed[137]. The selective laser sintering method is illustrated in **Figure 2.5.**

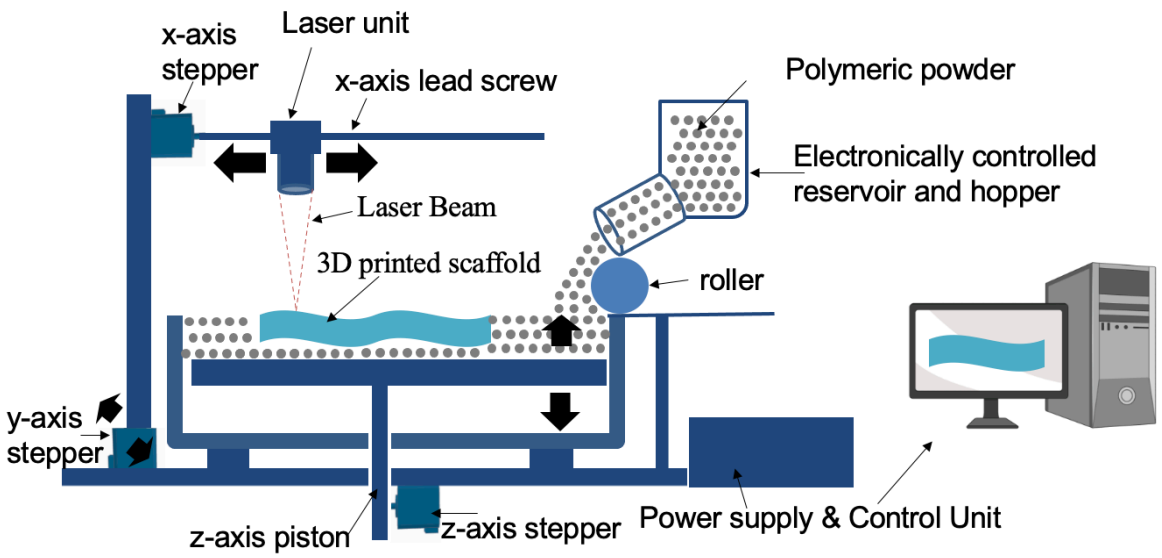

Figure 2.5: An illustration of the selective laser sintering method of 3D printing tissue engineering scaffolds. The polymeric powder is laid on the print bed before a laser beam melts the first layer according to the sliced g-code of the scaffold CAD. A fresh layer of powder will be spread on the complete print and sintered. This process continues until the entire scaffold is printed.

2.3.3 Stereolithography (SLA)

This fabrication technique involves using a liquid polymer to form a scaffold using a light-initiated chemical reaction[138]. In this process, a photocurable liquid polymer is deposited on a surface. This surface medium is exposed to UV light in the range of 300-400nm[139-140]. On the curing of the first layer, it is overlayed with the liquid polymer, and the process continues until the entire scaffold is obtained[141]. This is illustrated in **Figure 2.6.**

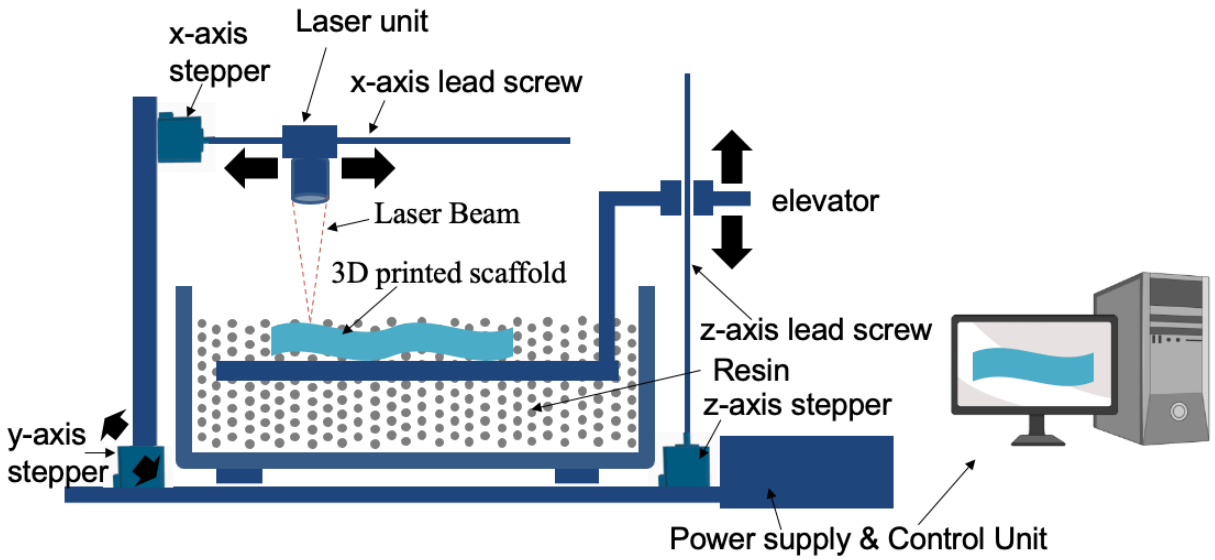

Figure 2.6: An illustration of the stereolithography method of scaffold 3D printing. A laser beam heats and solidifies a layer of polymer resin onto the print bed to create the first layer. The print bed moves into the resin to allow a new layer to be created on top of the first one. This process continues until the entire scaffold has been printed.

2.3.4 Wax Printing

Wax printing has been used in indirect 3D printing for scaffold fabrication. Wax droplets of print material and support material will be deposited on the print bed according to the desired scaffold design. On completion of the layer, a relevant amount of time will be allowed for the material to cool down. A mill will then be used to flatten the layer, after which a new layer is printed. This printing method continues until the entire scaffold is printed[1,142].

Table 2.1: Materials with their suitable scaffold 3D printing processes

Form	Examples	Suitable 3D – Printing Processes	Reference
Solidifiable Fluid	Photopolymer resins, temperature-sensitive polymers, ion cross-linkable hydrogels, ceramic paste	Stereolithography	139-140
		Polyjet	143
		Digital Light Processing (DLP)	144
		Microextrusion	145
Non-brittle filament	Thermoplastics: PLA, PCL, ABS,	Fused deposition modelling	132
Fine powder	Plastic fine powder, ceramic powder, metal powder	Laminated Object Manufacturing	146
		Ultrasonic Consolidation	147
		Selective Laser sintering	135-137
		Electron beam melting	148
		Laser engineering net shaping	149

2.4 Bioprinting

Bioprinting is the printing of inks that are embedded with a suspension of cells.

Current bioprinting technologies which are based on 3D printing with live cells are extrusion-based bioprinting (EBB), droplet-based bioprinting (DBB) or laser- based bioprinting (LBB), as depicted in **Figure 2.7** below. In EBB, a cell-laden bio-ink containing biomaterials and biologically active substances is pushed by a syringe through a needle onto a print bed in a spatially controlled pattern in a layer-by-layer manner until the structure is completely built[150].

Shear stress has been known to reduce cell viability, and therefore an optimum flow rate through the needle must be determined for optimal cell survival[151].

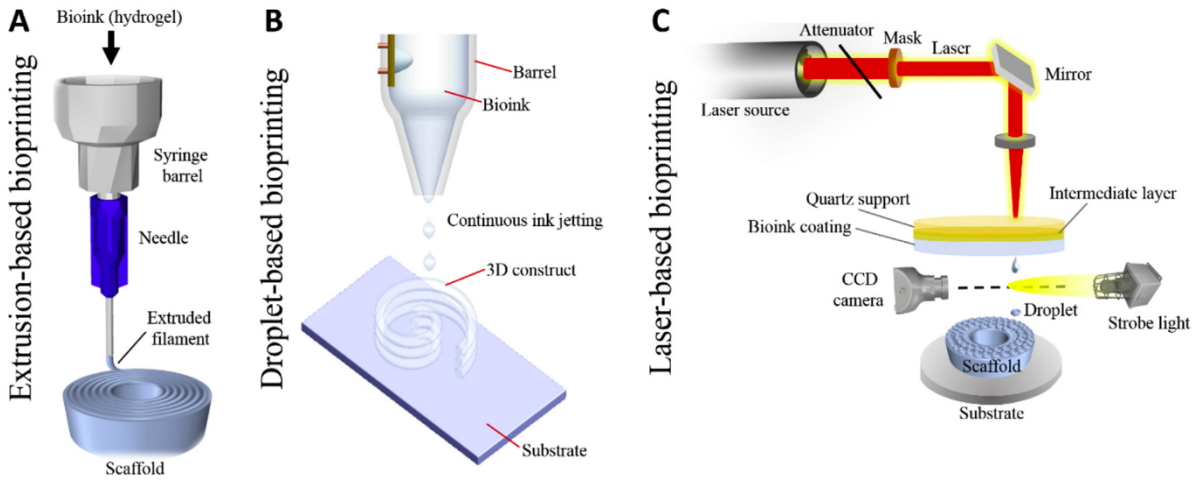

Figure 2.7: Bioprinting Techniques: (A) Extrusion-based bioprinting, a bio-ink is pushed from a syringe barrel onto a print bed in a constant stream. (B) Droplet-based bioprinting, the bio-ink is pushed from a print head onto the print bed in continuous droplets. (C) Laser-based bioprinting a laser melts a bio-ink coating from embedded onto a quartz support layer. The molten bio-ink falls onto the print bed. Figure adapted from [6] and reprinted from Biotechnology Advances with permission from Elsevier Ltd.

In DBB, bead-sized droplets of a cell-laden bio-ink under tension are deposited in a drop-by-drop manner in a controlled pattern onto a print bed[152]. The initial bio-ink layer may be allowed to cure before the next layer is printed on top of it[153].

Electrostatic[154] and piezoelectric actuators may be employed for the precise deposition of the droplets. Shear thinning challenges may also lead to decreased cell survival in DBB[6,152]. Different bio-inks and their corresponding suitability are highlighted in **Table 2.2.**

Table 2.2: Collagen-based bio-inks with appropriate bioprinting methods. (Adapted from[21], with permission from MDPI Bioengineering.)

Bioprinting Method	Collagen-Based Ink Formulation	Outcome	Reference
Extrusion	Methacrylated type I collagen; Sodium alginate	Fabrication of structures resembling native human corneal stroma with cell-laden bio ink via extrusion bioprinting.	155
	Collagen Type I; Alginic acid sodium salt from brown algae; CaCl2 solution	Core-sheath coaxial extrusion of alginate/collagen bio-ink with CaCl2 allows the creation of scaffolds with low collagen centration despite its low viscosity.	156
	Rat tail type I collagen; Gelatin (type A); Sodium alginate	Extrusion bioprinting of collagen scaffold via gelatin/alginate system with controllable degradation time based on amount of sodium citrate during incubation.	157
	Type I collagen was extracted from tendons obtained from rat tails	Identified storage modulus as the best predictor of collagen bio-ink printability during deposition.	158
	Type I collagen, Matrixen-PSP; Decellularized extracellular matrix (ECM); Silk Fibroin(SF)	Hybrid collagen/dECM/SF scaffold with enhanced cellular activity and mechanical properties. Enhanced cell differentiation, mechanical properties, amenable for hard tissue regeneration.	159
	Atelocollagen Type I powder	Novel self-assembly induced 3D printing to produce macro/nano porous collagen scaffolds with reasonable mechanical properties, excellent biocompatibility and mimicking native ECM.	160
Extrusion/Inkjet	Lyophilized collagen type 1 sponge derived from porcine skin	Development of a one-step process to produce a 3D human skin model with functional transwell system. Cost-effective compared to traditional transwell cultures.	161
Inkjet	Type I rat tail collagen; poly-d-lysine	Fabrication of neuron-adhesive patterns by printing cell-adhesive layers onto cell-repulsive substrates.	162
	Collagen (Calf skin)	Cell aggregates printed between layers of collagen gels suitable for tissue engineering	163
	Collagen (rat-tail); collagen (calf skin)	Low-cost, high-throughput surface patterning with collagen and potentially, other proteins.	164
	Collagen Type I	Fabrication of in vitro cancer microtissues via collagen inkjet printing. Four individual microtissues within one 96-well plate well, maintained for up to seven days.	165
	Collagen: Type I rat tail collagen; Fibrinogen; Thrombin	Collagen bio-inks and Fibrin/Collagen bio-inks unsuitable for in situ inkjet bioprinting.	166
	Type I acidic collagen; Agarose (low gelling temperature)	Fabrication of 3D corneal stromal structure with optically properties similar to native corneal stroma. Potential as a clinical or experimental model.	167
	Acidic collagen solution; Agarose (low gelling temperature)	MSC branching, spreading and osteogenic differentiation controlled by collagen concentration; Osteogenic potential (bone tissue engineering).	167
Laser-assisted	Collagen Type I (Rat-tail)	Fabrication of cell-laden skin tissue using laser-assisted bioprinting, in vivo potential. Skin tissues consist of: a base matriderm layer, 20 layers of fibroblast and 20 layers of keratinocytes.	168
	Collagen (Rat-tail)	Multicellular collagen skin tissue constructs printed using laser-assisted bioprinting, Keratinocyte and fibroblast layers did not intermix after 10 days. Mimics tissue-specific functions (e.g. gap-junction).	169
	Type I collagen (rat) solution; Nano hydroxyapatite (nHA)	In situ printing of cell-laden collagen-based ink via laser assisted bioprinting allow bone regeneration (mouse calvaria defect model). Contact free printing method is sterile with clinical potential.	170
	OptiColt human Col I; Ethylenediaminetetraacetic acid (EDTA) human female AB blood plasma; Thrombin from human plasma	Fabrication of 3D cornea tissue using novel human protein bio-inks via laser-assisted bioprinting. Novel bio-ink is biocompatible, without requiring additional crosslinking. The first study to demonstrate laser-assisted bioprinting for corneal applications using human stem cells.	171

2.5 Crosslinking of Collagen Scaffolds

Once printed collagen scaffolds need to be crosslinked. This strengthens the scaffold shells and reduces the telopeptide regions, reducing the chances of immune response in vivo[172]. Reconstituted collagen assemblies lack sufficient strength and may disintegrate upon handling or collapse under pressure from surrounding tissues in vivo[173].

At the same time, the rate of biodegradation must be customized for specific application[174]. In order to prevent denaturation at 37ºC, control the rate of degradation and improve the mechanical properties[175], different methods are used to crosslink the collagen scaffolds. The three main methods are chemical, physical and biological and each has its own advantages or disadvantages. Mechanisms for these methods are highlighted in **Figure 2.9.**

Chemical methods include using aldehydes[173] e.g. glutaraldehyde[176], isocyanates[177] e.g. hexamethylene diisocyanate[178] and carbodiimides[179] e.g. 1-ethyl-3-(3-dimethylaminopropyl)carbodiimide[180]. Carbohydrates and plant extracts can also be used. EDC/NHS cross-linking involves the activation of carboxyl groups, which then spontaneously bond to amine groups of lysine and hydroxylysine residues of collagen[181].

After extensive washing foreign cross-linking molecules are removed, resulting in collagen devices of good cytocompatibility, and reduced susceptibility to calcification[182], but with improved mechanical properties and resistance to proteolytic attack[183-184].

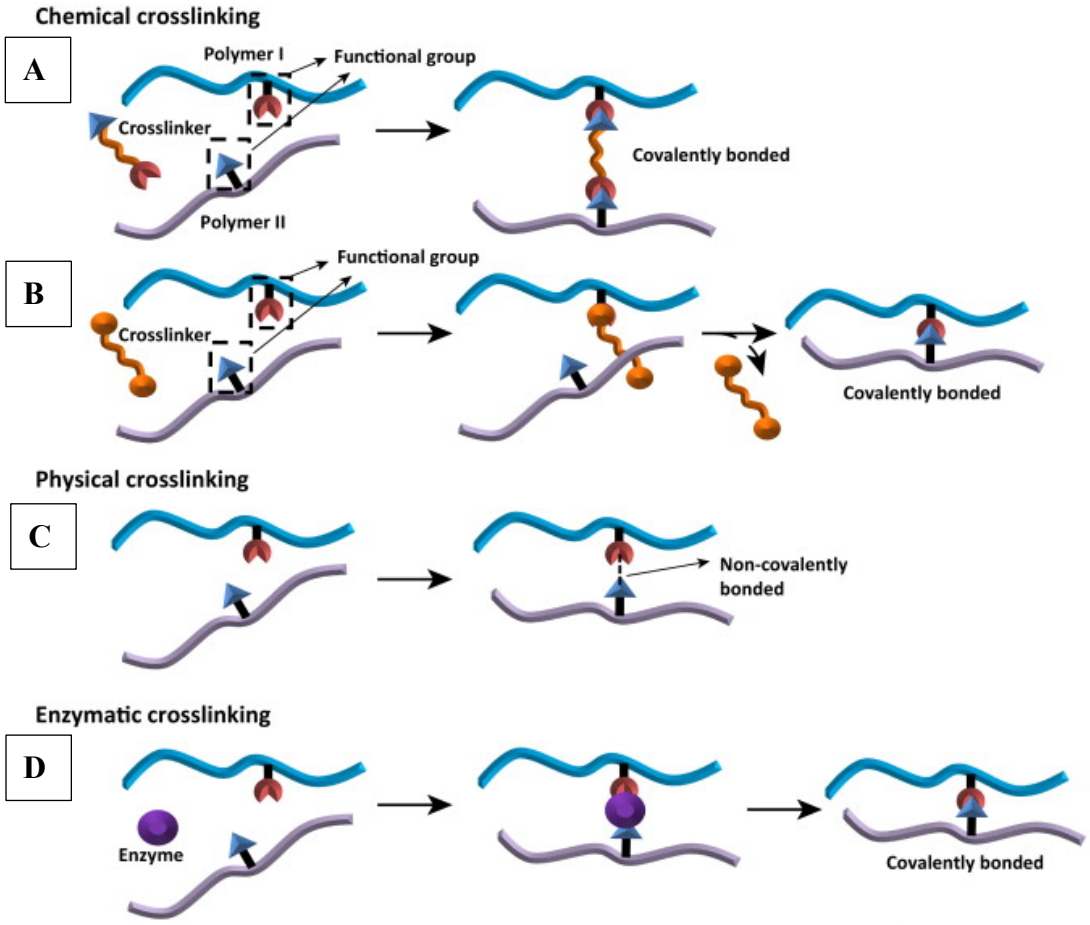

Figure 2.8: A schematic illustration of four types of crosslinking. **(A)** Chemical Crosslinking showing the crosslinking agent included in the bond between polymers. **(B)** Chemical crosslinking in which the crosslinking agent is not included in the bond between the polymers. **(C)** and **(D)** illustrate physical crosslinking and enzymatic crosslinking respectively. Image adapted from[185] and reprinted from Trends in Biotechnology, with permission from Elsevier Ltd.

Chemical methods sometimes have cytotoxic effects[186]. In order to minimize these cytotoxic effects, physical methods are used[187]. These include dehydrothermal treatment[187], UV irradiation[188-189] and photoreactive agents[190], e.g. Rose Bengal[191] and riboflavin[192].

Unfortunately, UV irradiation can have some denaturation effects on collagen and all physical methods are a lot weaker than the milder chemical method and are often associated with collagen denaturation (especially the DHT treatment), imposing the need for introduction of chemical crosslinks (usually carbodiimide).

For biological methods, Tissue-type and microbial transglutaminase (TGase) has been utilized to stabilize collagen-based[193] and gelatin-based[194] materials mimicking the enzymatic in vivo collagen cross-linking pathway. Despite their superior cytocompatibility to chemical approaches, it is worth pointing out that both physical and biological methods are very weak, often weaker than the mildest chemical approach[195-196]. Further, the physical methods can cause collagen denaturation[187]. As such, the quest for the optimal collagen cross-linker continues.

2.6 Collagen Scaffold Characterization

When using collagen scaffolds with the aim of tissue engineering, scaffold microstructure properties including porosity, permeability, mean pore size, pore shape, interconnectivity, specific surface area; and mechanical properties including stiffness and Young's modulus have been shown to significantly influence cell behaviors such as cell adhesion, cell migration, cell growth and as well as cell differentiation[13].

SEM micrographs are shown in **Figure 2.10.** These have been used to observe the scaffold architecture. While **Figure 2.11** shows 2-D tomographic reconstruction of a through the section of scaffolds using Matlab code to show a cell fitting growth.

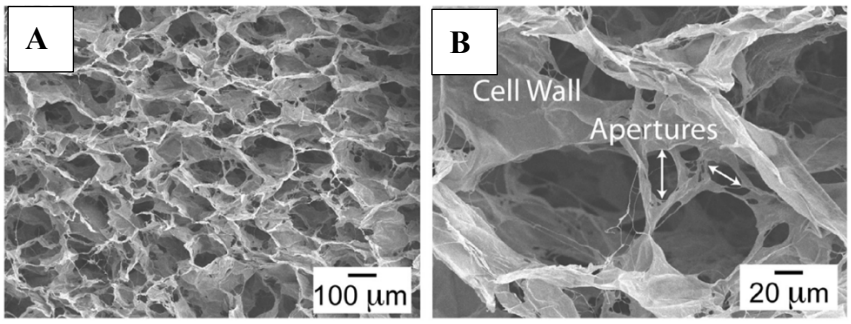

Figure 2.9: SEM micrograph of a section through a dry collagen-glycosaminoglycan scaffold. A and B show different magnifications of the same scaffold. Image adapted from[197] reprinted from Acta Biomaterialia with permission from Elsevier Ltd.

The stress–strain curve for a low-density, elastomeric open-cell foam in compression is characterized by three distinct regimes: a linear elastic regime (controlled by strut bending), a collapse plateau regime (struts buckling and pore collapse) and a densification regime (complete pore collapse throughout the material)[198]. This can be seen in **Figure 2.12** below.

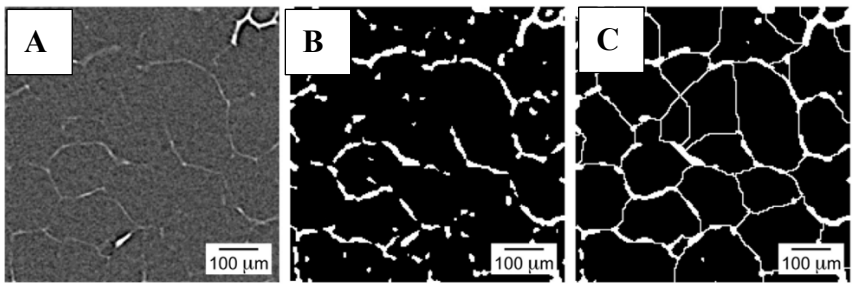

Figure 2.10: (A) A 2D tomographic reconstruction of section though collagen-glycosaminoglycan scaffold. **(B)** shows the same micrograph after thresholding and **(C)** shows the same image after a cell fitting procedure using a voxel-growth constrained algorithm in MATLAB. Image adapted from[197] reprinted from Acta Biomaterialia with permission from Elsevier Ltd.

2.6.1 Experimental procedures for Young's Moduli

As opposed to dense solids, scaffolds are cellular solids with foamlike structures. The Young's modulus (E^*) and elastic compressive strength δ^*_{el}, also called the compressive plateau stress of elastomeric open-cell foam, depending on the foam relative density, ρ^*/ρ_s, Young's modulus of the solid from which the foam is made, E_s, and a constant related to the cell geometry. The complex geometry of foams (and scaffolds) is difficult to model exactly; instead, dimensional arguments rely on modeling the mechanisms of deformation and failure in the foam (edge bending and the critical load for strut buckling), but not the exact cell geometry[199]. This illustration can be seen in **Figure 2.12**

For elastomeric cellular solids like collagen, E* and δ^*_{el} are given by:

$$E^* = C_1 \cdot \left(\frac{\rho^*}{\rho_s}\right)^2 \cdot E_s \qquad \text{Eq. 2.1}$$

$$\delta^*_{el} = C_2 \cdot \left(\frac{\rho^*}{\rho_s}\right)^2 \cdot E_s \qquad \text{Eq. 2.2}$$

Where C_1 and C_2 are constants of proportionality related to the cell geometry. Both, E* and δ^*_{el} are expected to be independent of the cell or pore size. Harley[200] used the experimental setup as shown in **Figure 2.13** to perform bending tests on scaffold struts. The following formulas were used to determine Young's modulus and force.

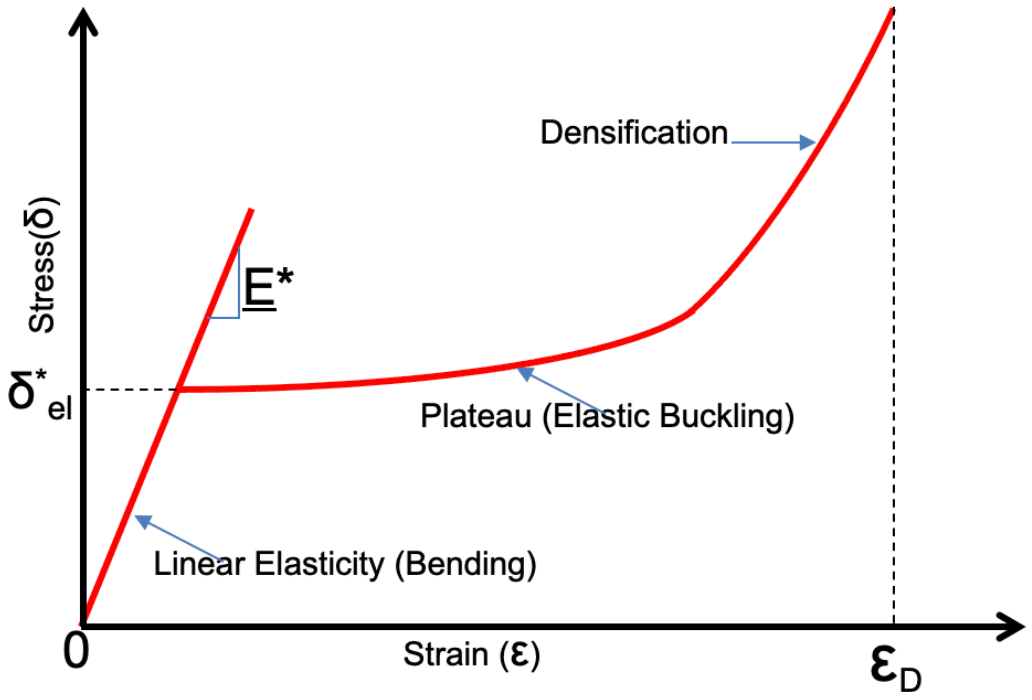

Figure 2.11: Uniaxial stress-strain curve for compressive loading of elastic-plastic foam solids. A collagen scaffold is a cellular elastic-plastic foam solid. At low stresses, there is linear elasticity followed by a long collapse plateau eventually truncated at a regime of densification where the stress rises sharply. Image adapted from Cellular Solids[199] and redrawn in Adobe Illustrator.

$$F = K_{cantilever} \cdot d_2 \qquad \text{Eq. 2.3}$$

$$E_s = \frac{64 \cdot (K_{cantilever} \cdot d_2) \cdot x^3}{3 \cdot \pi \cdot D^4 \cdot (d_t - d_2)} \qquad \text{Eq. 2.4}$$

They used the cellular solids relationship introduced in Eq. (2.1), the measured strut modulus E_s and the measured scaffold ρ^*/ρ_s to calculate the theoretical scaffold Young's modulus E^* and the elastic compressive strength δ^*_{el}.

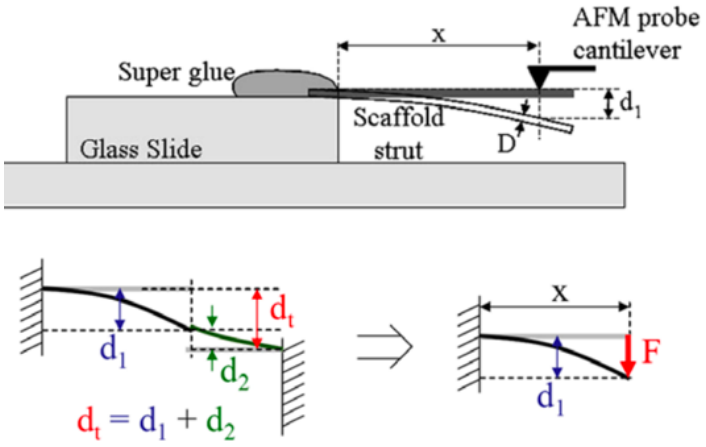

Figure 2.12: Scaffold bending test experimental setup and schematics. The schematics show how the bending system is used to calculate scaffold modulus in terms of the measured parameters from equation 3a and 3b. Image adapted from[200] and Reprinted with permission from Acta Biomaterialia.

The calculated E^* and δ^*_{el} were compared with the experimentally measured values over a range of ρ^*/ρ_s to understand better the relationship between the macroscopic and microscopic mechanical properties of the collagen composite scaffolds. These results are recorded in **Figure 2.14**[200].

Scaffold architecture can be observed using optical microscopy, scanning electron microscopy or X-ray computed tomography, while permeability can also be obtained using pressure gradient flow rate measurement[201].

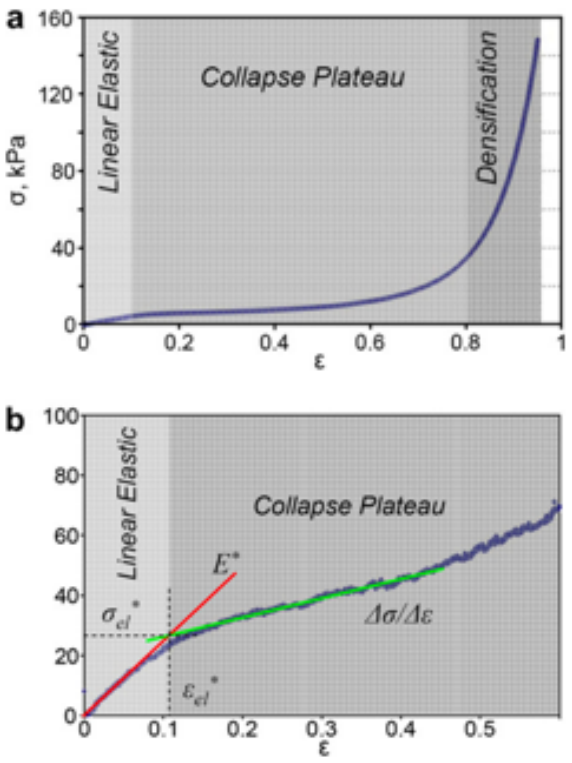

Figure 2.13: Compressive stress-strain curves are shown below for **(A)** dry and **(B)** hydrated composite collagen-glycosaminoglycan composite scaffolds. Adapted from[200] and reprinted with permission from Acta Biomaterialia.

2.6.2 The Effect of Permeability on Collagen Characterization

Permeability is a strong function of porosity level and pore architecture, particularly pore connectivity. There is also a more complex dependence on cell architecture since the tortuosity of individual channels and possible existence of high flow rate paths can also affect the measured permeability[202].

Furthermore, the permeability of a biological structure, such as a scaffold, can play an important role in its performance, affecting nutrient and oxygen diffusion, waste removal, and cell migration into the scaffold. Scaffold permeability is defined by a combination of five important parameters: (1) porosity, (2) pore size and distribution, (3) pore interconnectivity (or tortuosity), (4) fenestration (pore interconnection) size and distribution, and (5) pore orientation[203]. The fluid mobility (K, units of m^4/Ns) of a scaffold is another intrinsic property defining fluid flow through a porous material and is defined as the material permeability normalized by the viscosity of the fluid (μ, units of Pa·s):

$$K = \frac{\kappa}{\mu} \qquad \text{Eq. 2.5}$$

Where *k* is permeability. Darcy's law[13] states that permeability, k, can be calculated from Eq. 2.6, where *Q* is the volumetric flow rate (ml/s), ΔP is the pressure difference across the sample (N/m^2), *l* is the length of the specimen through which the fluid flows (m), A is the sample cross-sectional area in the direction of flow (m^2), and μ is the viscosity (Pa·s) of the fluid

$$\kappa = \frac{Q \cdot l \cdot \mu}{\Delta P \cdot A} \qquad \text{Eq. 2.6}$$

The rig in **Figure 2.14** allows small pressure differences to be imposed across the scaffold, defined by the hydrostatic head of water ($\Delta P = \rho hg$), since the bottom of the scaffold is exposed to the atmosphere.

The pressure was held constant across the scaffold (thickness L) and the volumetric flow rate (Q) of distilled water through the scaffold was measured (from the mass of water passing through the scaffold at each time). This mass was measured, using a Mettler PE 360 balance with a precision of 1 mg, and converted to volumetric flow using the fluid density (q = 0.998 Mgm^3). From Q, the sectional area (A) and the pressure gradient, ΔP/L, the specific permeability, *k*, was calculated using Darcy's Law as shown above[197].

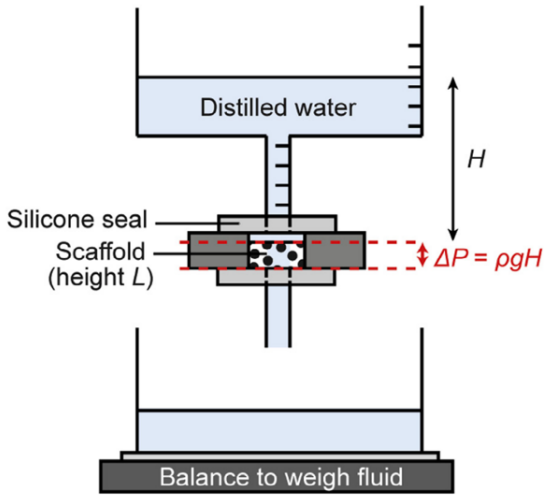

Figure 2.14: Schematic of a to measure scaffold permeability. Adapted from[197] and reprinted from Acta Biomaterialia with permission from Elsevier Ltd.

The average measured value of the specific permeability *k* was found to be 4.8 x 10^{10} ± 2.2 x 10^{10} m^2. This is in good agreement with predictions based on Computational Fluid Dynamics (CFD) simulation of the flow of water through tomographically captured structures which gave a value of about 2 x 10^{10} m^2. This is attributed to scaffold deformation (creep) even under the small pressure gradient applied in their study[197].

3D printed Collagen scaffolds have an isotropic cell structure and extensive connectivity between the adjacent cells of the scaffolds. This structure has significant implications for the scaffolds' stiffness as well as permeability. It has shown that the stiffness of these scaffolds in both hydrated and dry states is extremely low[13]. Scaffold permeability decreases with decreasing pore size and with increasing compressive strain[204].

Chapter 3: 3D Printer and Experimental Methodology

3.1 Solidscape 3D Printing Mechanism

A phase-change jet printing system was used to fabricate the channels. As shown in **Figure 3.1** and a schematic in **Figure 3.2**, the Solidscape T612bt (Stratasys Inc.) is a phase-change jet printing system that uses wax-based materials for build and support materials named Induracast and Indurasupport, respectively by the manufacturer.

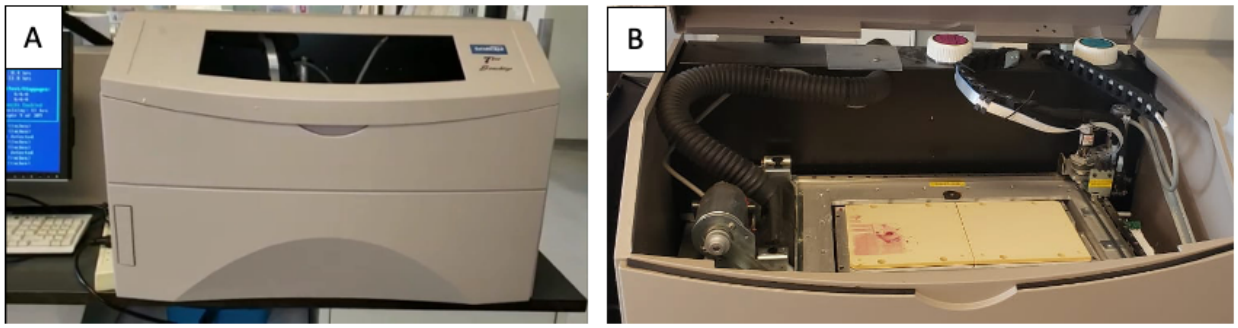

Figure 3.1: Images of the Solidscape T612BT 3D printer exterior A. and interior B. of the printer with the lid open to show the print bed (yellowish foam), material tanks (Blue lid – build and Red lid – support), the cutter, on the left with the black hose that is connected to an out of view vacuum that sucks and stores milled material. The print head system, backed away on the right rear with an attached head microprocessor and piezos to actuate material deposition on the print bed.

Induracast has a blue dye while Indurasupport has a red dye for visual differentiation. Induracast melts at ~115ºC while Indurasupport melts at ~85ºC. The system has two of each of the material reservoir tanks, heated lines and print heads, one dedicated to the build material and the other dedicated to the support material.

Solidscape documentation claims that the printer prints with high precision, with an error of ±0.25mm. This high precision has been achieved by using a microprocessor on the printhead which coupled with electrically actuated piezos determines the amount of material that will be deposited with each actuation. The print heads have a hold voltage set at 50V and fire voltage set at 20V and release material at a frequency of 9000Hz in tiny microdroplets. The material is laid down line-by-line for both Indurafill and Induracast. Once a layer is completed, a mill will flatten the layer with milled chips being vacuumed and stored in a filter. The bed moves a step below to commence the printing of a new layer. This process continues until the entire structure is printed.

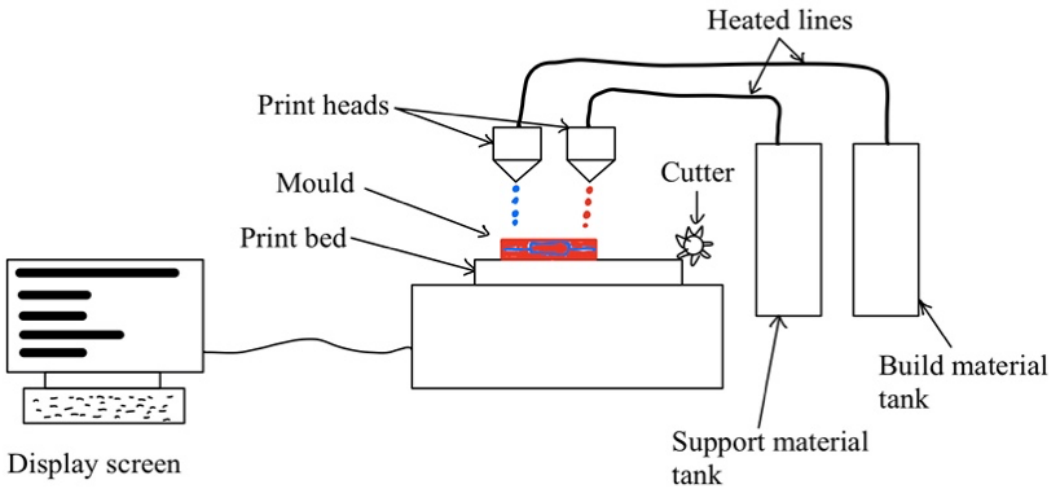

Figure 3.2: A schematic of the principle of operation of the Solidscape T612BT 3D Printer. Material from the build and support tanks is laid in a layer-by-layer manner on the print bed. The cutter smoothens each layer before new material for a new layer is laid. The screen is used to monitor print progress as well as visualize commands manipulating the print operation.

3.2 Material Survey for the Bioprinter Repurposing.

Induracast and Indurafill are cytotoxic to cells. This research sought to establish a biocompatible material that could be used to replace them. An extensive literature review was conducted looking at biocompatible waxes. Materials that were surveyed include: Alkyl Polyglucoside[205], capryloyl glycine[206], Dilinoleic acid[207], Ethylhexyl stearate[208], ethyl stearate[209], Isostearyl neopentanoate[210], Lauric acid[211], Linoleic acid[212], polyethylene glycol[213], polyethylene oxide[214], polyvinyl alcohol[154], Propylene glycol laurate[215], Stearyl alcohol[216] , Stearic Acid[217] and Stearoyl Sarcosine[218].

Among the factors that were observed in the search for a suitable biocompatible printing material were solubilities, melting points, relative rheology as well as availability. For solubility, water and ethanol were the most relevant solvents in washing away the build and support materials. Therefore, the chosen material had to be soluble in water, ethanol or both. Melting points were necessary to consider as the material had to be in solid form when deposited in the print tanks and had to melt within the manufacturer's material melting points. Materials needed to have melting points of between 40^{o}C and 200^{o}C. The materials needed to have a viscosity that was relatively similar to that of molten induracast and indurasupport so that it could flow through the printer's heated lines as well as the print heads. Ultimately the material needed to be relatively cheap and available from the list of available suppliers at a low cost. This was necessary as downstream, this research aims at producing scaffolds with high throughput, and a high cost would be a limiting factor.

After the literature the materials that were observed to be likely candidates were polyethylene glycol, polyvinyl alcohol, stearic acid, polyethylene oxide and ethyl stearate. Polyethylene Glycol (PEG) was found to be soluble in both water and ethanol and had a melting point of 64ºC. Polyvinyl alcohol was soluble in water but had a high melting point. Stearic acid was soluble in ethanol and had a melting point of 68ºC. Polyethylene oxide and ethyl stearate were soluble in water and ethanol respectively and had a melting point of 57ºC and 39ºC, respectively. Only PEG and SA were tested for rheology. Their viscosities were found to be relative to those of Induracast and Indurasupport. From a series of studies highlighted in the following sections, Stearic acid (SA) was determined as a suitable replacement for Induracast while polyethylene glycol (PEG) was used as a suitable replacement for Indurafill in this research.

Table 3.1: Comparing the desirable properties of 3D printer repurposing materials to replace induracast and indurasupport in the repurposed 3D bioprinter.

Material	H_2O sol. (mg/ml)	C_2H_5OH	M.P (^OC)	Rheology (100ºC)
Polyethylene Glycol	630 mg/ml, 20 °C[219]	✓	**64**	18 mPa.s (100ºC)
Polyvinyl Alcohol	5 mg/ml, 30ºC[220]		200	6.8 - 9.2 mPa·s (200ºC)
Stearic Acid		✓	**68**	5 mPa.s (100ºC)
Polyethylene Oxide	13 mg/ml, 72ºC[221]		57	12-50 mPa.s in H_2O[222]
Ethyl Stearate		✓	39	1.98 mPa.s (90ºC)[223]

3.2 Printing Material Characterization

3.2.1 Testing the Solubility of PEG, SA Indurasupport and Induracast moulds.

To streamline the identification of biocompatible build and support materials, a survey of possible materials was done. PEG and SA were obtained as materials with the desired properties: biocompatibility, melting points in the range of 60-70^{o}C and affordability. After a material literature survey, PEG and SA were settled on as the materials within our desired range. PEG and SA were obtained from Sigma Aldrich and an experiment for proof of principle was conducted to ascertain solubility in water and ethanol.

PEG and SA were cast in polydimethylsiloxane (PDMS) moulds and characterized alongside Indurafill and Induracast Fig. 4. Using Fusion 360, computer-aided design (CAD) models of desired moulds were designed. Using a 1.75mm Polylactic Acid (PLA) filament (Tianse), a fused deposition modelling (FDM) 3D printer (Leigh Irving Scientific) was used to print the designed moulds. PDMS was fabricated as per the manufacturer's instructions (184 Silicone Elastomer, Dow Silicone Corporation). The mixture was degassed in a desiccator and cast into the moulds printed using the FDM printer.

The cast was further degassed in the desiccator before being left on a hot plate for 8 hrs at 90^{o}C. PEG, SA and Induracast were melted in a beaker on a hotplate and cast in the PDMS moulds obtained earlier. The moulds were placed in different beakers containing ethanol to dissolve them.

SA and Induracast did dissolve while PEG did not dissolve in ethanol. When the solvent was substituted for deionised (DI) water, PEG dissolved while SA and Induracast did not dissolve in DI water.

Induracast did dissolve while PEG did not dissolve in ethanol. When the solvent was substituted for deionised (DI) water, PEG dissolved while SA and Induracast did not dissolve in DI water. Appendix 1 shows an image that highlights this process.

3.2.2 Testing the Viscosity of PEG, SA, Indurasupport and Induracast.

To determine their suitability as possible replacements for Induracast and Indurasupport, PEG and SA together with Indurasupport and Induracast were subjected to viscosity tests on a Dynamic Mechanical Analyzer (TA Instruments 3200 DMA machine) up to a shear rate of 200 1/s at 100^0C, 110^0C and 115^0C. These temperatures were determined to be the corresponding temperatures providing the required flow rate of PEG and SA in the T612BT's tanks, heated lines and print heads.

3.2.3 Material Characterization of PEG and SA.

Tensile test sample prints of the SA were designed in Fusion 360 and made using the T612BT 3D bioprinter. Control samples were cast using PDMS moulds. The samples were subjected to tensile tests using a dynamic mechanical analyzer (DMA 3200, TA Instruments), comparing the printed and cast samples' mechanical properties.

Thermal properties were determined using a differential scanning calorimeter (DSC250, TA Instruments). Additionally, the printing times on the 3D printer are always varying. PEG and SA will sometimes be left in the printer for days at a time while continuously heating them to maintain a molten state or heating and reheating the materials after starting the printer from a cold boot.

PEG and SA were melted and left in a molten state in an oven for up to 10 days to determine thermal stability and ensure that the material is not changing chemical composition because of the heating practices. These samples underwent Fourier-transform infrared (FTIR) analysis using an FTIR Spectrometer to determine the resulting molecular breakdown due to constant heating. This experiment determined how long PEG and SA can stay in the heated printer's reservoirs while printing. Heated and reheated samples that were 100 days old were also subjected to FTIR analysis.

3.3 Collagen Slurry Formulation

Collagen slurry with concentrations of 0.5%, 1% and 2.5% weight/volume was made by adding the corresponding mass of insoluble Type I Collagen from bovine Achilles tendon powder (Sigma Aldrich Co. Ltd., UK, Cat. # C9879) to 100 ml of 0.05 M acetic acid solution prepared by diluting Acetic Acid (ACS Reagent ≥99.7%, Cat.# 695092, Sigma-Aldrich Co. Ltd., UK) in MilliQ water in a beaker. The suspension was left to rehydrate for 8 hours at 4^{o}C, after which this dispersion was homogenized using a blender for 4 minutes on ice, then transferred to 50ml conical tubes.

The tubes were centrifuged at 4°C and 2500 RPM to remove air bubbles. This slurry was stored in a refrigerator at 4°C awaiting use.

3.3.1 Material Characterization of Collagen Slurry

The rheological properties of the collagen slurry used to fabricate scaffolds affects the quality of scaffolds obtained[200]. For instance, slurries with a high viscosity tend to have smaller pore sizes than slurries with lower viscosity[13]. Since collagen will be cast in the moulds, a low viscosity may lower the ability of collagen to flow into small-sized features of the mould[142].

Using a Dynamic Mechanical Analyzer (DMA 3200, TA Instruments), the rheological properties of the collagen slurry were determined. The different collagen slurry concentrations were tested twice in independent experiments.

To characterize the effect of collagen concentration and freezing temperature on pore size and geometry of the obtained scaffolds, samples were prepared by casting collagen in SA moulds. These were frozen in -20°C, -80°C and -196°C. The obtained samples were then broken to reveal the internal cross-section. These samples were freeze-dried to remove the ice crystals, and the obtained samples were imaged using a scanning electron microscope (SEM). ImageJ (National Institutes of Health) was used to analyze the SEM micrographs.

3.4 Fabrication of Collagen scaffolds

An inverse mold (Fig 3.4), with predefined channels was designed using CAD software (Autodesk Fusion 360). The CAD designs were saved as standard triangle language (STL) files and transferred into ModelWorks (Stratasys Inc.) for slicing. The sliced files saved as .t12 are transferred to the phase change jet bioprinter (Solidscape T612BT, Stratasys Inc.) discussed above. Before printing the mould, the printer prints two layers of PEG. SA will then print the inverse mould.

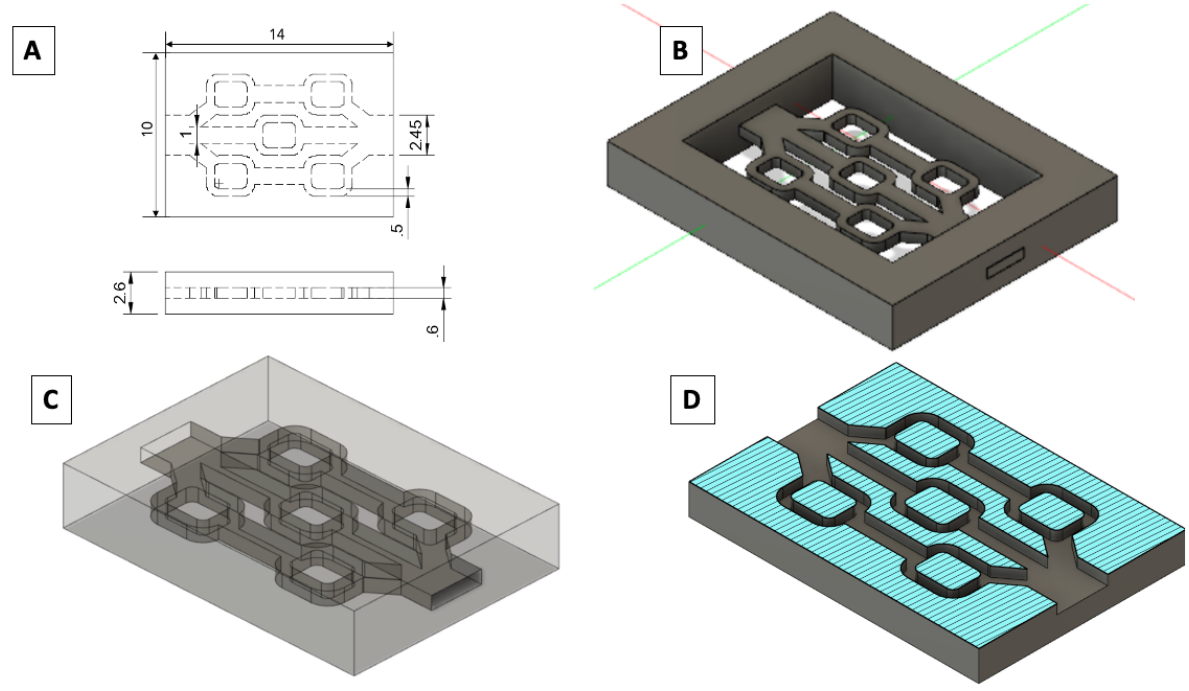

Figure 3.3: CAD designs of the stearic acid mould as well as the collagen scaffolds, designed using Autodesk Fusion 360 (**A**) is the CAD drawing of the scaffold showing the channel measurement. (**B**) is an image showing the internal microarchitecture. (**C**) is the CAD design of the mould, while (**D**) shows a cross-section of the scaffolds to reveal the internal microarchitecture. All measurements in mm.

Printed overhangs generated by SA and other spaces are held in place by the PEG support print material. Once printing is completed, the print bed is transferred to a hot plate and slightly heated to 40^{o}C. This softens the two layers of PEG and aid in the easy removal of the printed moulds. The moulds were placed in a conical flask containing water and in an orbital shaker maintained at 30^{0}C and 180 rpm. This action dissolved away the support material PEG. The obtained stearic acid moulds were air dried and stored in an airtight container awaiting further use.

One of the printed and washed stearic acid moulds was selected, and Collagen slurry cast into the mould. The cast mould was frozen at a temperature of -20^{o}C in a freezer. This freezes the collagen slurry's water component, creating ice crystals that fill the interstitial space. The frozen cast is then immersed in ethanol which dissolves away the stearic acid as well as the ice crystals in the collagen. A foam structure made up of interconnected pores within the scaffold is obtained. In future experiments, CAD designs containing channels of different sizes will be made to determine the optimum channel size for cell support.

3.5 Crosslinking of the Collagen Scaffolds

An EDC-NHS crosslinking solution of 1-ethyl-3-(3-dimethylaminopropyl) carbodiimide hydrochloride (EDC, Cat.# 161462, Sigma-Aldrich Co. Ltd., UK) and N-hydroxy-succinimide (NHS, Cat.# 6066-82-6, Sigma-Aldrich Co. Ltd., UK) was prepared using a 5:2:1 M ratio for EDC: NHS: Collagen, hereafter referred to as the ‘100% concentration’.

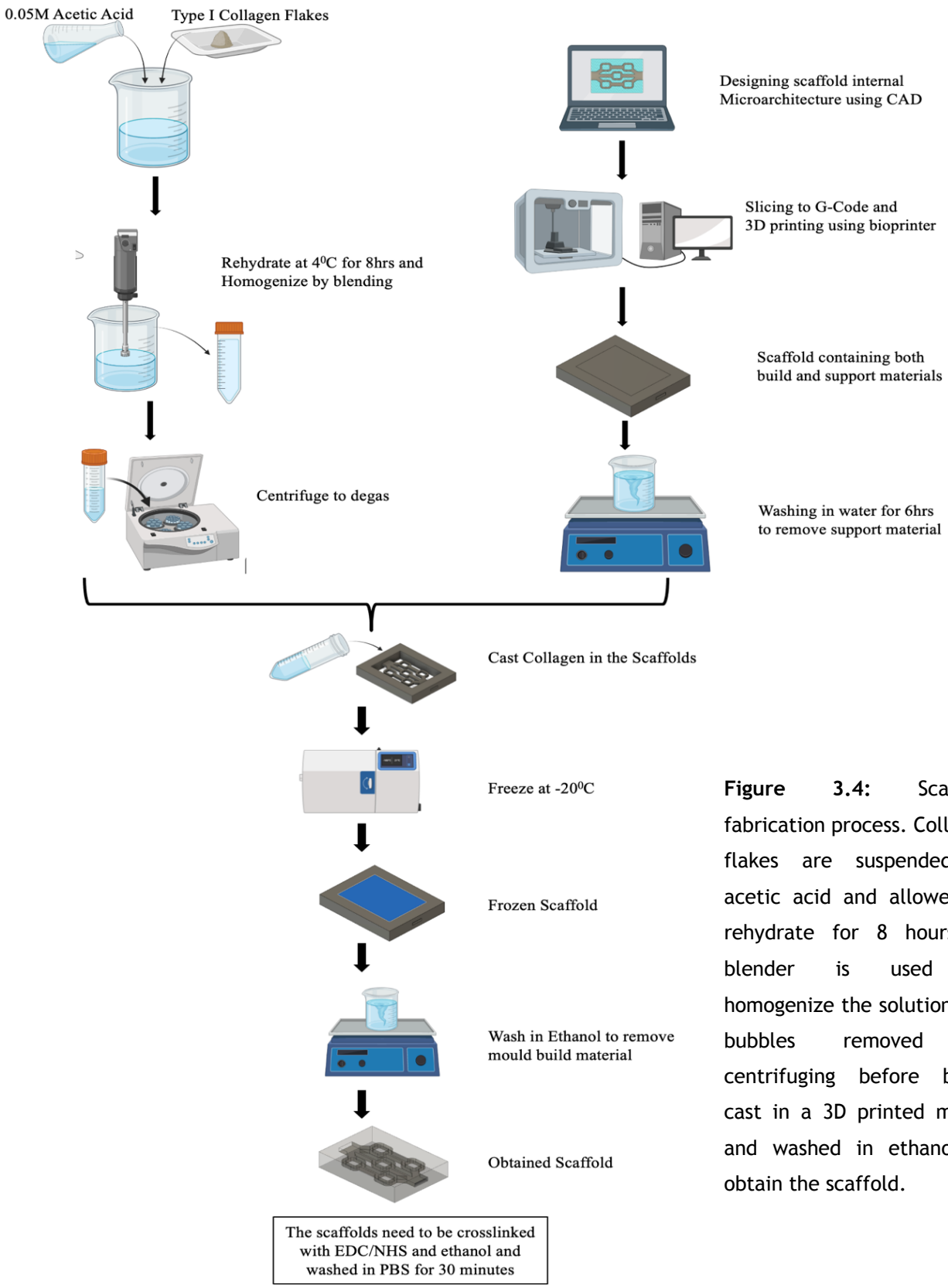

Figure 3.4: Scaffold fabrication process. Collagen flakes are suspended in acetic acid and allowed to rehydrate for 8 hours. A blender is used to homogenize the solution and bubbles removed by centrifuging before being cast in a 3D printed mould and washed in ethanol to obtain the scaffold.

For every 1 mg of collagen, the 100% concentration standard of crosslinking solution consisted of 1.15 mg EDC and 0.276 mg NHS dissolved in 80% ethanol. Scaffolds were immersed in the crosslinking solution and allowed to react for 3 hours at room temperature on an orbital shaker at 180rpm. After the reaction the scaffolds were washed thoroughly in Phosphate Buffer Solution (Dulbecco's phosphate buffered saline (PBS) powder (Cat. # D5652, Sigma-Aldrich Co. Ltd., UK) diluted in MilliQ water and sterilized) three times for 30 minutes. Scaffolds were then stored in PBS solution awaiting further use.

3.6 Collagen Scaffold Mechanical Characterization.

The scaffolds were freeze-dried as a suitable rig to conduct hydrated tensile scaffolds was not obtained. The dry scaffolds were subjected to tensile testing using a Dynamic Mechanical Analyzer (DMA 3200, TA instruments). An average of 4 runs for each experiment was conducted to determine Young's Modulus. Results were obtained to compare the correlation between Young's Moduli of the scaffolds to their pore size as well as the collagen slurry w/v concentration.

Shrinkage was measured using digital callipers. The results were used to observe the correlation between the time taken in the different fabrication procedures and their effect on the shrinkage of the collagen scaffolds.

Bonds in the chemical structure of collagen when observed in FTIR spectrometer will absorb light of particular wavelengths. A change in these absorption spectra signifies a change in the chemical composition of collagen.

Denaturation of collagen results in a change in its chemical structure. FTIR analysis was used to observe the denaturation of collagen because of the procedures carried out on the collagen.

3.7 Visualization of the Collagen Scaffold Internal Microarchitecture

Optical coherence tomography (OCT) was used to obtain images of the internal microarchitecture of the scaffolds. OCT is based on principles similar to low coherence interferometry, whereby electromagnetic waves directed from a light source to the tissue under study are echoed off from the tissue's microstructure, similar to the method used by an ultrasound[224].

The delay of the backscattered waves is measured and the depth at which the reflections occurred is thus revealed. Since light travels fast, direct measurement of these reflected waves is impossible; therefore, an interferometer with a reference light beam is used in this measurement[224].

A spectral domain OCT setup was used to image our scaffolds as shown in Fig. 3.6. An infrared super luminescent diode (Exalos; Switzerland) with a central wavelength(λ_0) of 1315 nm and bandwidth of 115 nm at 3dB and with a maximal output power of 30 mW was used as a light source. This light travelled through an optical circulator to a 2 X 2 fiber coupler with a 50/50 splitting ratio. This light was redirected to the sample arm and a reference arm.

By matching the polarization of the sample and reference, a polarization controller (Thorlabs) was used to reduce sample reflections and increase the signal-to-noise ratio. This output was redirected to the sample and the reference arms. The diverging optical fiber beams were collimated using collimators (Thorlabs).

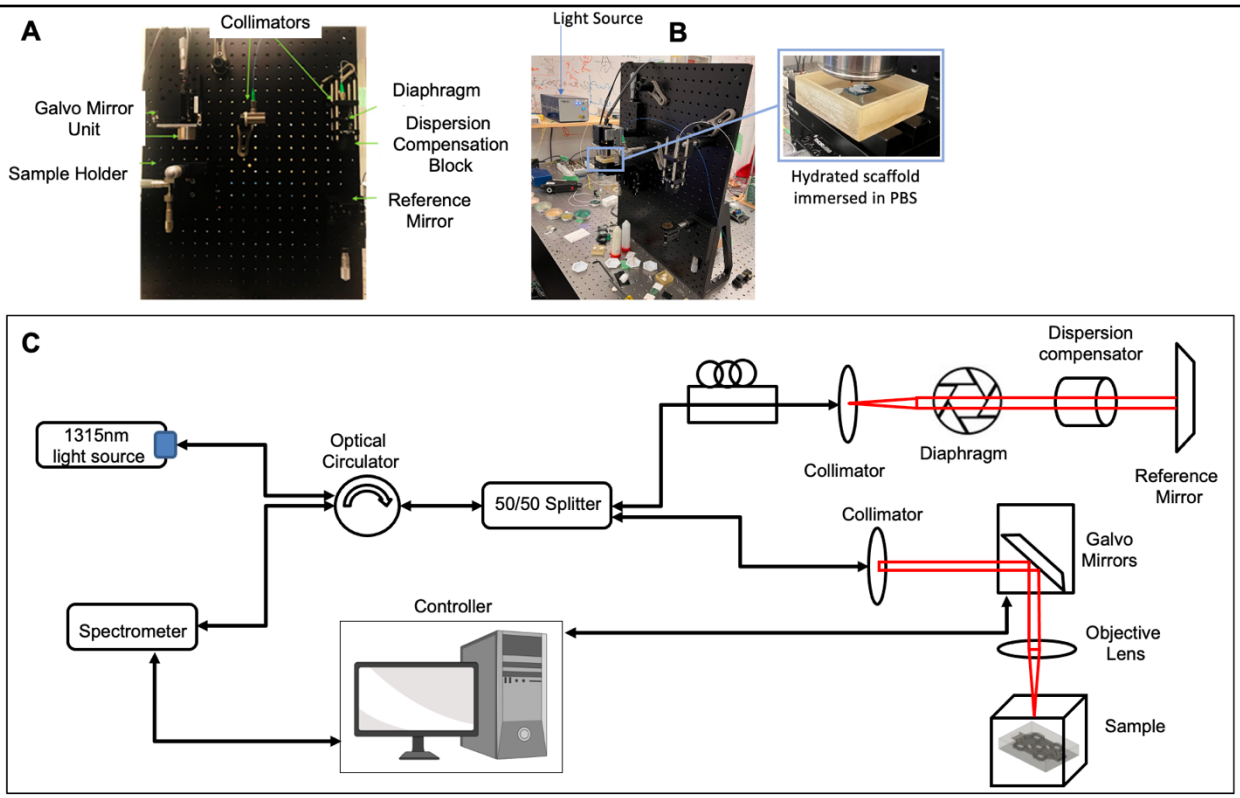

Figure 3.5: OCT setup used to obtain images of scaffold cross sections. (**A**) and (**B**) show the actual setup while (**C**) is a schematic showing the arrangement of components used in the OCT setup. Light of a wavelength of 1315nm is sent from a light source and reflected from a reference mirror and the sample. A computer program processes this spectral data to reveal cross sections of the scaffold sample. This process is done without inflicting damage on the scaffold.

Raster scanning by two galvo scanner mirrors was used to generate volumetric images. To enable the acquisition and signal processing of spectrometer data on a computer, a custom program developed in the LabVIEW environment (National Instruments) was used. This software was used to display images of the cross-sections of the sample.

Chapter 4: Results and Discussion

4.1 Comparing PEG and SA Printability to Induracast and Indurasupport.

Following solubility tests that confirmed PEG dissolving in water and SA dissolving in ethanol, it is important that these compounds can flow in the heated lines at rates comparable to those of the native Induracast and Indurasupport.

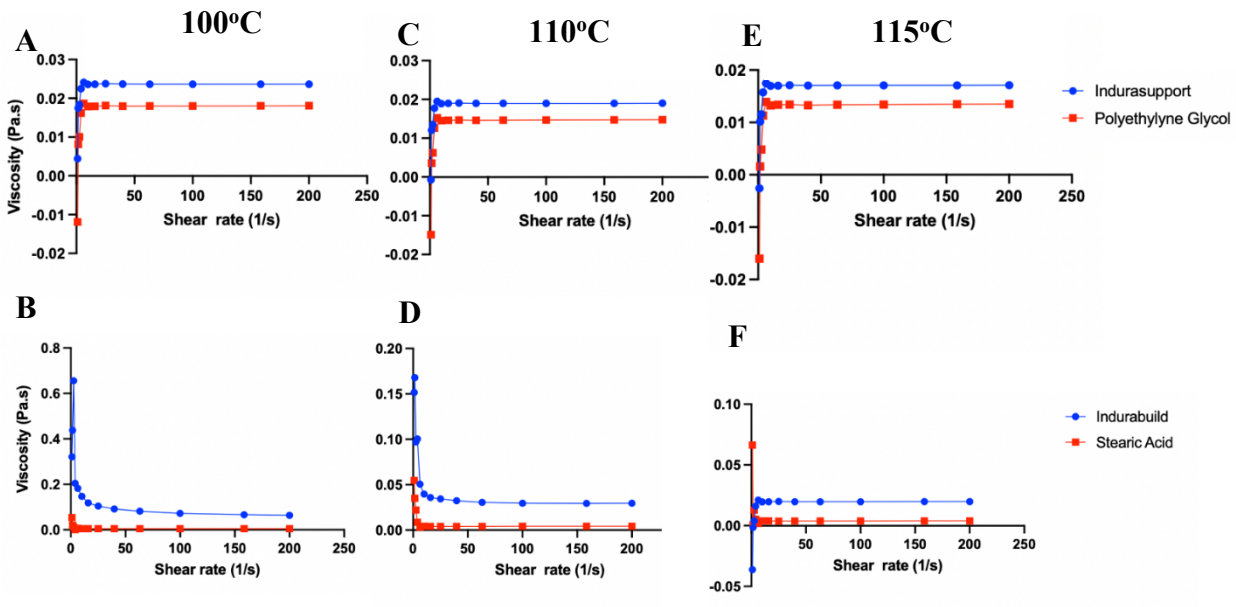

Figure 4.1: Comparing the viscosities of (**A**) Indurasupport to PEG and (**B**) Induracast to SA at100°C, (**C**) and (**D**) compares viscosities at 110°C and (**E**) and (**F**) compares viscosities at 115°C Indurabuild to SA at 100°C, 110°C and 115°C. As the temperatures increased above 110°C, the viscosities tended to have a smaller difference than 100°C. There is a comparable shift in viscosities of PEG and Indurasupport to less than 0.005 Pa.s and less than 0.0025 for SA and Induracast for corresponding temperatures at temperatures between 110 and 115°C.

The viscosity of PEG and SA was compared against that of Induracast and Indurasupport. Using a Dynamic Mechanical Analyzer, results from viscosity tests as seen in **Figure 4.1** suggest that PEG and SA can be used to replace induracast and indurasupport as the printing material as they flow at comparable rates that are within 2 mPa.s and 7.5 mPa.s respectively for PEG and SA in comparison to Indurasupport and Induracast at temperatures between 110^{o}C and 115^{o}C. Ultimately, PEG was printed at 110^{o}C as the support material while SA was printed at 115^{o}C as the build material on the 3D printer.

4.2 Observation of Printing Material Degradation.

It is important that PEG and SA retain their chemical composition after being 3D printed. This is because further processing of the moulds depend on the specific chemical compositions of PEG and SA. Degradation would be observed by a change in the chemical composition of the mould materials.

This material was not meant to be discarded. The next time the printer is used, the material undergoes a second heating cycle. Subsequent heating cycles were named the third, the fourth, the fifth and so on. Material needed to be checked for degradation due to multiple heating cycles. Additionally, these materials would be left in the printer for several days at a time, sometimes without printing.

FTIR spectrometry was used to observe whether there was the degradation of stearic acid and polyethylene glycol because of heating during the 3D printing action. The results of these observations are highlighted in **Figure 4.2.** An attenuated total reflection (ATR) FTIR spectrometer was used in this experiment. A sample was placed on a diamond crystal on the instrument.

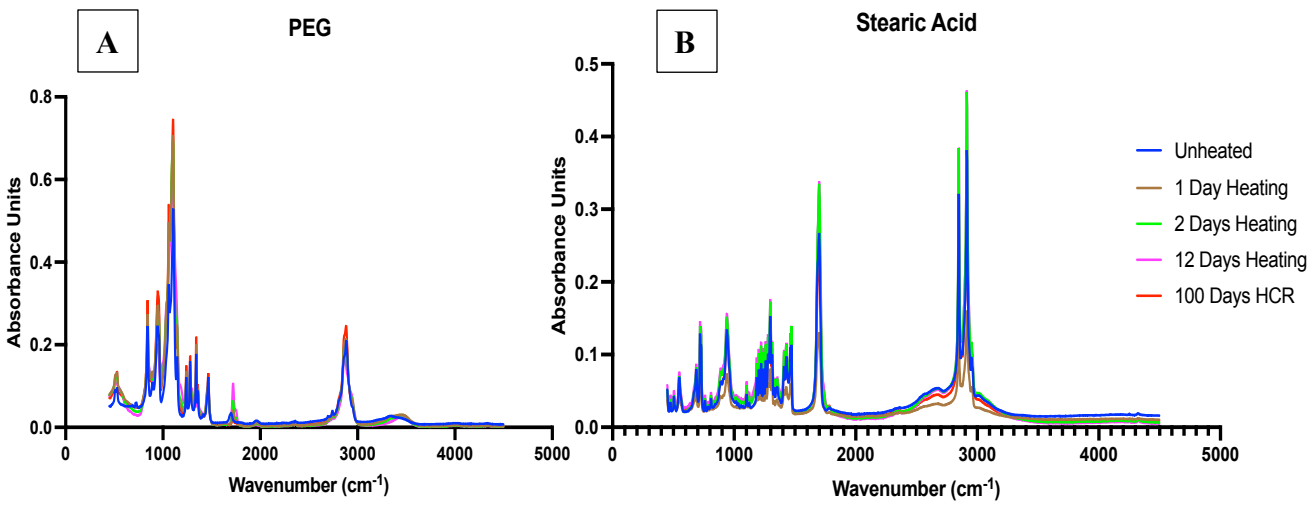

Figure 4.2: FTIR spectra of (**A**) PEG and (**B**) SA to examine degradation due to heating. Samples were heated for up to 12 days in an oven maintained at 100ºC. An additional sample was obtained from the 3D printer. This sample had been in the printer for 100 days, heated, cooled and reheated to 100ºC in multiple cycles. An unheated sample is used for reference. Peaks on the test samples that have been heated over several days correspond to wavenumbers on the unheated sample referred to as REF. 0 DAYS, showing no degradation on both PEG and SA due to heating.

Infrared light was passed through the diamond crystal and interacted with the sample while part of that light would undergo total internal reflection. Analysis of how much light was reflected by analysis software (OPUS) provides molecular information about the sample.

In this experiment, samples were heated in an oven at 100°C for 12 days, and an additional sample was obtained from each of the printer's tanks after 100 days of heating, cooling and reheating the tanks to 100^0C. The obtained spectra showed that the chemical composition of PEG and SA did not change after heating as all the corresponding samples of SA and PEG matched the unheated samples.

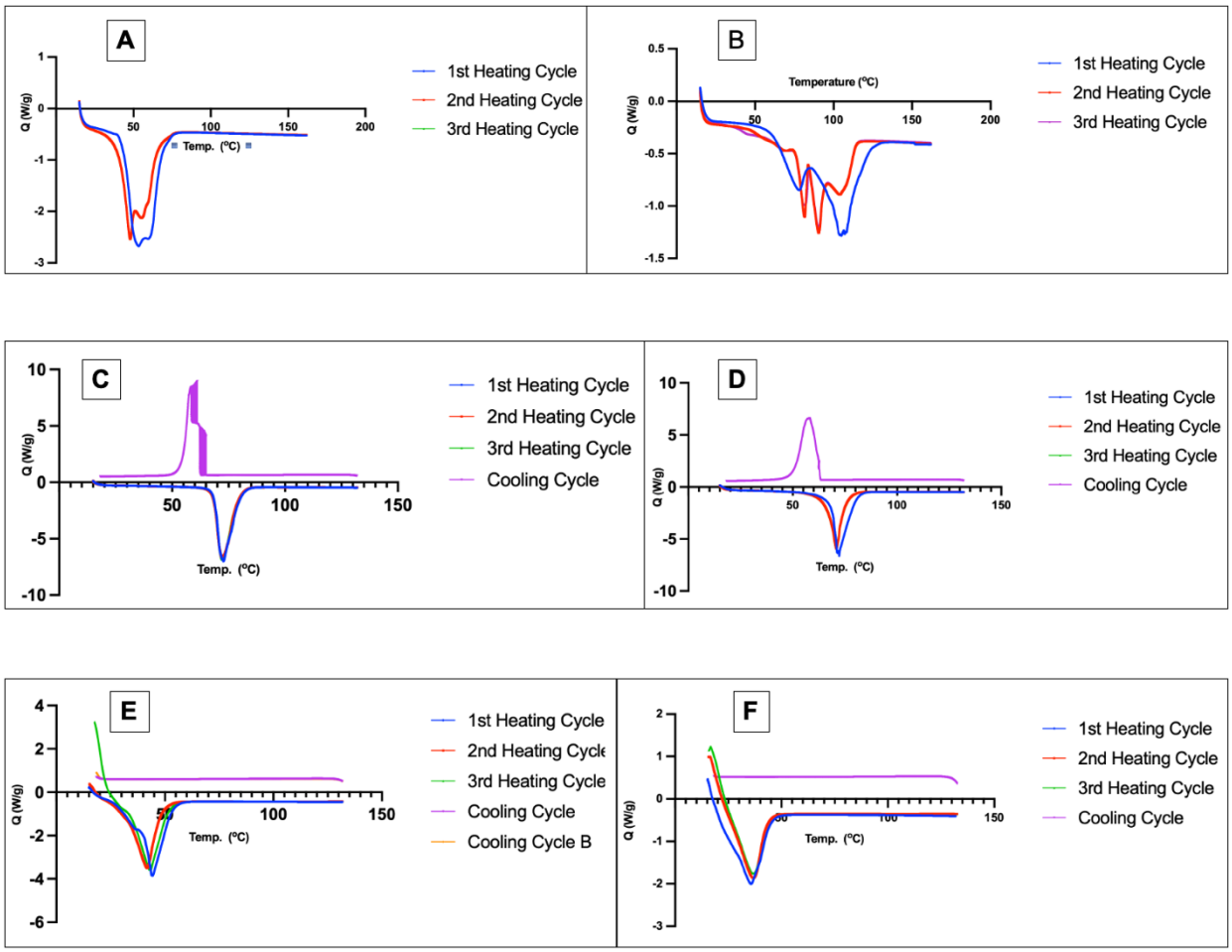

Figure 4.3: An examination was done to determine the thermal properties of the printing materials. These experiments also provided proof that the chemical properties of PEG and stearic acid did not change with subsequent heating cycles.

When virgin PEG and SA are placed in the heated tanks, the materials are heated and transported along the heated lines to the print head to commence the printing action. We called this the first heating cycle. After the printing action of the 3D bioprinter, unused PEG and SA would be left over in the tanks, heated lines and the print heads. This material should not degrade due to this heating mechanism. **Fig. 4.3** shows heating and cooling profiles simulated according to conditions during normal printing of moulds on the 3D printer. An analysis of these heating and cooling profiles shows that the material does not deviate from the heating cycles that are experienced by the virgin printing material.

4.3. Printing Temperature Determination – Print Droplet Analysis.

As observed in the viscosity analysis tests in Section 4.1 and Figure 4.1 above, print material viscosity depended on the material temperature. Printing at different results yielded moulds with a few deformities. This included the effects of double jetting and failure of material jetting from time to time. The double jetting resulted from two factors: jet wetting – the accumulation of print material on the print jets leading to failure of proper material deposition; and partial jet blocking due to blockage of the jet by a lodged foreign material. It was observed that jet wetting was most experienced when printing at temperatures below 110^0C and occasionally at temperatures above 110^0C. Images of characteristic double jetting and jet wetting can be seen in Appendix 2. A print droplet analysis was conducted by quickly passing glass slides under material as it was jetted from the print heads. These glass slides were observed under a light microscope (Imager M2 – Zeiss), and images were collected using a camera (Axio-Zeiss).

These results are shown in Fig. 4.5. Print bead diameters were collected at different temperatures and compared against those of induracast whose recommended print temperature was 115^0C

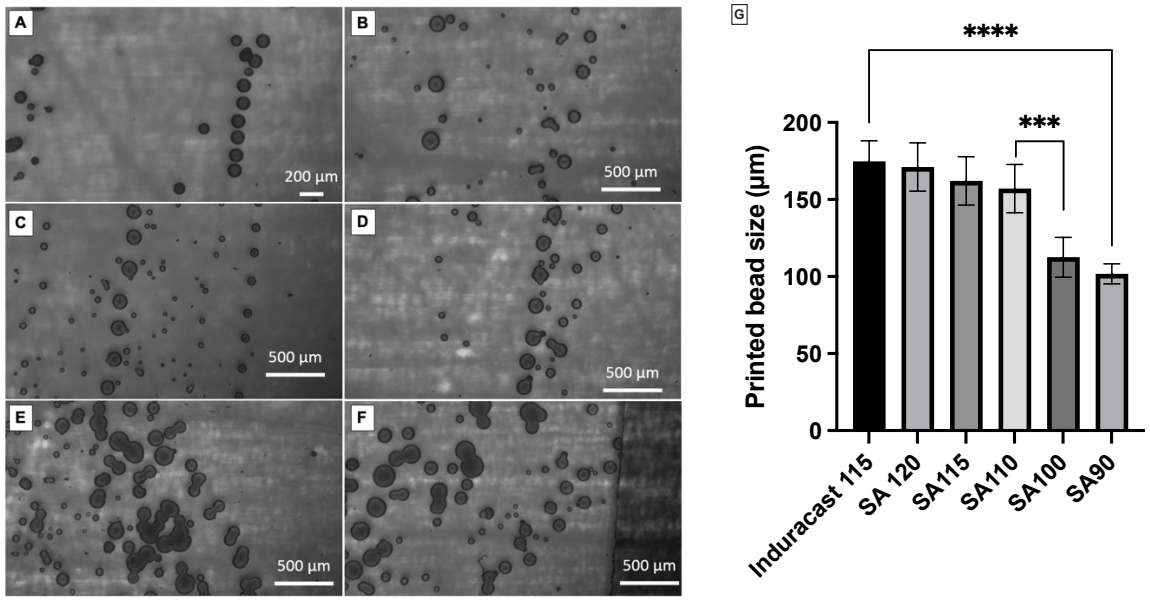

Figure 4.4: Comparing bead diameters of SA and Induracast. Images of stearic acid beads collected at different print temperatures (**A**)-90ºC, (**B**)-100ºC, (**C**)-110ºC, (**D**)-115ºC and (**E**)-120ºC alongside (**F**)-induracast beads collected at 115ºC. (**G**) shows a graph comparing the means of different bead sizes for the two materials. Printing of stearic acid at 120ºC produced bead sizes consistently comparable to those obtained by printing induracast at the recommended 115ºC. Images processed with ImageJ and data analyzed in Graphpad Prism. Data reported as mean ± SD. (***)p<0.001, (****)p<0.0001, n=6.

An analysis of these beads using ImageJ was conducted comparing the means of the bead diameters. Stearic acid beads printed at 120^0C had diameters comparable to induracast beads. It was decided that the printer would print stearic acid at 120^0C. A similar test was conducted comparing PEG to indurasupport beads and for optimum printing results, PEG was printed at 105-110^0C.

This variation was because of the hygroscopic nature of PEG that led to the yielding of different diameters on contact with the glass slides. The wetting of the PEG jet was not observed to be dependent on temperature as opposed to that of stearic acid.

4.4 The Effect of Scaffold Preparation and Casting Conditions

After the moulds are prepared, Collagen slurry is cast and frozen to push the water component into the interstitial spaces. Dissolution of this water in ethanol on further processing will create interconnected pores in the collagen scaffold. These pores need to be of an optimum size to allow for the proliferation of the scaffold with cells upon seeding.

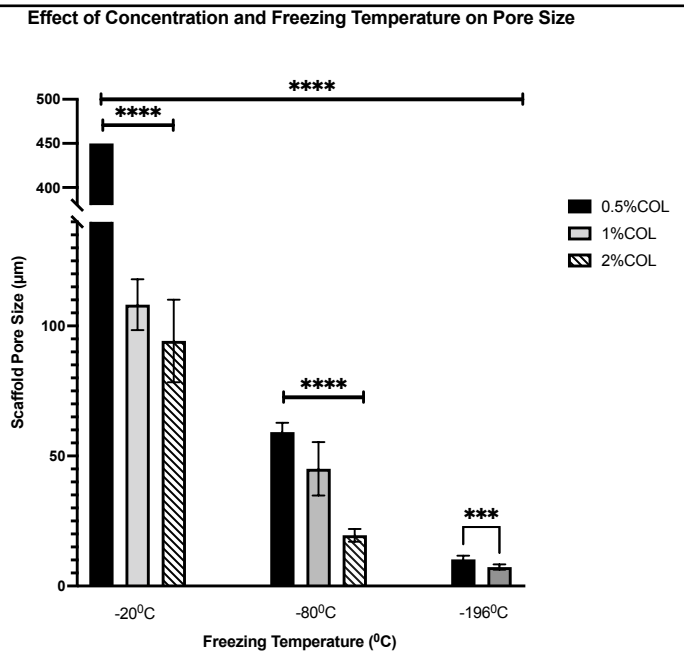

Figure 4.5: Bar graphs comparing the means of pore diameters of different collagen scaffolds fabricated from different collagen concentrations and freezing temperatures. Analysis of the pore diameters from SEM images shows that lower freezing temperatures yielded scaffolds with smaller pore sizes. At the same time, higher collagen concentrations also yielded smaller pore sizes. The images were processed in ImageJ and analyzed in Graphpad. Data reported as mean ± SD. (***)$p<0.001$, (****)$p<0.0001$, n=14.

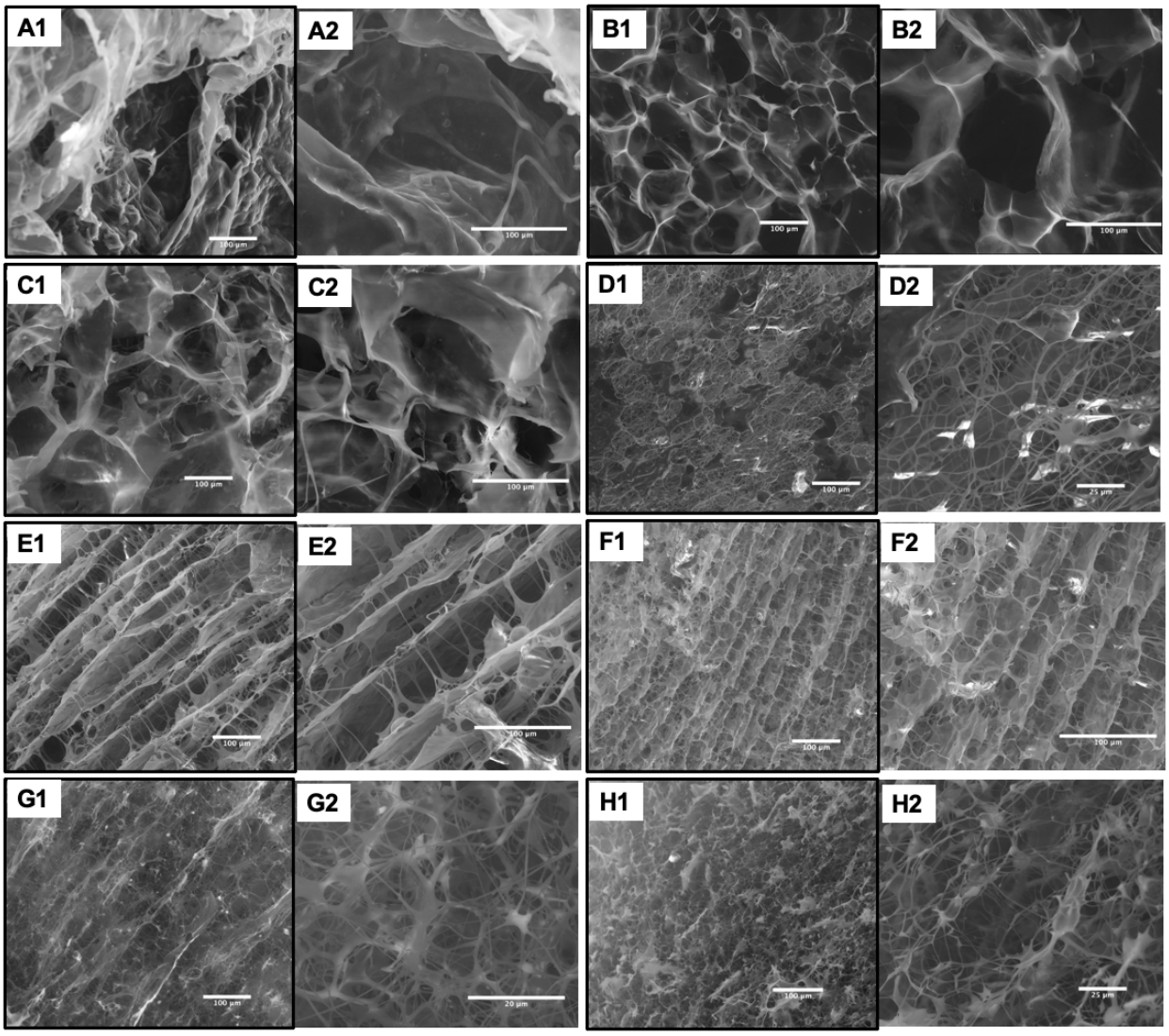

Figure 4.6: SEM images of different collagen scaffolds made with different collagen concentrations and freezing temperatures. **(A1, B1, …)** show SEM micrographs obtained at x250 magnification while **(A2, B2, …)** show SEM micrographs obtained at x500-2500 magnification to reveal the architecture of the pores in the scaffold. The scaffolds have been fabricated by freezing at different temperatures. (**A-C):** -20^{0}C, **(D-F)**: -80^{0}C, **(G-H)**: -196^{0}C. **(A),(D)** and **(G)** have a collagen concentration of 0.5%, **(B),(E)** and **(H)** have a collagen concentration of 1% while **(C)** and **(F)** have a concentration of 2%. SEM Images were taken by (Quanta 3D, Thermofisher, USA) The images were processed in ImageJ and analyzed in Graphpad. Analysis of the pore diameters from SEM images in ImageJ show that lower freezing temperatures yielded scaffolds with smaller pore sizes. At the same time, higher collagen concentrations also yielded smaller pore sizes.

Different cells have different preference for different pore sizes. By understanding the effect of collagen concentration and the freezing temperature, scaffolds will be fabricated with the necessary conditions according to the cells we desire to use for subsequent tissue engineering exercises.

The images were collected by a scanning electron microscope (Quanta 3D, Thermofisher, USA) and processed using ImageJ. Analysis of the obtained pore sizes by Graphpad showed that lower freezing temperatures led to obtaining smaller pore sizes as shown in **Fig. 6** and **Fig. 4.7.** Lower freezing temperatures also had clear orientations of pores aligned parallel to one another. This is because of the rapid freezing of water and ice crystals forming in one direction as opposed to higher (less negative) freezing temperatures where ice crystals are formed slower. Higher collagen concentrations in the slurry led to the creation of smaller pores than lower collagen concentrations in the slurry.

4.5. Wash time optimization

Once printed, the moulds are washed in water to remove PEG, the support material. The moulds must spend enough time in water so that the resulting SA mould is not contaminated with any PEG. Remaining Trace amounts of PEG in the SA mould will occupy space that should otherwise be occupied by collagen once the slurry is cast in the SA mould.

To determine optimum wash time 4 samples of 4 different designs were evaluated by weighing them on a weigh scale and plotting their weight against the amount of time they had spent in water. Care was taken to dry the mould prior to weighing as any trace amounts of water would significantly alter the wight of the washed mould. These results have been highlighted in Fig. 4.8. The 4 designs had different amounts of PEG support embedded in their surface area presented as a percentage of their total exposed surface area according to the complexity of the design. It was observed that the most complex designs covered in more PEG took more time to wash. The least amount of time to wash the scaffold was 6 hours for scaffolds with at least 40% support material cover. However, it is recommended that the moulds be washed overnight in an orbital shaker for a minimum of 10 hours. This will ensure that any trace amounts of PEG are completely washed.

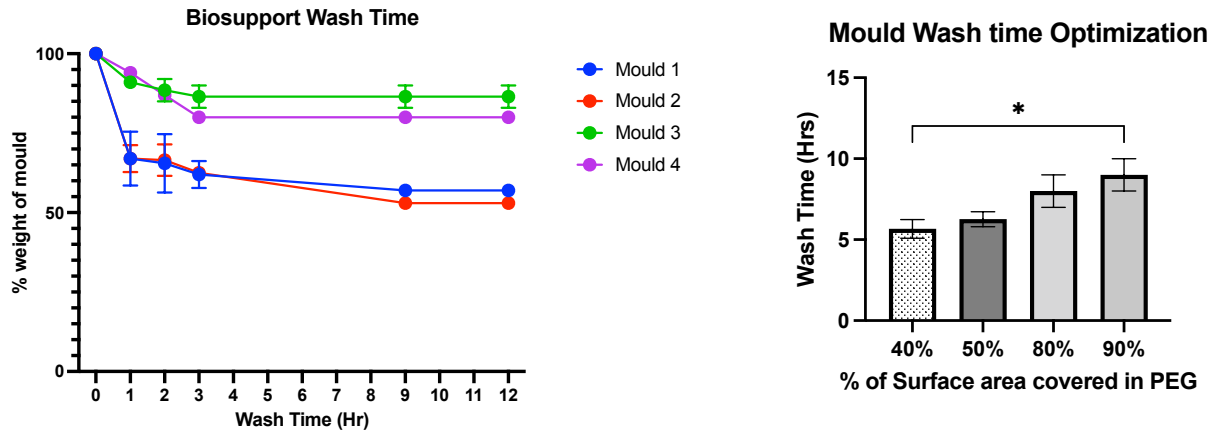

Figure 4.7: Determining Mould Wash Time. These plots analyze the amount of time taken to wash moulds in water to remove PEG. It is recommended that scaffolds be washed overnight as it may not be necessarily forthcoming as to how much support material is covering a mould. Analysis performed on Graphpad Prism. Data reported as mean ± SD. (*)$p<0.05$, n=4.

4.6 Observation of Channels and Channel Characterization

To observe the internal structure and microarchitecture of the scaffolds, the viability of four methods was assessed: Use of a light microscope, microtomography (using a Bruker Skyscan 1210 x-ray micro-tomography (μCT) system), use of an optical coherence tomography (OCT) setup and an environmental scanning electron micrograph (ESEM) (Quanta 3D, Thermofisher, USA).

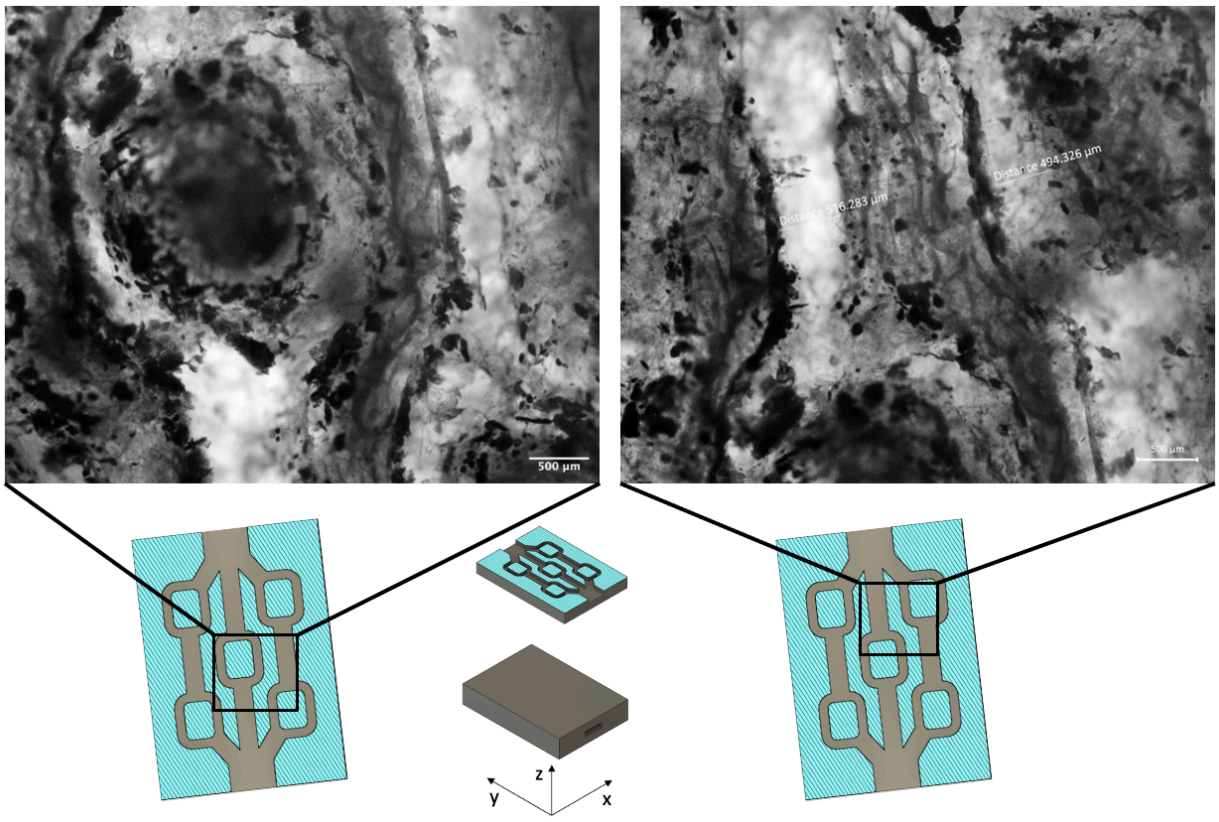

Figure 4.8: Micrographs of the scaffold obtained using a light microscope. While this method reveals the internal channels, a transverse section was made through the scaffold in the x-y plane. This rendered the scaffold unusable as this method destroyed the integrity of the enclosed channels. OCT follows this proof of concept in **Fig. 4.9,** which shows the presence of channels in the scaffold non-destructively.

Of these four setups, OCT was considered the most viable one and offered the advantage of non-destructiveness to the specimen. μCT needed a dopant to be added to the specimen. This would make the specimen cytotoxic. Suggested dopants were Cesium Chloride and Potassium Iodide. A doping method is still under experimentation to ensure the visibility of the scanned internal microarchitecture of the scaffold.

ESEM operates in a vacuum. This led to specimen drying and collapse; therefore, the internal microarchitecture could not be observed using ESEM. The alternative is to use SEM and slice through the midplane of a freeze-dried scaffold which is destructive and renders the scaffold unusable after imaging.

The internal microarchitecture of the Scaffolds was examined using a light microscope (Imager.M2, Zeiss). Obtained images can be seen in Fig. 4.9. While it was possible to observe the internal architecture, the scaffold had to be sliced open. This destruction of the scaffold renders it unusable. Images obtained from OCT however, Fig. 4.10, were obtained without destroying the scaffold. On further analysis of the scaffold OCT images by processing the images using ImageJ tools to measure the scaffold shrinkage, it was observed that all scaffolds experienced shrinkage compared to the CAD design file.

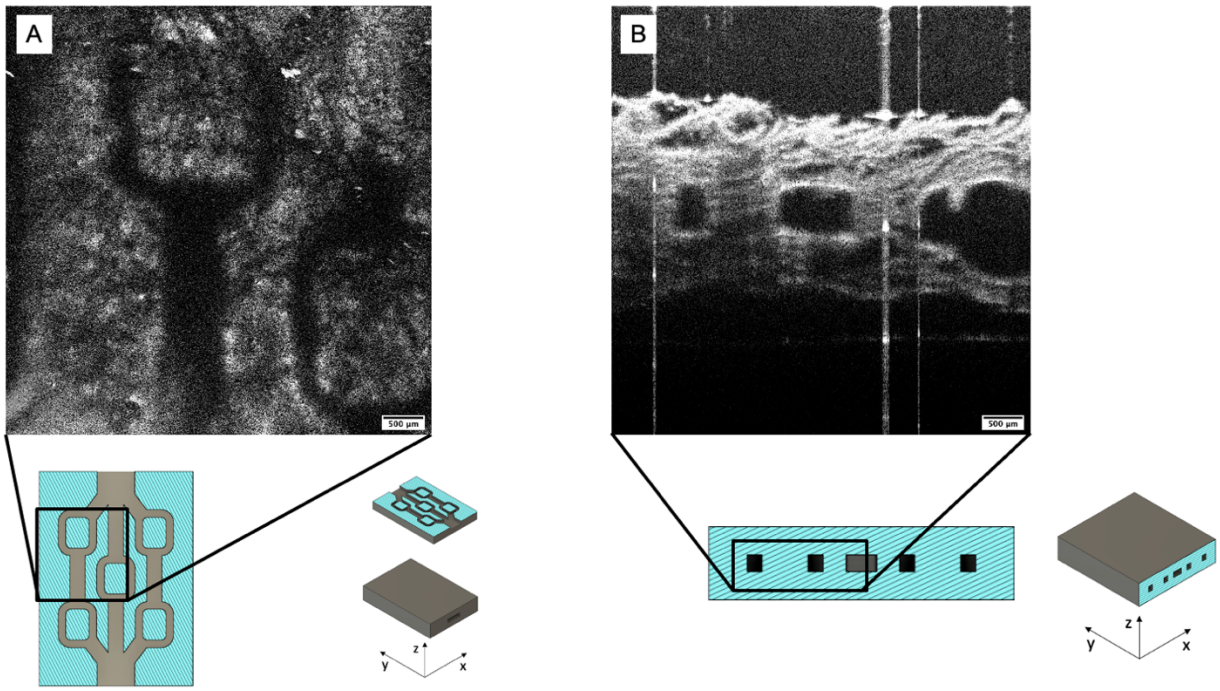

Figure 4.9: OCT images revealing the internal microarchitecture of the collagen scaffolds. A. Shows a transverse section showing a cross-section of the channels along the x-y plane. B shows an image of a cross-section of the scaffolds along the x-z plane. The scaffolds are suspended in PBS during the test and are not destroyed. Multiple images taken by OCT can be manipulated by additional software and stitched together to create a full stack of 3D image files.

As seen in **Figure 4.10**, an analysis of the channel width and height illustrated a shrinkage with a slight recovery in narrower channels and a significant recovery in the channel height when the NHS-EDC crosslinker is added without washing in PBS. Narrower channels, Channel 2, shrunk more than the wider channels, channel 1 by about 40%. Washing in PBS after crosslinking led to further shrinkage with the second PBS wash leading to a 1% recovery in channel width and a 5% recovery in channel height.

$$Scaffold\ Shrinkage = \frac{D-R}{D}\ X\ 100\% \qquad \text{Eq. 4.1}$$

D = Design Scaffold Dimension

R = Measured Scaffold Dimension

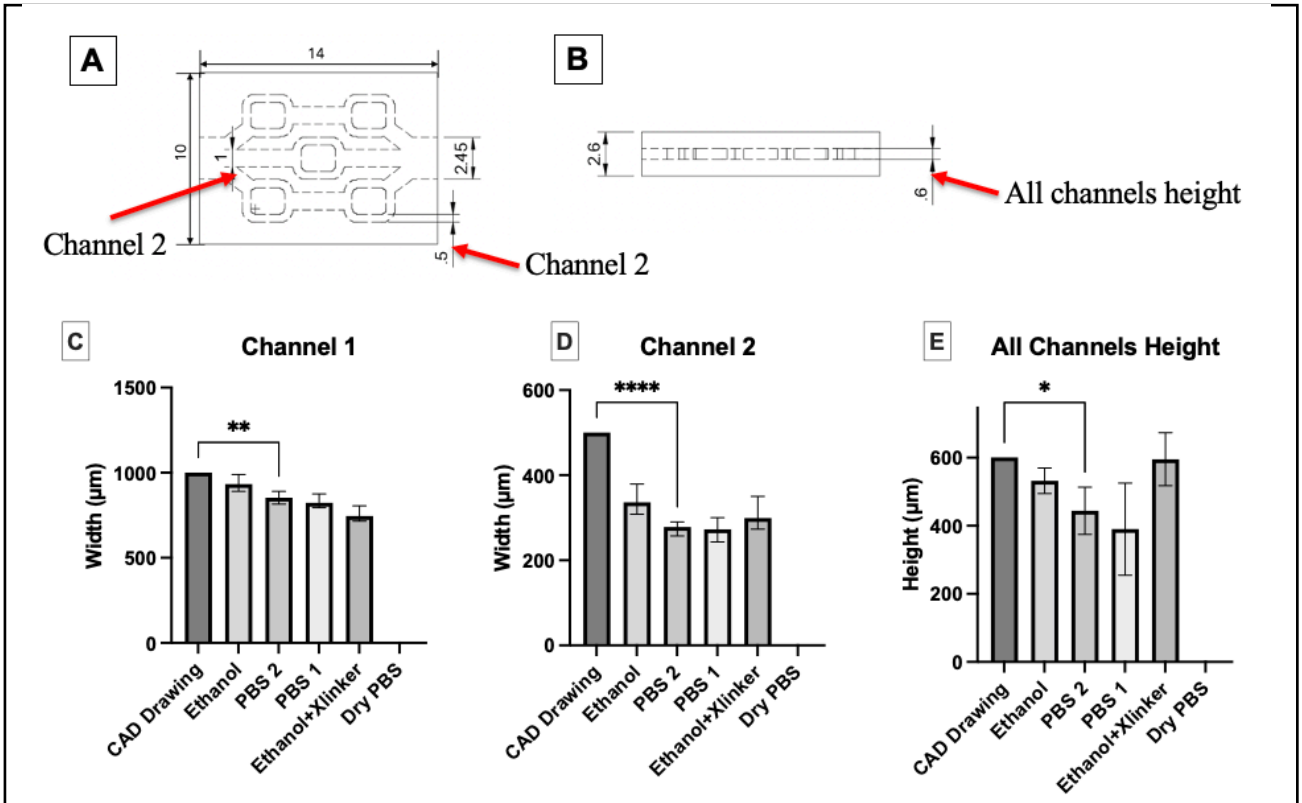

Figure 4.10: An analysis of channel shrinkage. Analysis of the designed channel sizes highlighted in the red arrows on CAD design compared to channel 1, channel 2 and the channel height. Washing the mould and the scaffold in ethanol shrunk the channels. Subsequent crosslinking shrunk the channels further while washing in PBS after crosslinking led to further shrinkage with a second wash in PBS leading to slight shrinkage recovery. Data collected from OCT instrument and image processed in ImageJ. Data analysed in Graphpad. Data reported as mean ± SD. (*) $p<0.05$, (**)$p<0.01$, (****)$p<0.0001$, n=6.

4.7 Mechanical Characterization of Moulds and Scaffolds

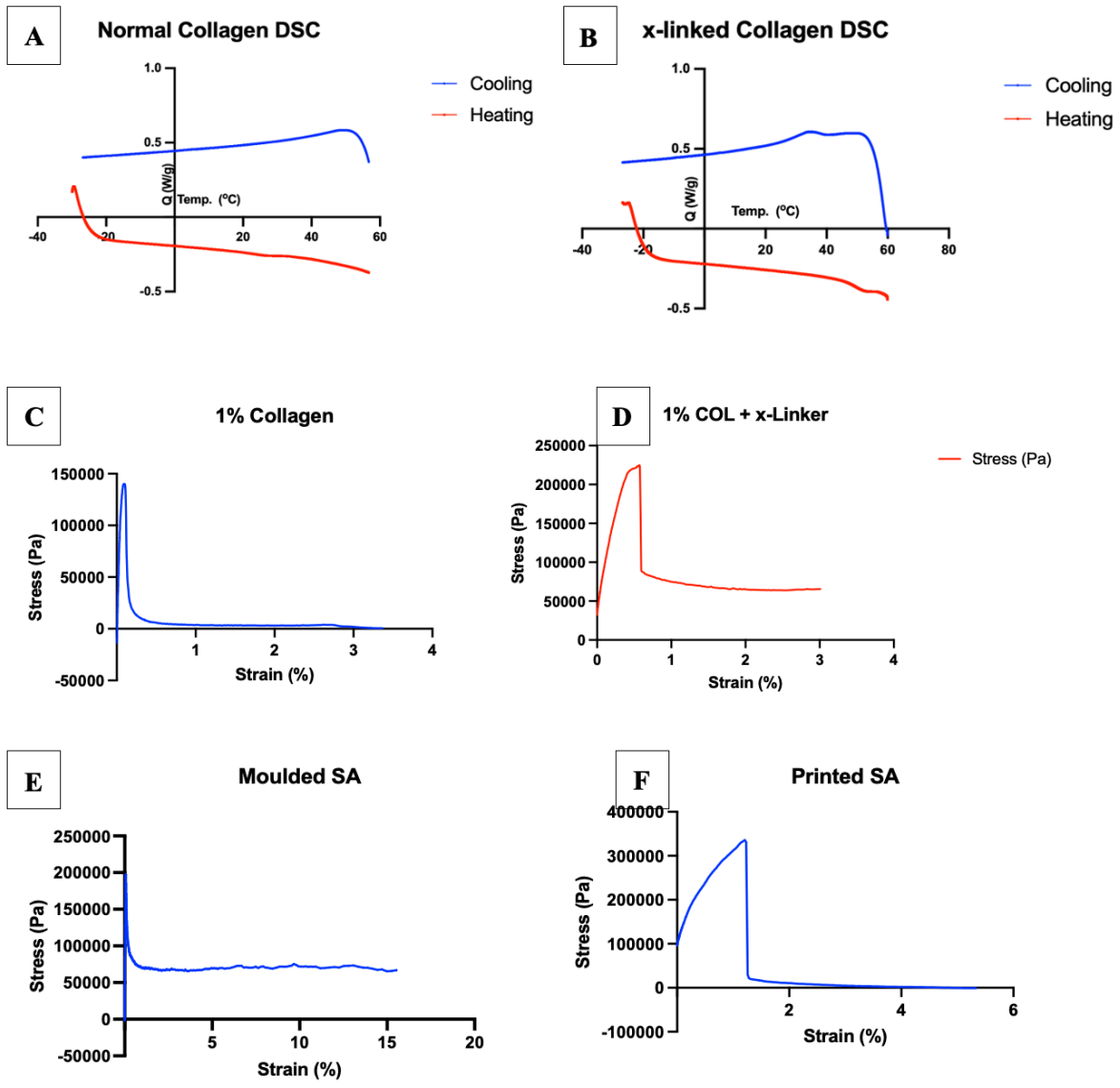

Figure 4.11: Thermal Profiles for Uncrosslinked and Crosslinked Collagen Scaffolds. (A) and **(B)** Show thermal profile curves for normal collagen and crosslinked collagen. **(C)** Uncrosslinked collagen shows a very steep elastic region on the stress vs strain curve compared to **(D)** crosslinked collagen with a lower young's modulus suggesting a stronger material. Crosslinking increases the mechanical strength of the collagen scaffold. **(E)** When SA is cast in PDMS, it yields a very brittle specimen as opposed to **(F)** printed specimens of SA that show a stronger material. Data were obtained from a DMA Machine (TA 3200 DMA Machine, TA Instruments), n=4.

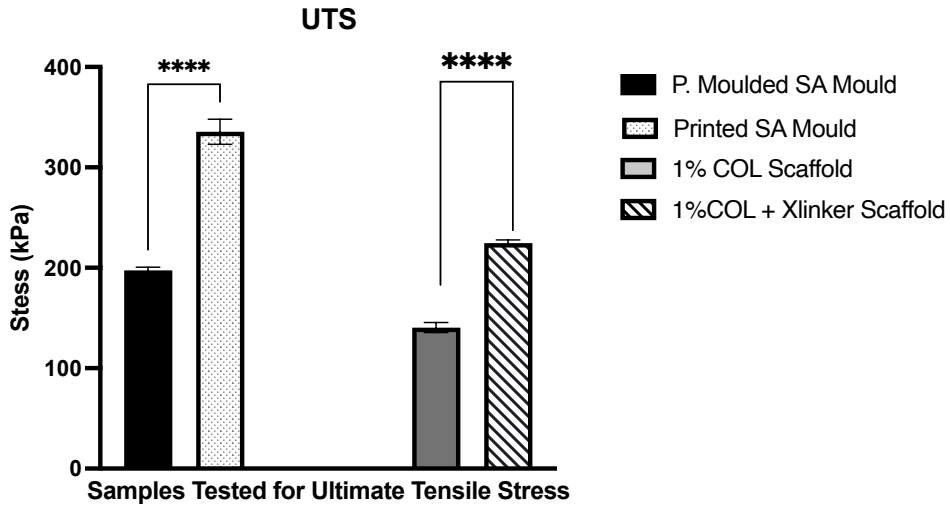

Figure 4.12: Plotting the ultimate tensile stress for different materials. It is observed that printed stearic acid specimens are stronger (UTS = 335kPa) compared to those that were moulded in PDMS (UTS = 197kPa). Scaffolds crosslinked with EDC-NHS chemical crosslinker showed ultimate tensile stress of 225kPa as opposed to the uncrosslinked scaffolds with an ultimate tensile stress of 140kPa ag Data obtained from a DMA machine. Data reported as mean ± SD. (****)$p<0.0001$, n=4.

The collagen scaffolds need to offer the necessary mechanical strength and withstand any forces exerted by the cells because of the growing tissue during the tissue engineering process. On the other hand, the stearic acid moulds need to be strong enough to handle any forces resulting from handling them during subsequent processes before they are sacrificially removed from the scaffold.

The mechanical properties of the collagen scaffolds and stearic acids were assessed. This was done by preparing samples that were subjected to tensile tests on a dynamic mechanical analyzer (TA 3200 DMA Machine, TA instruments).

Analysis of these samples shown in **Fig. 4.14** using Graphpad to yield the results obtained from the DMA machine showed that 1% collagen had ultimate tensile stress of 140kPa. It's young's modulus was 2.5 GPa. As can be observed from **Fig.4.12(C)**, this was very brittle.

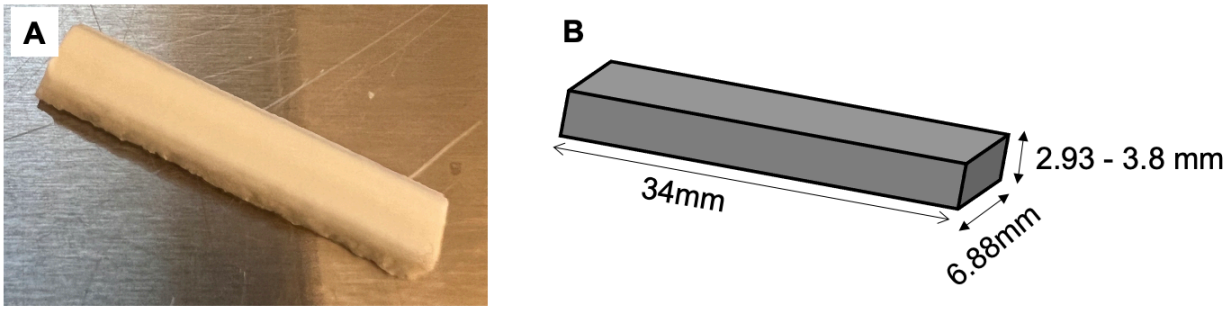

Figure 4.13: Samples used for tensile tests on the DMA machine. Samples for both collagen and stearic acid were based on image B which is adapted from ASTM D638 dog bone tensile specimen. Image A shows the stearic acid sample.

A chemical crosslinker, EDC-NHS was used to improve the mechanical properties of this scaffold. A tensile test showed an improved ultimate tensile stress of 225kPa. Its elasticity also improved to a reduced young's modulus of 0.5Gpa. This improved elasticity allows cells allows the scaffold to stretch on force application from cellular activity.

Young's modulus was calculated using Eq. 4.2 while the ultimate tensile stress was obtained directly from graphpad.

$$Young's\ Modulus\ (E) = \frac{Stress}{Strain} \qquad \text{Eq. 4.2}$$

4.8 Printer Optimization

To maintain precision, the printer had to be improved so that the printed surface of the stearic acid mould could match that of induracast. The printer works by releasing tiny droplets of print material at a frequency of about 9000Hz. The manufacturer has set the print heads to a hold voltage set at 50V and a fire voltage set at 20V.

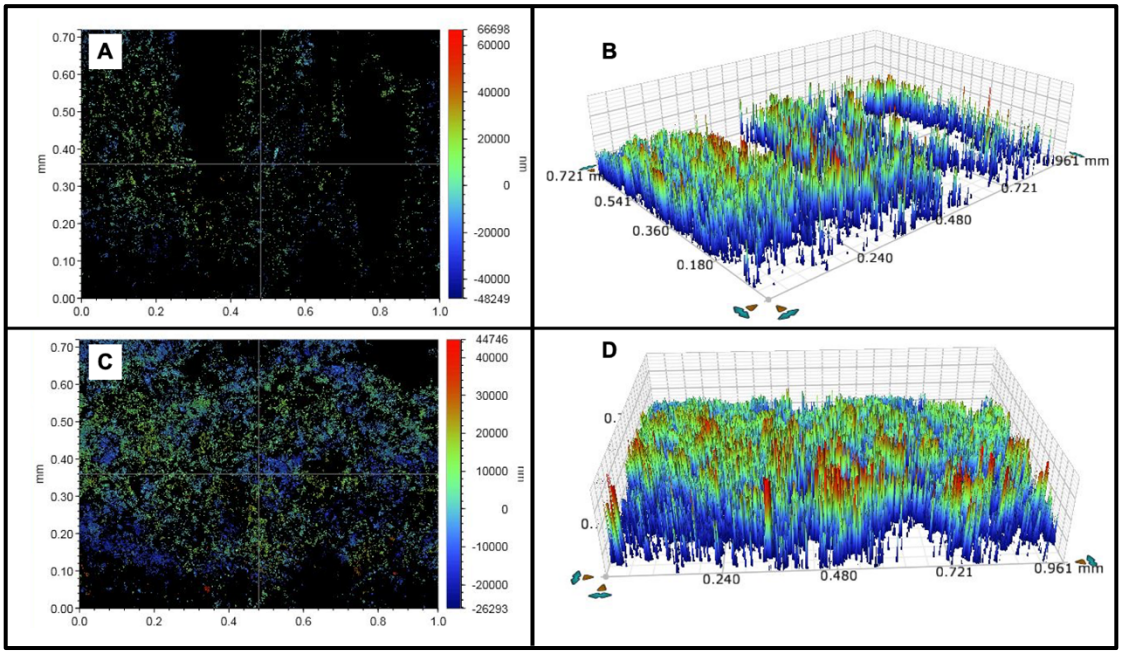

Figure 4.14: Optical profile Comparing the printed surface of stearic acid **(A)** and **(B)** to that of induracast, **(C)** and **(D)**. The printed surface of induracast was printed without the activation of the cutter.

Initial prints obtained by the 3D printer had an irregular surface with the difference between the highest ridges and deepest valleys being up to 2mm. Experiments were conducted whereby the hold and fire voltages for the print head were adjusted, and the obtained prints were inspected for roughness and compared to induracast.

The printer is not configured to print below 350mg of induracast per square inch in one printing layer. However due to density differences, 350mg of stearic acid is a large volume. (Approx. $3cm^3$) This is a very large amount. Subsequent adjustments resulted in the actual weight of SA being 130mg per square inch.

The printer was 'tricked' into believing that it was printing 350mg of SA while in the actual sense it was depositing 130mg per square inch. This adjusted the hold voltage for stearic acid at 65v for high volume print and 45v for low volume print. Similar adjustments were made to the support material head which was 'tricked' to believe it was depositing 288mg per square inch, while the actual deposition was 166mg. A print surface check for stearic acid and induracast moulds yielded print surfaces that were within a range of 20µm. These results can be seen in the optical profiler analysis in **Figure 4.14.**

Chapter 5: Tissue Culture

5.1 Cell Seeding and Tissue Culturing

The scaffolds were examined for biocompatibility. A blade was used to slice open the scaffold exposing the microchannel. After crosslinking the collagen scaffolds, they were thoroughly washed in Phosphate Buffered Solution (Dubelcco's phosphate-buffered saline (PBS) powder (Cat.# D5652, Sigma Aldrich Co. Ltd., UK) diluted in MilliQ water and sterilized) and placed in 15ml tubes and sterilized using 25 kGy gamma irradiation.

Human Umbilical Vein Endothelial Cells (HUVECs) were used to study the biocompatibility of the fabricated scaffolds. A HUVEC TERT-2 (hTERT-2) cell line (American Type Culture Collection - ATCC) was obtained and expanded in endothelial basal medium (EBM) (Lonza, BioWhittaker, Switzerland, Cat. # CC-3121) tissue culture media. Irradiated scaffolds were washed in the tissue culture media (EBM) (Lonza, BioWhittaker, Switzerland, Cat. # CC-3121) and left in an incubator at 37^0C, 5% CO_2 (Thermo-Scientific, Forma, Steri-Cycle) for 24h. Using a micropipette, a suspension of HUVECs was seeded onto the microchannels at 50,000 cells per scaffold. The seeded scaffolds were incubated for 72 hours and protected from light at 37^0C, with 5% CO_2 saturation (Thermo-Scientific, Forma, Steri-Cycle).

To observe the effect of the engineered scaffolds on the seeded cells, the cells were analyzed using an Alamar Blue assay for viability whereby the cells were stained with Alamar Blue (Invitrogen, USA) and incubated for 4 hours at 37^0C, 5% CO2 saturation (Thermo-Scientific, Forma, Steri-Cycle). An Alamar blue assay was used to evaluate the population of the cells.

The cells were fixed on the scaffolds by washing in formalin (4% paraformaldehyde solution prepared from reagent-grade paraformaldehyde (Sigma Aldrich, UK, Cat. # 1003163480)) for 30 minutes. The fixed scaffolds were then placed in PBS awaiting imaging. SEM images were obtained under environmental conditions (Quanta 3D, Thermofisher, USA) to examine their interaction with the scaffold. **Figure 5.1** shows a section though the scaffold that was observed under an SEM.

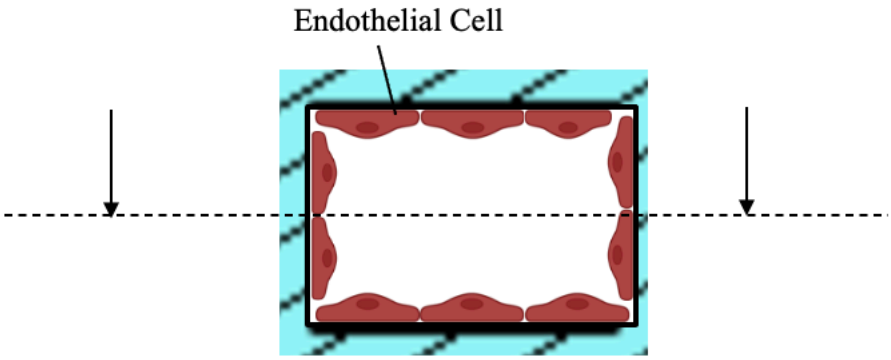

Figure 5.1: A section of the scaffold with endothelial cells was imaged. The scaffolds have a lumen lined with endothelial cells, which have been sectioned and imaged using an SEM.

5.2 Analysing Scaffold-Cellular Interaction.

An analysis of SEM images of the seeded scaffolds showed that the cells interacted with the scaffolds forming cytoplasmic projections that attach to neighbouring cells as well as the scaffold.

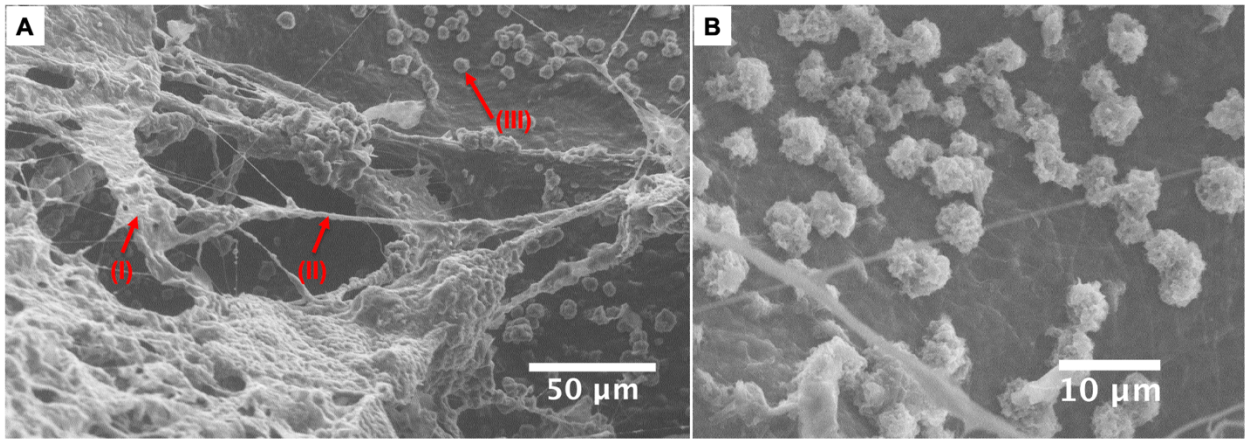

Figure 5.2: (A) Shows an SEM of the fabricated scaffolds showing cell attachment on the surface of the fabricated scaffolds subjected to static growing conditions for 72h. Looking at the red arrows, **(I)** shows the cytoplasmic projections of multiple HUVECs, **(II)** shows the cytoplasmic projections (filopodia) of an individual endothelial cell. **(III)** Bacteria attached to the scaffolds showing contamination of the scaffolds. **(B)** shows a higher magnification SEM micrograph focussing on the contamination.

This can be observed in **Fig. 5.2** which shows this interaction. This figure shows that the cells interact well with the scaffold surface. Typically, cells attach to the surface in about 12-24h and start dividing in 24-48h[225]. The seeded cells have attached by developing filopodia. The fact that at 72h cells can be observed attached to these scaffolds shows that the scaffolds are biocompatible. The ideal biological scaffold is the native ECM in which these cells would naturally grow. This is because it contains all the components needed to support the living of the cells as well as the mechanical characteristics to provide the mechanical support for the proper tissue function.

An observation of **Fig. 5.2** also reveals the presence of bacteria growing alongside the HUVECs. These bacteria are most likely because of the processing carried out on the scaffolds pre- and post-seeding. Likely sources of contamination include: (1) The scaffolds remained in media for up to 48h prior to seeding with cells. There is a likelihood that the hydration process introduced bacteria to the scaffold surfaces, and the period before seeding gave the bacteria time to grow. (2) Contaminated equipment may have introduced bacteria to the scaffolds when seeding the cells.

It can therefore be considered that these scaffolds are biocompatible and can support the growth of HUVECs. This makes it possible to explore the creation of microvascular networks in the scaffold that can be employed in tissue engineering by providing a vascularized scaffold for thick tissue engineering.

Chapter 6: Thesis Summary and Future Work

6.1 Thesis Summary

In this study, a 3D printer (Solidscape 612bt, Stratasys) was used. This 3D printer uses induracast and indurasupport as the printing materials. While this printer can successfully use its high precision 3D printing technique to create highly precise inverse moulds, its printing materials are highly cytotoxic. Induracast melts at ~115^{o}C while indurasupport melts at ~85^{o}C. At the recommended printing temperatures, induracast and indurasupport had flow viscosities of ~22.5 mPa.s and ~20 mPa.s respectively. A material survey was conducted to identify biocompatible polymers that could be used to replace the printing materials. Polyethylene Glycol (PEG) with a melting temperature of 64^{o}C was recommended as an ideal replacement for indurasupport while stearic acid (SA) with a melting point of 68^{o}C was recommended as an ideal replacement for induracast.

The viscosity of these materials was evaluated using a dynamic mechanical analyzer, which was found to be 18 mPa.s for PEG and 15 mPa.s for SA. Their ideal printing temperatures were determined as 110^{o}C for PEG and 120^{o}C for SA.

The printer was used to print inverse moulds and collagen scaffolds produced by casting a slurry in the mould and freezing it. 1% w/v collagen concentration was used with the freezing temperature being -20^{o}C. The produced scaffolds were crosslinked in NHS/EDC. Crosslinked scaffolds had improved strength, with the UTS increasing to 225kPA from 140kPa for uncrosslinked collagen scaffolds. Crosslinking also improved elasticity by lowering the young's modulus to 0.5GPa from 2.5 GPa.

When compared to stearic acid scaffolds made by moulding in PDMS, printed scaffolds proved to be stronger, with a UTS of 335kPa compared to 197kPa for moulded scaffolds. Improving the wash time for moulds was also analysed, and it was considered that the printed moulds needed to be washed for 12h to ensure removal of all the support material and ensure exposure of up to 100% of internal architecture to interact with collagen slurry.

Ultimately cells were seeded on sterilized scaffolds and incubated for 72h. SEM micrographs of cells fixed on the scaffolds with formalin showed that the cells interacted with the scaffolds and each other with adequate filopodia growth. It was, however, observed that the cells grew alongside a colony of bacteria due to contamination introduced during seeding.

Despite continuous progress in tissue engineering, a fabrication method using readily available biocompatible material to fabricate scaffolds that contain microchannels is not available yet. We present a novel method of using readily available materials that can be used in commercially available 3D printers to fabricate tissue constructs that promote the growth of blood vessels and increase cell penetration and viability. This sets a stage for high throughput tissue engineering scaffolds containing functional perfusable vasculature that will promote the production of thick engineered tissues for transplant or disease modeling and drug screening.

6.2 Limitations and Future Recommendations

In this thesis, we have repurposed a commercially available 3D printer to fabricate scaffolds for tissue engineering. One layer of vascularization can be made possible by the scaffolds that have been fabricated here. However, it will be of great interest to fabricate scaffolds that can be as thick as 1 cm^3. Vascularization of these thick scaffolds will make it possible to achieve the engineering of thicker tissues. The repurposed 3D printer dislodged the printed mould whenever the printer's mill was activated, and the print specimen reached a printing height that was >~7mm. Finding a bonding agent that will firmly attach the printed mould firmly to the print bed will make it possible to print taller (>7mm) specimens.

It was observed that as taller prints were being printed, an SA print layer on top of a PEG layer caused the PEG layer to melt. The printed surfaces need to have a perfectly flat layer. A method for rapidly cooling the SA layer will ensure that the PEG layer below it is not melted. It is recommended to find a method to make this rapid cooling possible as it will make printing taller moulds feasible.

The methods described in this thesis led to the introduction of bacteria/contamination, as observed in **Fig. 5.2.** The seeding and incubation technique needs to be improved so as not to introduce any contamination to the tissue as this would reduce the vessel forming capacity of the engineered tissue.

Ultimately, the ECM is made up of various components. To obtain functional tissue, it is recommended to fabricate scaffolds with multiple ECM components and investigate the integrity of perfused vessels formed by these scaffolds.

APPENDIX

Appendix 1. Comparison of the dissolution of PEG and SA in water and ethanol.

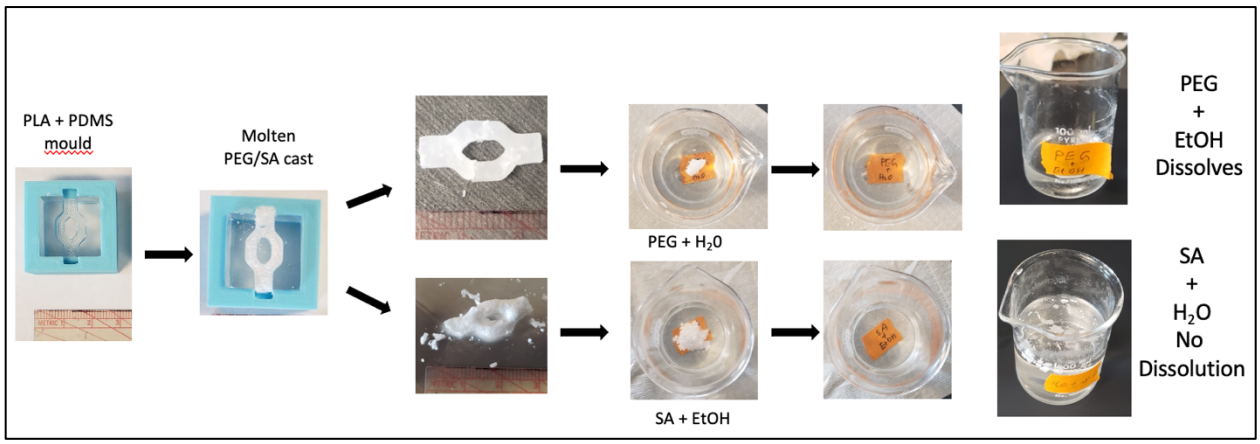

Supplemental Figure 1. Investigating the dissolution of stearic acid and polyethylene glycol in water and ethanol. PDMS moulds were used to cast samples of PEG and SA. PEG dissolved in both water and ethanol while SA dissolved in ethanol only.

Appendix 2. Chemical Formula for the printing material

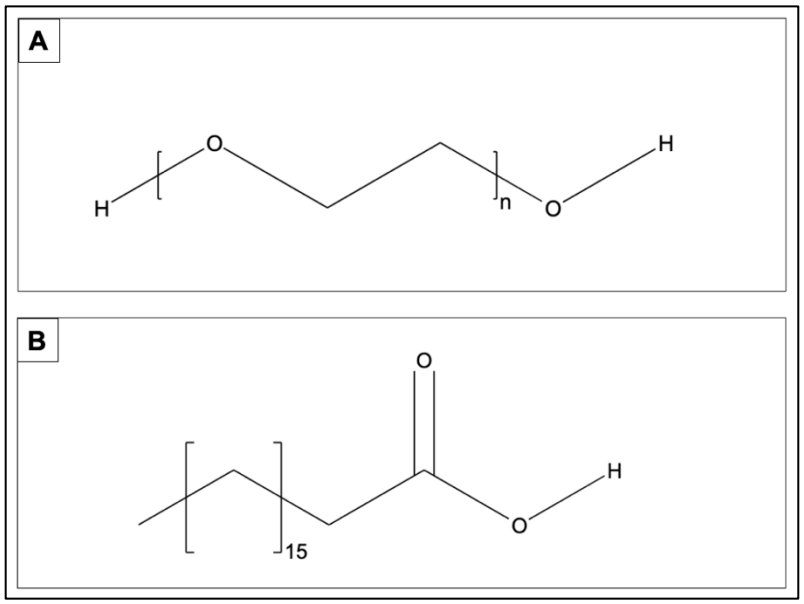

Supplemental Figure 2. Chemical formula for A, Polyethylene Glycol (PEG) and B, Stearic Acid (SA). These monomers combine into long polymer chains.

Appendix 3. Investigating sources of printing challenges at the print heads.

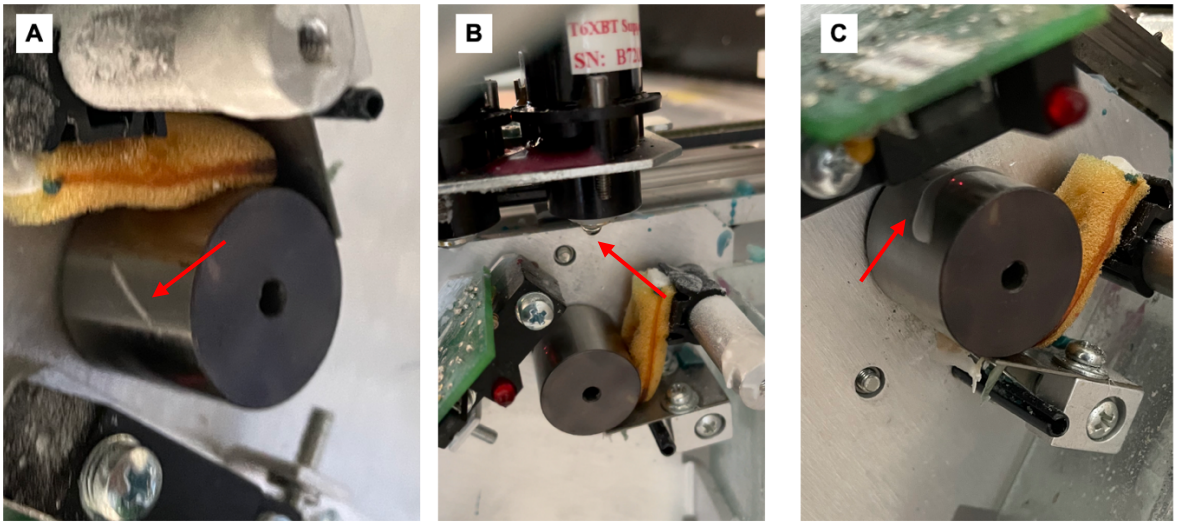

Supplemental Figure 3. (A) Shows a proper line printed on the jet check drum during the jet check process. To obtain this perfect print, the jet is not clogged with impurities or blocked by the accumulation of molten print material – jet wetting which can be seen in **(B).** Shows a situation where material fills up on the print head jet blocking the deposition of printer material on the print bed during a normal printing procedure. **(C)** Is the result of a wet jet depositing material on the jet check drum. Factors that led to jet wetting included high ambient temperature, the low molecular weight of the printing material, high ambient humidity and continuous printing for extended periods (>3hrs) without cleaning the jet.

REFERENCES

1. Do, A.-V., Khorsand, B., Geary, S. M. & Salem, A. K. 3D Printing of Scaffolds for Tissue Regeneration Applications. *Adv. Healthc. Mater.* **4**, 1742–1762 (2015).
2. Atala, A., Bauer, S. B., Soker, S., Yoo, J. J. & Retik, A. B. Tissue-engineered autologous bladders for patients needing cystoplasty. *Lancet* **367**, 1241–1246 (2006).
3. Kolesky, D. B. *et al.* 3D bioprinting of vascularized, heterogeneous cell-laden tissue constructs. *Adv. Mater.* **26**, 3124–3130 (2014).
4. Beyar, R. Challenges in Organ Transplantation. *Rambam Maimonides Med. J.* **2**, 1–10 (2011).
5. Abouna, G. M. Organ Shortage Crisis: Problems and Possible Solutions. *Transplant. Proc.* **40**, 34–38 (2008).
6. Datta, P. *et al.* Essential steps in bioprinting: From pre- to post-bioprinting. *Biotechnol. Adv.* **36**, 1481–1504 (2018).
7. Knowlton, S. *et al.* Advancing cancer research using bioprinting for tumor-on-a-chip platforms. *Int. J. Bioprinting* **2**, 3–8 (2016).
8. Elson, E. L. & Genin, G. M. Tissue constructs: Platforms for basic research and drug discovery. *Interface Focus* **6**, (2016).
9. Farbod, K., Nejadnik, M. R., Jansen, J. A. & Leeuwenburgh, S. C. G. Interactions Between Inorganic and Organic Phases in Bone Tissue as a Source of Inspiration for Design of Novel Nanocomposites. *Tissue Eng. - Part B Rev.* **20**, 173–188 (2014).

10. Laurencin, C. T., Ambrosio, A. M. A., Borden, M. D. & Cooper, J. A. Tissue engineering: Orthopedic applications. *Annu. Rev. Biomed. Eng.* 19–46 (1999) doi:10.1146/annurev.bioeng.1.1.19.

11. Dallas, S. L., Prideaux, M. & Bonewald, L. F. The osteocyte: An endocrine cell . . . and more. *Endocr. Rev.* **34**, 658–690 (2013).

12. O'Brien, F. J., Harley, B. A., Yannas, I. V. & Gibson, L. Influence of freezing rate on pore structure in freeze-dried collagen-GAG scaffolds. *Biomaterials* **25**, 1077–1086 (2004).

13. O'Brien, F. J. *et al.* The effect of pore size on permeability and cell attachment in collagen scaffolds for tissue engineering. *Technol. Heal. Care* **15**, 3–17 (2007).

14. Guo, B. & Ma, P. X. Synthetic biodegradable functional polymers for tissue engineering: A brief review. *Sci. China Chem.* **57**, 490–500 (2014).

15. Starnecker, F., König, F., Hagl, C. & Thierfelder, N. Tissue-engineering acellular scaffolds—The significant influence of physical and procedural decellularization factors. *J. Biomed. Mater. Res. - Part B Appl. Biomater.* **106**, 153–162 (2018).

16. Sobrino, A. *et al.* 3D microtumors in vitro supported by perfused vascular networks. *Sci. Rep.* **6**, 1–11 (2016).

17. Zheng, Y. *et al.* In vitro microvessels for the study of angiogenesis and thrombosis. *Proc. Natl. Acad. Sci. U. S. A.* **109**, 9342–9347 (2012).

18. Armiento, A. R., Hatt, L. P., Sanchez Rosenberg, G., Thompson, K. & Stoddart, M. J. Functional Biomaterials for Bone Regeneration: A Lesson in Complex Biology. *Adv. Funct. Mater.* **30**, 1–41 (2020).

19. Cunniffe, G. M. & O'Brien, F. J. Collagen scaffolds for orthopedic regenerative medicine. *Jom* **63**, 66–73 (2011).

20. Hutmacher, D. W. Scaffold design and fabrication technologies for engineering tissues - State of the art and future perspectives. *J. Biomater. Sci. Polym. Ed.* **12**, 107–124 (2001).

21. Chan, W. W. *et al.* Additive biomanufacturing with collagen inks. *Bioengineering* **7**, 1–23 (2020).

22. Han, L., Zhang, Z. wen, Wang, B. he & Wen, Z. kun. Construction and biocompatibility of a thin type I/II collagen composite scaffold. *Cell Tissue Bank.* **19**, 47–59 (2018).

23. Wolf, K. *et al.* Collagen-based cell migration models in vitro and in vivo. *Semin. Cell Dev. Biol.* **20**, 931–941 (2009).

24. Sorushanova, A. *et al.* The Collagen Suprafamily: From Biosynthesis to Advanced Biomaterial Development. *Adv. Mater.* **31**, (2019).

25. Koch, L. *et al.* Skin tissue generation by laser cell printing. *Biotechnol. Bioeng.* **109**, 1855–1863 (2012).

26. Cen, L., Liu, W., Cui, L., Zhang, W. & Cao, Y. Collagen tissue engineering: Development of novel biomaterials and applications. *Pediatr. Res.* **63**, 492–496 (2008).

27. Taylor, P. M. *et al.* Interaction of human valve interstitial cells with collagen matrices manufactured using rapid prototyping. *Biomaterials* **27**, 2733–2737 (2006).

28. Copes, F., Pien, N., Van Vlierberghe, S., Boccafoschi, F. & Mantovani, D. Collagen-based tissue engineering strategies for vascular medicine. *Front. Bioeng. Biotechnol.* **7**, 1–15 (2019).

29. Kim, W. J., Jang, C. H. & Kim, G. H. Optimally designed collagen/polycaprolactone biocomposites supplemented with controlled release of HA/TCP/rhBMP-2 and HA/TCP/PRP for hard tissue regeneration. *Mater. Sci. Eng. C* **78**, 763–772 (2017).

30. Sachlos, E., Reis, N., Ainsley, C., Derby, B. & Czernuszka, J. T. Novel collagen scaffolds with predefined internal morphology made by solid freeform fabrication. *Biomaterials* **24**, 1487–1497 (2003).

31. Zhang, X., Tang, K. & Zheng, X. Electrospinning and rheological behavior of poly (vinyl alcohol)/collagen blended solutions. *J. Wuhan Univ. Technol. Mater. Sci. Ed.* **30**, 840–846 (2015).

32. Melčová, V. *et al.* Fdm 3d printed composites for bone tissue engineering based on plasticized poly(3-hydroxybutyrate)/poly(d,l-lactide) blends. *Polymers (Basel).* **12**, 1–19 (2020).

33. Skoog, S. A., Goering, P. L. & Narayan, R. J. Stereolithography in tissue engineering. *J. Mater. Sci. Mater. Med.* **25**, 845–856 (2014).

34. Williams, J. M. *et al.* Bone tissue engineering using polycaprolactone scaffolds fabricated via selective laser sintering. *Biomaterials* **26**, 4817–4827 (2005).

35. Justin, A. W., Brooks, R. A. & Markaki, A. E. Multi-casting approach for vascular networks in cellularized hydrogels. *J. R. Soc. Interface* **13**, (2016).

36. Levato, R. *et al.* Biofabrication of tissue constructs by 3D bioprinting of cell-laden microcarriers. *Biofabrication* **6**, (2014).

37. Pirraco, R. P., Marques, A. P. & Reis, R. L. Cell interactions in bone tissue engineering. *J. Cell. Mol. Med.* **14**, 93–102 (2010).

38. Khalil, S., Nam, J. & Sun, W. Multi-nozzle deposition for construction of 3D biopolymer tissue scaffolds. *Rapid Prototyp. J.* **11**, 9–17 (2005).

39. Nair, K. *et al.* Characterization of cell viability during bioprinting processes. *Biotechnol. J.* **4**, 1168–1177 (2009).

40. Bertassoni, L. E. *et al.* Hydrogel bioprinted microchannel networks for vascularization of tissue engineering constructs. *Lab Chip* **14**, 2202–2211 (2014).

41. Radisic, M. *et al.* Medium perfusion enables engineering of compact and contractile cardiac tissue. *Am. J. Physiol. - Hear. Circ. Physiol.* **286**, 507–516 (2004).

42. Sartore, L., Pandini, S., Dey, K., Bignotti, F. & Chiellini, F. Materialia A versatile cell-friendly approach to produce PLA-based 3D micro-macro-porous blends for tissue engineering scaffolds. *Materialia* **9**, 100615 (2020).

43. Porter, J. R., Ruckh, T. T. & Popat, K. C. Bone tissue engineering: A review in bone biomimetics and drug delivery strategies. *Biotechnol. Prog.* **25**, 1539–1560 (2009).

44. Sachlos, E., Czernuszka, J. T., Gogolewski, S. & Dalby, M. Making tissue engineering scaffolds work. Review on the application ofsolid freeform fabrication technology to the production of tissue engineeringscaffolds. *Eur. Cells Mater.* **5**, 29–40 (2003).

45. An, J., Teoh, J. E. M., Suntornnond, R. & Chua, C. K. Design and 3D Printing of Scaffolds and Tissues. *Engineering* **1**, 261–268 (2015).

46. Tarafder, S., Balla, V. K., Davies, N. M., Bandyopadhyay, A. & Bose, S. Microwave-sintered 3D printed tricalcium phosphate scaffolds for bone tissue engineering. *J. Tissue Eng. Regen. Med.* **7**, 631–641 (2013).

47. Bjerre, L., Bünger, C. E., Kassem, M. & Mygind, T. Flow perfusion culture of human mesenchymal stem cells on silicate-substituted tricalcium phosphate scaffolds. *Biomaterials* **29**, 2616–2627 (2008).

48. Li, S. H., De Wijn, J. R., Layrolle, P. & De Groot, K. Synthesis of macroporous hydroxyapatite scaffolds for bone tissue engineering. *J. Biomed. Mater. Res. An Off. J. Soc. Biomater. Japanese Soc. Biomater. Aust. Soc. Biomater. Korean Soc. Biomater.* **61**, 109–120 (2002).

49. Bose, S. *et al.* Processing and characterization of porous alumina scaffolds. *J. Mater. Sci. Mater. Med.* **13**, 23–28 (2002).

50. Gaddam, A., Brazete, D. S., Neto, A. S., Nan, B. & Ferreira, J. M. F. Three-dimensional printing of zirconia scaffolds for load bearing applications: Study of the optimal fabrication conditions. *J. Am. Ceram. Soc.* **104**, 4368–4380 (2021).

51. Burwell, A. K., Litkowski, L. J. & Greenspan, D. C. Calcium sodium phosphosilicate (NovaMin®): remineralization potential. *Adv. Dent. Res.* **21**, 35–39 (2009).

52. Day, R. M. *et al.* Assessment of polyglycolic acid mesh and bioactive glass for soft-tissue engineering scaffolds. *Biomaterials* **25**, 5857–5866 (2004).

53. Hench, L. L., Jones, J. R. & Sepulveda, P. Bioactive Materials for Tissue Engineering Scaffolds. *Futur. Strateg. Tissue Organ Replace.* 3–24 (2002) doi:10.1142/9781860949647_0001.

54. Hench, L. L. Sol-gel materials for bioceramic applications. *Curr. Opin. Solid State Mater. Sci.* **2**, 604–610 (1997).

55. Williams, D. Benefit and risk in tissue engineering. *Mater. Today* **7**, 24–29 (2004).

56. Gogolewski, S., Jovanovic, M., Perren, S. M., Dillon, J. G. & Hughes, M. K. Tissue response and in vivo degradation of selected polyhydroxyacids: Polylactides (PLA), poly (3-hydroxybutyrate)(PHB), and poly (3-hydroxybutyrate-co-3-hydroxyvalerate)(PHB/VA). *J. Biomed. Mater. Res.* **27**, 1135–1148 (1993).

57. Ma, P. X. & Zhang, R. Microtubular architecture of biodegradable polymer scaffolds. *J. Biomed. Mater. Res. An Off. J. Soc. Biomater. Japanese Soc. Biomater. Aust. Soc. Biomater. Korean Soc. Biomater.* **56**, 469–477 (2001).

58. Agrawal, C. M. & Ray, R. B. Biodegradable polymeric scaffolds for musculoskeletal tissue engineering. *J. Biomed. Mater. Res. An Off. J. Soc. Biomater. Japanese Soc. Biomater. Aust. Soc. Biomater. Korean Soc. Biomater.* **55**, 141–150 (2001).

59. Wu, L. & Ding, J. In vitro degradation of three-dimensional porous poly (D, L-lactide-co-glycolide) scaffolds for tissue engineering. *Biomaterials* **25**, 5821–5830 (2004).

60. Shaharuddin, S. & Matthews, Z. FL and Rawlings. *RD, Compos. Mater. Eng. Sci. Chapman Hall, London* (1994).

61. Ramakrishna, S., Mayer, J., Wintermantel, E. & Leong, K. W. Biomedical applications of polymer-composite materials: a review. *Compos. Sci. Technol.* **61**, 1189–1224 (2001).

62. Ninan, N. *et al.* Wound healing analysis of pectin/carboxymethyl cellulose/microfibrillated cellulose based composite scaffolds. *Mater. Lett.* **132**, 34–37 (2014).

63. Munarin, F., Tanzi, M. C. & Petrini, P. Advances in biomedical applications of pectin gels. *Int. J. Biol. Macromol.* **51**, 681–689 (2012).

64. Navajas, E. V. *et al.* Concentration of hyaluronic acid in primary open-angle glaucoma aqueous humor. *Exp. Eye Res.* **80**, 853–857 (2005).

65. Scuderi, N. *et al.* The clinical application of autologous bioengineered skin based on a hyaluronic acid scaffold. *Biomaterials* **29**, 1620–1629 (2008).

66. Kleinberg, T. T., Tzekov, R. T., Stein, L., Ravi, N. & Kaushal, S. Vitreous substitutes: a comprehensive review. *Surv. Ophthalmol.* **56**, 300–323 (2011).

67. Lei, Y., Gojgini, S., Lam, J. & Segura, T. The spreading, migration and proliferation of mouse mesenchymal stem cells cultured inside hyaluronic acid hydrogels. *Biomaterials* **32**, 39–47 (2011).

68. Chang, K.-V., Hsiao, M.-Y., Chen, W.-S., Wang, T.-G. & Chien, K.-L. Effectiveness of intra-articular hyaluronic acid for ankle osteoarthritis treatment: a systematic review and meta-analysis. *Arch. Phys. Med. Rehabil.* **94**, 951–960 (2013).

69. Croisier, F. & Jérôme, C. Chitosan-based biomaterials for tissue engineering. *Eur. Polym. J.* **49**, 780–792 (2013).

70. Toskas, G. *et al.* Ulvan and ulvan/chitosan polyelectrolyte nanofibrous membranes as a potential substrate material for the cultivation of osteoblasts. *Carbohydr. Polym.* **89**, 997–1002 (2012).

71. Chen, S.-H. *et al.* Assessment of reinforced poly (ethylene glycol) chitosan hydrogels as dressings in a mouse skin wound defect model. *Mater. Sci. Eng. C* **33**, 2584–2594 (2013).

72. Sikareepaisan, P., Ruktanonchai, U. & Supaphol, P. Preparation and characterization of asiaticoside-loaded alginate films and their potential for use as effectual wound dressings. *Carbohydr. Polym.* **83**, 1457–1469 (2011).

73. Kim, J. O. *et al.* Development of polyvinyl alcohol–sodium alginate gel-matrix-based wound dressing system containing nitrofurazone. *Int. J. Pharm.* **359**, 79–86 (2008).

74. Pawar, S. N. & Edgar, K. J. Alginate derivatization: A review of chemistry, properties and applications. *Biomaterials* **33**, 3279–3305 (2012).

75. Nair, L. S. & Laurencin, C. T. Polymers as biomaterials for tissue engineering and controlled drug delivery. *Tissue Eng. I* 47–90 (2005).

76. McGuigan, A. P. & Sefton, M. V. The thrombogenicity of human umbilical vein endothelial cell seeded collagen modules. *Biomaterials* **29**, 2453–2463 (2008).

77. Abou Neel, E. A. *et al.* Collagen—emerging collagen based therapies hit the patient. *Adv. Drug Deliv. Rev.* **65**, 429–456 (2013).

78. Fleck, C. A. & Simman, R. Modern collagen wound dressings: function and purpose. *J. Am. Col. Certif. Wound Spec.* **2**, 50–54 (2010).

79. Liu, Y., Ren, L. & Wang, Y. Crosslinked collagen–gelatin–hyaluronic acid biomimetic film for cornea tissue engineering applications. *Mater. Sci. Eng. C* **33**, 196–201 (2013).

80. Filippi, M., Born, G., Chaaban, M. & Scherberich, A. Natural Polymeric Scaffolds in Bone Regeneration . *Frontiers in Bioengineering and Biotechnology* vol. 8 (2020).

81. Boffito, M., Sartori, S. & Ciardelli, G. Polymeric scaffolds for cardiac tissue engineering: requirements and fabrication technologies. *Polym. Int.* **63**, 2–11 (2014).

82. Ge, Z., Jin, Z. & Cao, T. Manufacture of degradable polymeric scaffolds for bone regeneration. *Biomed. Mater.* **3**, 22001 (2008).

83. Smink, A. M., de Haan, B. J., Lakey, J. R. T. & de Vos, P. Polymer scaffolds for pancreatic islet transplantation—Progress and challenges. *Am. J. Transplant.* **18**, 2113–2119 (2018).

84. Maquet, V. & Jerome, R. Design of macroporous biodegradable polymer scaffolds for cell transplantation. in *Materials Science Forum* vol. 250 15–42 (Trans Tech Publ, 1997).

85. Halake, K. *et al.* Recent application developments of water-soluble synthetic polymers. *J. Ind. Eng. Chem.* **20**, 3913–3918 (2014).

86. Simionescu, B. C. & Ivanov, D. Natural and synthetic polymers for designing composite materials. in *Handbook of bioceramics and biocomposites* 233–286 (Springer, 2016).

87. Ghosh, S. Recent research and development in synthetic polymer-based drug delivery systems. *J. Chem. Res.* **2004**, 241–246 (2004).

88. Tokiwa, Y., Ando, T., Suzuki, T. & Takeda, K. Biodegradation of synthetic polymers containing ester bonds. in (ACS Publications, 1990).

89. Berda, E. B., Foster, E. J. & Meijer, E. W. Toward controlling folding in synthetic polymers: fabricating and characterizing supramolecular single-chain nanoparticles. *Macromolecules* **43**, 1430–1437 (2010).

90. Grémare, A. *et al.* Characterization of printed PLA scaffolds for bone tissue engineering. *J. Biomed. Mater. Res. Part A* **106**, 887–894 (2018).

91. Shu, X., Shi, Q., Feng, J., Xie, X. & Chen, Y. Design and in vitro evaluation of novel γ-PGA/hydroxyapatite nanocomposites for bone tissue engineering. *J. Mater. Sci.* **49**, 7742–7749 (2014).

92. Holy, C. E., Cheng, C., Davies, J. E. & Shoichet, M. S. Optimizing the sterilization of PLGA scaffolds for use in tissue engineering. *Biomaterials* **22**, 25–31 (2000).

93. Patricio, T., Domingos, M., Gloria, A. & Bártolo, P. Characterisation of PCL and PCL/PLA scaffolds for tissue engineering. *Procedia Cirp* **5**, 110–114 (2013).

94. Prasad, A., Sankar, M. R. & Katiyar, V. State of art on solvent casting particulate leaching method for orthopedic scaffoldsfabrication. *Mater. Today Proc.* **4**, 898–907 (2017).

95. Hernandez, H. L. *et al.* Processing-dependent mechanical properties of solvent cast cyclic polyphthalaldehyde. *Polymer (Guildf).* **162**, 29–34 (2019).

96. Nam, Y. S., Yoon, J. J. & Park, T. G. A novel fabrication method of macroporous biodegradable polymer scaffolds using gas foaming salt as a porogen additive. *J. Biomed. Mater. Res. An Off. J. Soc. Biomater. Japanese Soc. Biomater. Aust. Soc. Biomater. Korean Soc. Biomater.* **53**, 1–7 (2000).

97. Brougham, C. M. *et al.* Freeze-drying as a novel biofabrication method for achieving a controlled microarchitecture within large, complex natural biomaterial scaffolds. *Adv. Healthc. Mater.* **6**, 1700598 (2017).

98. Matthews, J. A., Boland, E. D., Wnek, G. E., Simpson, D. G. & Bowlin, G. L. Electrospinning of collagen type II: a feasibility study. *J. Bioact. Compat. Polym.* **18**, 125–134 (2003).

99. Brinckmann, S. A., Lakhera, N., Laursen, C. M., Yakacki, C. & Frick, C. P. Characterization of poly (para-phenylene)-MWCNT solvent-cast composites. *AIMS Mater. Sci.* **5**, 301–319 (2018).

100. Deng, L., Kang, X., Liu, Y., Feng, F. & Zhang, H. Characterization of gelatin/zein films fabricated by electrospinning vs solvent casting. *Food Hydrocoll.* **74**, 324–332 (2018).

101. Chia, O. C., Suhaimin, I. S., Kassim, S. A., Zubir, S. A. & Abdullah, T. K. Effect of modified solvent casting/particulate leaching (SCPL) technique on the properties of bioactive glass reinforced polyurethane scaffold for biomedical applications. *J. Phys. Sci.* **30**, 115–126 (2019).

102. Thadavirul, N., Pavasant, P. & Supaphol, P. Development of polycaprolactone porous scaffolds by combining solvent casting, particulate leaching, and polymer leaching techniques for bone tissue engineering. *J. Biomed. Mater. Res. Part A* **102**, 3379–3392 (2014).

103. Zhan, J., Sun, X., Cui, F. & Kong, X. Preparation of 3-D porous fibroin scaffolds by freeze drying with treatment of methanol solutions. *Chinese Sci. Bull.* **52**, 1791–1795 (2007).

104. Ho, M.-H. *et al.* Preparation of porous scaffolds by using freeze-extraction and freeze-gelation methods. *Biomaterials* **25**, 129–138 (2004).

105. Kane, R. J. & Roeder, R. K. Effects of hydroxyapatite reinforcement on the architecture and mechanical properties of freeze-dried collagen scaffolds. *J. Mech. Behav. Biomed. Mater.* **7**, 41–49 (2012).

106. Colosi, C. *et al.* Morphological comparison of PVA scaffolds obtained by gas foaming and microfluidic foaming techniques. *Langmuir* **29**, 82–91 (2013).

107. Yoon, J. J. & Park, T. G. Degradation behaviors of biodegradable macroporous scaffolds prepared by gas foaming of effervescent salts. *J. Biomed. Mater. Res. An Off. J. Soc. Biomater. Japanese Soc. Biomater. Aust. Soc. Biomater. Korean Soc. Biomater.* **55**, 401–408 (2001).

108. Montjovent, M.-O. *et al.* Biocompatibility of bioresorbable poly (L-lactic acid) composite scaffolds obtained by supercritical gas foaming with human fetal bone cells. *Tissue Eng.* **11**, 1640–1649 (2005).

109. Nam, Y. S. & Park, T. G. Porous biodegradable polymeric scaffolds prepared by thermally induced phase separation. *J. Biomed. Mater. Res. An Off. J. Soc. Biomater. Japanese Soc. Biomater. Aust. Soc. Biomater. Korean Soc. Biomater.* **47**, 8–17 (1999).

110. Akbarzadeh, R. & Yousefi, A. Effects of processing parameters in thermally induced phase separation technique on porous architecture of scaffolds for bone tissue engineering. *J. Biomed. Mater. Res. Part B Appl. Biomater.* **102**, 1304–1315 (2014).

111. Kim, J. F., Kim, J. H., Lee, Y. M. & Drioli, E. Thermally induced phase separation and electrospinning methods for emerging membrane applications: A review. *AIChE J.* **62**, 461–490 (2016).

112. Rnjak-Kovacina, J. & Weiss, A. S. Increasing the pore size of electrospun scaffolds. *Tissue Eng. Part B Rev.* **17**, 365–372 (2011).

113. Subbiah, T., Bhat, G. S., Tock, R. W., Parameswaran, S. & Ramkumar, S. S. Electrospinning of nanofibers. *J. Appl. Polym. Sci.* **96**, 557–569 (2005).

114. Thorvaldsson, A., Stenhamre, H., Gatenholm, P. & Walkenström, P. Electrospinning of highly porous scaffolds for cartilage regeneration. *Biomacromolecules* **9**, 1044–1049 (2008).

115. Shahrubudin, N., Lee, T. C. & Ramlan, R. An overview on 3D printing technology: Technological, materials, and applications. *Procedia Manuf.* **35**, 1286–1296 (2019).

116. Leukers, B. *et al.* Hydroxyapatite scaffolds for bone tissue engineering made by 3D printing. *J. Mater. Sci. Mater. Med.* **16**, 1121–1124 (2005).

117. Bose, S., Vahabzadeh, S. & Bandyopadhyay, A. Bone tissue engineering using 3D printing. *Mater. today* **16**, 496–504 (2013).

118. Haleem, A., Javaid, M., Khan, R. H. & Suman, R. 3D printing applications in bone tissue engineering. *J. Clin. Orthop. trauma* **11**, S118–S124 (2020).

119. Dawood, A., Marti, B. M., Sauret-Jackson, V. & Darwood, A. 3D printing in dentistry. *Br. Dent. J.* **219**, 521–529 (2015).

120. Yang, X. *et al.* Collagen-alginate as bioink for three-dimensional (3D) cell printing based cartilage tissue engineering. *Mater. Sci. Eng. C* **83**, 195–201 (2018).

121. Highley, C. B., Rodell, C. B. & Burdick, J. A. Direct 3D printing of shear-thinning hydrogels into self-healing hydrogels. *Adv. Mater.* **27**, 5075–5079 (2015).

122. Sachlos, E., Reis, N., Ainsley, C., Derby, B. & Czernuszka, J. T. Novel collagen scaffolds with predefined internal morphology made by solid freeform fabrication. *Biomaterials* **24**, 1487–1497 (2003).

123. Hassanajili, S., Karami-Pour, A., Oryan, A. & Talaei-Khozani, T. Preparation and characterization of PLA/PCL/HA composite scaffolds using indirect 3D printing for bone tissue engineering. *Mater. Sci. Eng. C* **104**, 109960 (2019).

124. Vashistha, R. *et al.* Quest for cardiovascular interventions: precise modeling and 3D printing of heart valves. *J. Biol. Eng.* **13**, 1–12 (2019).

125. Zhang, L., Yang, G., Johnson, B. N. & Jia, X. Three-dimensional (3D) printed scaffold and material selection for bone repair. *Acta Biomater.* **84**, 16–33 (2019).

126. Chimene, D., Lennox, K. K., Kaunas, R. R. & Gaharwar, A. K. Advanced bioinks for 3D printing: a materials science perspective. *Ann. Biomed. Eng.* **44**, 2090–2102 (2016).

127. Kantaros, A., Chatzidai, N. & Karalekas, D. 3D printing-assisted design of scaffold structures. *Int. J. Adv. Manuf. Technol.* **82**, 559–571 (2016).

128. Yan, Q. *et al.* A review of 3D printing technology for medical applications. *Engineering* **4**, 729–742 (2018).

129. Do, A.-V., Smith, R., Acri, T. M., Geary, S. M. & Salem, A. K. 3D printing technologies for 3D scaffold engineering. in *Functional 3D tissue engineering scaffolds* 203–234 (Elsevier, 2018).

130. Cengiz, I. F. *et al.* Building the basis for patient-specific meniscal scaffolds: from human knee MRI to fabrication of 3D printed scaffolds. *Bioprinting* **1**, 1–10 (2016).

131. Koffler, J. *et al.* Biomimetic 3D-printed scaffolds for spinal cord injury repair. *Nat. Med.* **25**, 263–269 (2019).

132. Corcione, C. E. *et al.* Highly loaded hydroxyapatite microsphere/PLA porous scaffolds obtained by fused deposition modelling. *Ceram. Int.* **45**, 2803–2810 (2019).

133. Cai, H., Azangwe, G. & Shepherd, D. E. T. Skin cell culture on an ear-shaped scaffold created by fused deposition modelling. *Biomed. Mater. Eng.* **15**, 375–380 (2005).

134. Distler, T. *et al.* Polymer-bioactive glass composite filaments for 3D scaffold manufacturing by fused deposition modeling: fabrication and characterization. *Front. Bioeng. Biotechnol.* **8**, 552 (2020).

135. Liu, F.-H., Lee, R.-T., Lin, W.-H. & Liao, Y.-S. Selective laser sintering of bio-metal scaffold. *Procedia Cirp* **5**, 83–87 (2013).

136. Duan, B. *et al.* Three-dimensional nanocomposite scaffolds fabricated via selective laser sintering for bone tissue engineering. *Acta Biomater.* **6**, 4495–4505 (2010).

137. Yeong, W. Y. *et al.* Porous polycaprolactone scaffold for cardiac tissue engineering fabricated by selective laser sintering. *Acta Biomater.* **6**, 2028–2034 (2010).

138. Lee, S.-J., Nowicki, M., Harris, B. & Zhang, L. G. Fabrication of a highly aligned neural scaffold via a table top stereolithography 3D printing and electrospinning. *Tissue Eng. Part A* **23**, 491–502 (2017).

139. Kim, J. *Advanced multidirectional UV lithography for three dimensional (3-D) micro-/nano structures*. (State University of New York at Buffalo, 2011).

140. Aisenbrey, E. A. *et al.* A Stereolithography-Based 3D Printed Hybrid Scaffold for In Situ Cartilage Defect Repair. *Macromol. Biosci.* **18**, 1700267 (2018).

141. Elomaa, L. *et al.* Preparation of poly (ε-caprolactone)-based tissue engineering scaffolds by stereolithography. *Acta Biomater.* **7**, 3850–3856 (2011).

142. Yeong, W. Y., Chua, C. K., Leong, K. F., Chandrasekaran, M. & Lee, M. W. Indirect fabrication of collagen scaffold based on inkjet printing technique. *Rapid Prototyp. J.* **12**, 229–237 (2006).

143. Tappa, K. & Jammalamadaka, U. Novel biomaterials used in medical 3D printing techniques. *J. Funct. Biomater.* **9**, 17 (2018).

144. Kim, S. H. *et al.* Precisely printable and biocompatible silk fibroin bioink for digital light processing 3D printing. *Nat. Commun.* **9**, 1–14 (2018).

145. Bishop, E. S. *et al.* 3-D bioprinting technologies in tissue engineering and regenerative medicine: Current and future trends. *Genes Dis.* **4**, 185–195 (2017).

146. Zhang, G., Guo, J., Chen, H. & Cao, Y. Organic mesh template-based laminated object manufacturing to fabricate ceramics with regular micron scaled pore structures. *J. Eur. Ceram. Soc.* **41**, 2790–2795 (2021).

147. Das, S., Bourell, D. L. & Babu, S. S. Metallic materials for 3D printing. *Mrs Bull.* **41**, 729–741 (2016).

148. Ginestra, P. *et al.* Selective laser melting and electron beam melting of Ti6Al4V for orthopedic applications: a comparative study on the applied building direction. *Materials (Basel).* **13**, 5584 (2020).

149. Zafar, M. J., Zhu, D. & Zhang, Z. 3D printing of bioceramics for bone tissue engineering. *Materials (Basel).* **12**, 3361 (2019).

150. Ning, L. & Chen, X. A brief review of extrusion-based tissue scaffold bio-printing. *Biotechnol. J.* **12**, 1600671 (2017).

151. Ozbolat, I. T. & Hospodiuk, M. Current advances and future perspectives in extrusion-based bioprinting. *Biomaterials* **76**, 321–343 (2016).

152. Yoon, H. S., Yang, K., Kim, Y. M., Nam, K. & Roh, Y. H. Cellulose nanocrystals as support nanomaterials for dual droplet-based freeform 3D printing. *Carbohydr. Polym.* **272**, 118469 (2021).

153. Bártolo, P. J., Chua, C. K., Almeida, H. A., Chou, S. M. & Lim, A. S. C. Biomanufacturing for tissue engineering: Present and future trends. *Virtual Phys. Prototyp.* **4**, 203–216 (2009).

154. Baker, M. I., Walsh, S. P., Schwartz, Z. & Boyan, B. D. A review of polyvinyl alcohol and its uses in cartilage and orthopedic applications. *J. Biomed. Mater. Res. Part B Appl. Biomater.* **100**, 1451–1457 (2012).

155. Isaacson, A., Swioklo, S. & Connon, C. J. 3D bioprinting of a corneal stroma equivalent. *Exp. Eye Res.* **173**, 188–193 (2018).

156. Zhu, K. *et al.* A general strategy for extrusion bioprinting of bio-macromolecular bioinks through alginate-templated dual-stage crosslinking. *Macromol. Biosci.* **18**, 1800127 (2018).

157. Wu, Z. *et al.* Bioprinting three-dimensional cell-laden tissue constructs with controllable degradation. *Sci. Rep.* **6**, 1–10 (2016).

158. Diamantides, N. *et al.* Correlating rheological properties and printability of collagen bioinks: the effects of riboflavin photocrosslinking and pH. *Biofabrication* **9**, 34102 (2017).

159. Lee, H. *et al.* Fabrication of micro/nanoporous collagen/dECM/silk-fibroin biocomposite scaffolds using a low temperature 3D printing process for bone tissue regeneration. *Mater. Sci. Eng. C* **84**, 140–147 (2018).

160. Shin, K.-H., Kim, J.-W., Koh, Y.-H. & Kim, H.-E. Novel self-assembly-induced 3D plotting for macro/nano-porous collagen scaffolds comprised of nanofibrous collagen filaments. *Mater. Lett.* **143**, 265–268 (2015).

161. Kim, B. S., Lee, J.-S., Gao, G. & Cho, D.-W. Direct 3D cell-printing of human skin with functional transwell system. *Biofabrication* **9**, 25034 (2017).

162. Sanjana, N. E. & Fuller, S. B. A fast flexible ink-jet printing method for patterning dissociated neurons in culture. *J. Neurosci. Methods* **136**, 151–163 (2004).

163. Boland, T., Mironov, V., Gutowska, A., Roth, E. A. & Markwald, R. R. Cell and organ printing 2: Fusion of cell aggregates in three-dimensional gels. *Anat. Rec. Part A Discov. Mol. Cell. Evol. Biol.* **272**, 497–502 (2003).

164. Roth, E. A. *et al.* Inkjet printing for high-throughput cell patterning. *Biomaterials* **25**, 3707–3715 (2004).

165. Park, T.-M. *et al.* Fabrication of in vitro cancer microtissue array on fibroblast-layered nanofibrous membrane by inkjet printing. *Int. J. Mol. Sci.* **18**, 2348 (2017).

166. Murphy, S. V, Skardal, A. & Atala, A. Evaluation of hydrogels for bio-printing applications. *J. Biomed. Mater. Res. Part A* **101**, 272–284 (2013).

167. Duarte Campos, D. F. *et al.* Bioprinting organotypic hydrogels with improved mesenchymal stem cell remodeling and mineralization properties for bone tissue engineering. *Adv. Healthc. Mater.* **5**, 1336–1345 (2016).

168. Michael, S. *et al.* Tissue engineered skin substitutes created by laser-assisted bioprinting form skin-like structures in the dorsal skin fold chamber in mice. *PLoS One* **8**, e57741 (2013).

169. Koch, L. *et al.* Skin tissue generation by laser cell printing. *Biotechnol. Bioeng.* **109**, 1855–1863 (2012).

170. Keriquel, V. *et al.* In situ printing of mesenchymal stromal cells, by laser-assisted bioprinting, for in vivo bone regeneration applications. *Sci. Rep.* **7**, 1–10 (2017).

171. Sorkio, A. *et al.* Human stem cell based corneal tissue mimicking structures using laser-assisted 3D bioprinting and functional bioinks. *Biomaterials* **171**, 57–71 (2018).

172. Angele, P. *et al.* Influence of different collagen species on physico-chemical properties of crosslinked collagen matrices. *Biomaterials* **25**, 2831–2841 (2004).

173. Huang, G. P. *et al.* An investigation of common crosslinking agents on the stability of electrospun collagen scaffolds. *J. Biomed. Mater. Res. Part A* **103**, 762–771 (2015).

174. Gu, L., Shan, T., Ma, Y., Tay, F. R. & Niu, L. Novel biomedical applications of crosslinked collagen. *Trends Biotechnol.* **37**, 464–491 (2019).

175. Nair, M., Best, S. M. & Cameron, R. E. Crosslinking collagen constructs: achieving cellular selectivity through modifications of physical and chemical properties. *Appl. Sci.* **10**, 6911 (2020).

176. Farris, S., Song, J. & Huang, Q. Alternative reaction mechanism for the cross-linking of gelatin with glutaraldehyde. *J. Agric. Food Chem.* **58**, 998–1003 (2010).

177. Mendoza-Novelo, B., Mata-Mata, J. L., Vega-González, A., Cauich-Rodríguez, J. V & Marcos-Fernández, Á. Synthesis and characterization of protected oligourethanes as crosslinkers of collagen-based scaffolds. *J. Mater. Chem. B* **2**, 2874–2882 (2014).

178. Zeugolis, D. I., Paul, G. R. & Attenburrow, G. Cross-linking of extruded collagen fibers—A biomimetic three-dimensional scaffold for tissue engineering applications. *J. Biomed. Mater. Res. Part A An Off. J. Soc. Biomater. Japanese Soc. Biomater. Aust. Soc. Biomater. Korean Soc. Biomater.* **89**, 895–908 (2009).

179. Barnes, C. P., Pemble IV, C. W., Brand, D. D., Simpson, D. G. & Bowlin, G. L. Cross-linking electrospun type II collagen tissue engineering scaffolds with carbodiimide in ethanol. *Tissue Eng.* **13**, 1593–1605 (2007).

180. Hafemann, B., Ghofrani, K., Gattner, H.-G., Stieve, H. & Pallua, N. Cross-linking by 1-ethyl-3-(3-dimethylaminopropyl)-carbodiimide (EDC) of a collagen/elastin membrane meant to be used as a dermal substitute: effects on physical, biochemical and biological features in vitro. *J. Mater. Sci. Mater. Med.* **12**, 437–446 (2001).

181. Krishnamoorthy, G., Sehgal, P. K., Mandal, A. B. & Sadulla, S. Development of D-lysine-assisted 1-ethyl-3-(3-dimethylaminopropyl)-carbodiimide/N-hydroxysuccinimide-initiated cross linking of collagen matrix for design of scaffold. *J. Biomed. Mater. Res. Part A* **101**, 1173–1183 (2013).

182. Ma, B., Wang, X., Wu, C. & Chang, J. Crosslinking strategies for preparation of extracellular matrix-derived cardiovascular scaffolds. *Regen. Biomater.* **1**, 81–89 (2014).

183. Yung, C. W. *et al.* Transglutaminase crosslinked gelatin as a tissue engineering scaffold. *J. Biomed. Mater. Res. Part A An Off. J. Soc. Biomater. Japanese Soc. Biomater. Aust. Soc. Biomater. Korean Soc. Biomater.* **83**, 1039–1046 (2007).

184. Powell, H. M. & Boyce, S. T. EDC cross-linking improves skin substitute strength and stability. *Biomaterials* **27**, 5821–5827 (2006).

185. Reddy, N., Reddy, R. & Jiang, Q. Crosslinking biopolymers for biomedical applications. *Trends Biotechnol.* **33**, 362–369 (2015).

186. Gough, J. E., Scotchford, C. A. & Downes, S. Cytotoxicity of glutaraldehyde crosslinked collagen/poly (vinyl alcohol) films is by the mechanism of apoptosis. *J. Biomed. Mater. Res. An Off. J. Soc. Biomater. Japanese Soc. Biomater. Aust. Soc. Biomater. Korean Soc. Biomater.* **61**, 121–130 (2002).

187. Weadock, K. S., Miller, E. J., Keuffel, E. L. & Dunn, M. G. Effect of physical crosslinking methods on collagen-fiber durability in proteolytic solutions. *J. Biomed. Mater. Res. An Off. J. Soc. Biomater. Japanese Soc. Biomater.* **32**, 221–226 (1996).

188. Weadock, K. S., Miller, E. J., Bellincampi, L. D., Zawadsky, J. P. & Dunn, M. G. Physical crosslinking of collagen fibers: comparison of ultraviolet irradiation and dehydrothermal treatment. *J. Biomed. Mater. Res.* **29**, 1373–1379 (1995).

189. Yunoki, S., Suzuki, T. & Takai, M. Stabilization of low denaturation temperature collagen from fish by physical cross-linking methods. *J. Biosci. Bioeng.* **96**, 575–577 (2003).

190. Dong, C.-M. *et al.* Photomediated crosslinking of C6-cinnamate derivatized type I collagen. *Biomaterials* **26**, 4041–4049 (2005).

191. Alarcon, E. I. *et al.* Rose Bengal binding to collagen and tissue photobonding. *ACS omega* **2**, 6646–6657 (2017).

192. Ibusuki, S. *et al.* Photochemically cross-linked collagen gels as three-dimensional scaffolds for tissue engineering. *Tissue Eng.* **13**, 1995–2001 (2007).

193. Orban, J. M. *et al.* Crosslinking of collagen gels by transglutaminase. *J. Biomed. Mater. Res. Part A* **68**, 756–762 (2004).

194. Staroszczyk, H., Pielichowska, J., Sztuka, K., Stangret, J. & Kołodziejska, I. Molecular and structural characteristics of cod gelatin films modified with EDC and TGase. *Food Chem.* **130**, 335–343 (2012).

195. Valero, C., Amaveda, H., Mora, M. & García-Aznar, J. M. Combined experimental and computational characterization of crosslinked collagen-based hydrogels. *PLoS One* **13**, e0195820 (2018).

196. Drexler, J. W. & Powell, H. M. Dehydrothermal crosslinking of electrospun collagen. *Tissue Eng. Part C Methods* **17**, 9–17 (2011).

197. Varley, M. C. *et al.* Cell structure, stiffness and permeability of freeze-dried collagen scaffolds in dry and hydrated states. *Acta Biomater.* **33**, 166–175 (2016).

198. Gibson, L. J. Cellular solids. *Mrs Bull.* **28**, 270–274 (2003).

199. Gibson, Lorna J., A. M. F. Cellular solids. *Journal of Biomechanics* vol. 22 397 (1997).

200. Harley, B. A., Leung, J. H., Silva, E. C. C. M. & Gibson, L. J. Mechanical characterization of collagen-glycosaminoglycan scaffolds. *Acta Biomater.* **3**, 463–474 (2007).

201. Mitsak, A. G., Kemppainen, J. M., Harris, M. T. & Hollister, S. J. Effect of polycaprolactone scaffold permeability on bone regeneration in vivo. *Tissue Eng. Part A* **17**, 1831–1839 (2011).

202. Pennella, F. *et al.* A survey of methods for the evaluation of tissue engineering scaffold permeability. *Ann. Biomed. Eng.* **41**, 2027–2041 (2013).

203. Zhao, H., Li, L., Ding, S., Liu, C. & Ai, J. Effect of porous structure and pore size on mechanical strength of 3D-printed comby scaffolds. *Mater. Lett.* **223**, 21–24 (2018).

204. Mohee, L., Offeddu, G. S., Husmann, A., Oyen, M. L. & Cameron, R. E. Investigation of the intrinsic permeability of ice-templated collagen scaffolds as a function of their structural and mechanical properties. *Acta Biomater.* **83**, 189–198 (2019).

205. Ryan, L. D. & Kaler, E. W. Alkyl polyglucoside microemulsion phase behavior. *Colloids Surfaces A Physicochem. Eng. Asp.* **176**, 69–83 (2001).

206. Barbareschi, M., Benetti, F., Gaio, E., Angileri, L. & Veraldi, S. Capryloyl glycine and soy isoflavonoids in hypertrichosis: An experimental and placebo-controlled clinical study. *J. Cosmet. Dermatol.* **20**, 18–22 (2021).

207. Zawidlak-Węgrzyńska, B. *et al.* In vivo biocompatibility of an innovative elastomer for heart assist devices. *Polymers (Basel).* **14**, 1002 (2022).

208. Murcia, M. D. *et al.* Optimization of a sustainable biocatalytic process for the synthesis of ethylhexyl fatty acids esters. *Catal. Today* **346**, 98–105 (2020).

209. Sharipov, M., Tawfik, S. M., Gerelkhuu, Z., Huy, B. T. & Lee, Y.-I. Phospholipase A2-responsive phosphate micelle-loaded UCNPs for bioimaging of prostate cancer cells. *Sci. Rep.* **7**, 1–9 (2017).

210. Raphael, A. P., Garrastazu, G., Sonvico, F. & Prow, T. W. Formulation design for topical drug and nanoparticle treatment of skin disease. *Ther. Deliv.* **6**, 197–216 (2015).

211. Pradhan, P. *et al.* Comparative evaluation of heating ability and biocompatibility of different ferrite-based magnetic fluids for hyperthermia application. *J. Biomed. Mater. Res. Part B Appl. Biomater. An Off. J. Soc. Biomater. Japanese Soc. Biomater. Aust. Soc. Biomater. Korean Soc. Biomater.* **81**, 12–22 (2007).

212. Tran, N. *et al.* Polyurethane/polycaprolactone membrane grafted with conjugated linoleic acid for artificial vascular graft application. *Sci. Technol. Adv. Mater.* **21**, 56–66 (2020).

213. Rao, L., Zhou, H., Li, T., Li, C. & Duan, Y. Y. Polyethylene glycol-containing polyurethane hydrogel coatings for improving the biocompatibility of neural electrodes. *Acta Biomater.* **8**, 2233–2242 (2012).

214. Nelson, K. D., Eisenbaumer, R., Pomerantz, M. & Eberhart, R. C. High affinity polyethylene oxide for improved biocompatibility. *ASAIO J. (American Soc. Artif. Intern. Organs 1992)* **42**, M884-9 (1996).

215. Gupta, S. & Moulik, S. P. Biocompatible microemulsions and their prospective uses in drug delivery. *J. Pharm. Sci.* **97**, 22–45 (2008).

216. Martinelli, F. *et al.* Engineered sodium hyaluronate respirable dry powders for pulmonary drug delivery. *Int. J. Pharm.* **517**, 286–295 (2017).

217. Almeida, E. D. P. *et al.* Skin permeation, biocompatibility and antitumor effect of chloroaluminum phthalocyanine associated to oleic acid in lipid nanoparticles. *Photodiagnosis Photodyn. Ther.* **24**, 262–273 (2018).

218. Tackie-Otoo, B. N., Mohammed, M. A. A. & Tze, J. Y. S. Experimental Investigation of N-lauroyl Sarcosine and N-lauroyl-L-glutamic Acid as Green Surfactants for Enhanced Oil Recovery Application. *J. Mol. Liq.* 119738 (2022).

219. Poly(ethylene glycol) average mol wt 8,000, powder 25322-68-3. https://www.sigmaaldrich.com/CA/en/product/aldrich/p2139.

220. Partovinia, A. & Naeimpoor, F. Phenanthrene biodegradation by immobilized microbial consortium in polyvinyl alcohol cryogel beads. *Int. Biodeterior. Biodegradation* **85**, 337–344 (2013).

221. Aliabadi, H. M., Mahmud, A., Sharifabadi, A. D. & Lavasanifar, A. Micelles of methoxy poly(ethylene oxide)-b-poly(ε-caprolactone) as vehicles for the solubilization and controlled delivery of cyclosporine A. *J. Control. Release* **104**, 301–311 (2005).

222. Poly(ethylene oxide) average Mv 100,000, powder 25322-68-3. https://www.sigmaaldrich.com/CA/en/product/aldrich/181986.

223. Pratas, M. J. *et al.* Densities and viscosities of fatty acid methyl and ethyl esters. *J. Chem. Eng. Data* **55**, 3983–3990 (2010).

224. Aumann, S., Donner, S., Fischer, J. & Müller, F. Optical coherence tomography (OCT): principle and technical realization. *High Resolut. Imaging Microsc. Ophthalmol.* 59–85 (2019).

225. Langendorf, E. K., Rommens, P. M., Drees, P. & Ritz, U. Dexamethasone Inhibits the Pro-Angiogenic Potential of Primary Human Myoblasts. *Int. J. Mol. Sci.* **22**, 7986 (2021).